REVERSIBILITY OF ARCTIC SEA ICE RETREAT

-

A CONCEPTUAL MULTI-SCALE MODELING APPROACH

By

Marc Mueller-Stoffels

RECOMMENDED:

Advisory Committee Chair

Chair, Department of Physics

APPROVED:

Dean, College of Natural Science and Mathematics

Dean of the Graduate School

April 11, 2012

Date

REVERSIBILITY OF ARCTIC SEA ICE RETREAT

-

A CONCEPTUAL MULTI-SCALE MODELING APPROACH

A

THESIS

Presented to the Faculty

of the University of Alaska Fairbanks

in Partial Fulfillment of the Requirements

for the Degree of

DOCTOR OF PHILOSOPHY

By

Marc Mueller-Stoffels, M.S.

Fairbanks, Alaska

May 2012

UMI Number: 3528860

All rights reserved

INFORMATION TO ALL USERS
The quality of this reproduction is dependent upon the quality of the copy submitted.

In the unlikely event that the author did not send a complete manuscript
and there are missing pages, these will be noted. Also, if material had to be removed,
a note will indicate the deletion.

UMI 3528860
Published by ProQuest LLC 2012. Copyright in the Dissertation held by the Author.
Microform Edition © ProQuest LLC.
All rights reserved. This work is protected against
unauthorized copying under Title 17, United States Code.

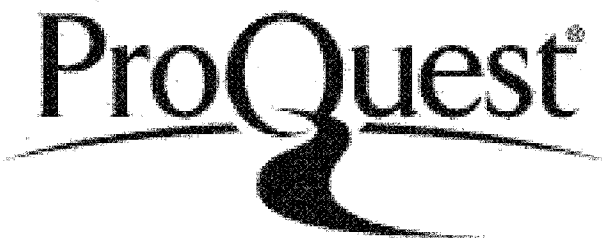

ProQuest LLC
789 East Eisenhower Parkway
P.O. Box 1346
Ann Arbor, MI 48106-1346

Abstract

The ice-albedo feedback has been identified as an important factor in the decay of the Arctic sea ice cover in a warming climate. Mechanisms of transition from perennial ice cover to seasonal ice cover are discussed in the literature; the existence of a tipping point is disputed. A newly developed regular network model for energy exchange and phase transition of an ice covered ocean mixed layer is introduced. The existence of bistability, a key ingredient for irreversibility, on local and regional scales is explored. It is shown in a spatially confined model that the asymptotic behavior and the existence of a parameter region of bistability strongly depend on the albedo parametrization. The spatial dynamics of sea ice retreat are studied for a high resolution latitudinal model of the ocean mixed layer. This regional model suggests that sea ice retreat is reversible. It is shown that laterally driven melt of thick multi-year sea ice, and thus, ice-albedo feedback, is an important mechanism in the transition from perennial to seasonal ice cover at the pole. Results are used to interpret observed changes in the recent ice extent and ice volume record. It is shown that the effectiveness of ice-albedo feedback strongly depends on the existence of lateral heat transfer mechanisms in the ocean.

Table of Contents

Page

List of Figures

Page

List of Tables

Page

Acknowledgements

Many people have helped and encouraged me on my way to the point I am at today. As this work is the, to date, ultimate accomplishment of my educational journey it is only appropriate that I first and foremost thank all my outstanding teachers inside and outside the classroom.

Special thanks go to my advisor Dr. Renate Wackerbauer. Renate, thank you for having the courage to take on this project, for being patient with me, and for teaching me a great deal about how quality research, and quality research documentation is done. Where this work still lacks quality it is entirely my fault.

Ice albedo feedback and low order models were first introduced to me by Dr. Hajo Eicken. Hajo, thank you for interesting me in pursuing this line of research and for explaining, from the sea ice specialist's and geophysicist's point of view, what is needed to improve this work.

To the entirety of my advisory committee, Dr. Renate Wackerbauer, Dr. Hajo Eicken, Dr. David Newman, Dr. Martin Truffer and the late Dr. Davis Sentman, go many thanks for lending their experience, advice and time to keep this project on track.

There are some people without whom graduate students could easily get lost in piles of paperwork. To Mary Parsons and Saundra Jefko go very special thanks for helping me make sense of forms and formalities that seem to require more than a PhD to navigate.

Funding for this project has come from many highly appreciated sources: the UAF Physics Department (teaching assistantship and resources), the UAF Graduate School (graduate student fellowship, thesis completion grant, and travel grant), the Cooperative Institute for Alaskan Research (research and travel funds through the Committee for Global Change student grant competition), the Arctic Region Supercomputing Center (computational resources), and the UAF College of Natural Science and Mathematics (travel grant). When no funding was to be found for this project Renate Wackerbauer, Hajo Eicken and Gwen Holdmann (Alaska Center for Energy and Power) trusted me to work on other exciting projects.

Last, but not least, tremendous thanks go to my family, especially to my wife Megan, for supporting me and for encouraging me to see this project through at the times when I would have rather done anything but this.

Never follow another man's footsteps.
Dare to travel uncharted ground.
On your way you may fall; you may stumble.
You blaze trails that may come to an end.
When you wonder if it's worth the trouble.
Hold your head high and head out again.

Hobo Jim - Uncharted Ground

Chapter 1
Introduction

If the Earth were 1 m in diameter, a typical sea ice cover would be the approximate thickness of a cell membrane (10 to 100 nm). Depending on the season it would cover over 10% of the globe. It is this large extent, coupled with the remarkable physical properties of sea ice that makes this thin skim of ice of such great importance to the balance of Earth's climate system and the polar region ecosystems.

Sea ice provides two essential services to humanity. It is part of the supply chain of nutrients at the foundation of the food web and it is part of the mechanisms regulating temperatures that allow life on Earth to be sustained. Furthermore, to the peoples of the Arctic region, sea ice is a matter of survival as it provides a hunting platform and protects costal villages from waves generated by winter storms (Overeem et al., 2011). Better predictions of ice extent and volume are of interest to resource extracting industries and marine shipping companies planning to use the Arctic Ocean (Brigham, 2007; Müller-Stoffels and Eicken, 2011). Thus, it is of great interest to understand the fate of Earth's sea ice covers in a changing climate.

It is the consensus of all leading general circulation models (GCMs, a.k.a. climate models), that the Arctic sea ice perennial extent is retreating and will continue to retreat under current greenhouse gas emission projections for the coming century. Figure 1.1 shows possible scenarios of retreat of the Arctic sea ice cover. The amount of sea ice retreat is highly disputed amongst these models, with some predicting moderate sea ice losses and others predicting an Arctic Ocean that is ice free in the summer by 2100. Interestingly, the real world retreat of summer sea ice (Fig. 1.1, red line) outpaces all but one of the model projections. The inter-model variability is caused by differing initial conditions, differences in forcing used during model spin-up phase, and different parametrizations of climate subsystems, e.g., the albedo parametrization. It has been shown that slight changes to how the albedo is parametrized can change model trajectories significantly (Eisenman, Untersteiner, and Wettlaufer, 2007). The sharp decline in summer ice extent has raised the question whether the Arctic ice cover has reached a tipping point (Walker, 2006), i.e., a point of irreversible losses. This notion is supported by model findings based on ordinary differential equation (ODE) models (Thorndike, 1992; Eisenman and Wettlaufer, 2009), but

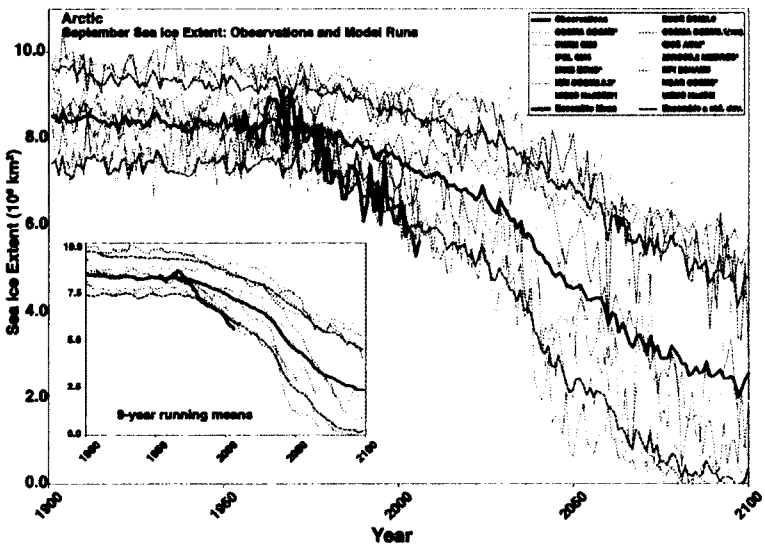

Figure 1.1. Arctic September sea ice extent ($\times 10^6$ km^2) from observations (thick red line) and 13 IPCC AR4 climate models (IPCC, 2007), together with the multi-model ensemble mean (solid black line) and standard deviation (dotted black line). Inset shows 9-year running means (Stroeve et al., 2007).

has also been contradicted by ODE models (Notz, 2009). ODE models do not exhibit an explicit spatial extent, which makes it difficult to relate sudden ice cover losses in them to the retreat of the sea ice cover in nature. Energy balance models (EBMs) implement latitudinal spatial extent and solve coupled ODE (Budyko, 1969; Sellers, 1969; North, 1984; Shine and Henderson-Sellers, 1985; Winton, 2008). EBMs can resolve the retreat of a sea ice cover, but generally they lack an explicit time-dependence, which limits their resolution of seasonal cycles and cannot capture the observed difference in dynamics between summer and winter ice extent. In addition, EBMs generally exhibit a small ice cap instability, which often treated as a model artifact and mechanisms are implemented to eliminate this behavior (North, 1984). Recent results for one GCM suggest that sea ice retreat is reversible (Armour et al., 2011), but connections to irreversible sea ice loss observed in ODE models are lacking. Known feedback processes in the Arctic climate support the argument for a tipping point (Bony et al., 2006), but it has been difficult to connect ODE model results to GCM results. The goal of the study presented here is to provide an intermediate regular network model with spatial extent that can serve as a link between ODE models and

GCMs, and to study feedbacks in climate sub-systems.

1.1 Albedo

Sea ice is a very good reflector of sunlight. Thus, the Earth's polar regions are partially covered with a near perfect mirror, reflecting much of the incoming shortwave radiation directly back to space (Fig.1.2). Variations in quality and size of this mirror will have a direct impact on Earth's climate system as a whole. This is amplified by the fact that sea ice covers oceans, which themselves are near perfect absorbers of shortwave radiation. For example, an area at the North pole which is not covered by sea ice will absorb over 6 times more energy as the same area was it covered by sea ice.

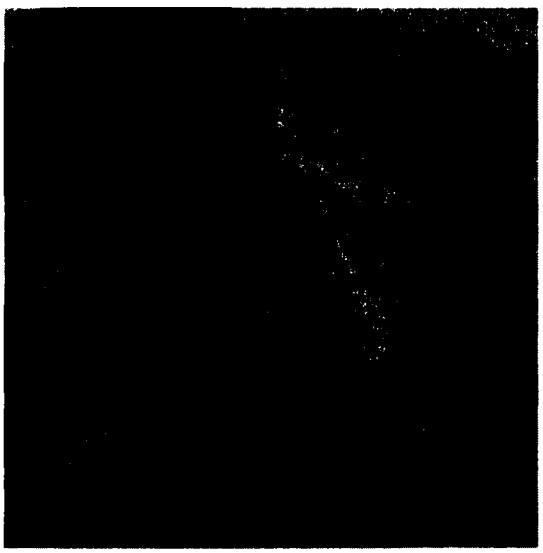

Figure 1.2. Aerial photograph of sea ice and open water. Snow covered sea ice is nearly white; draining melt ponds are light blue; Submerged ice is dark blue/green and open water is dark. Image by Norbert Rosing/National Geographic.

Albedo is a dimensionless number between 0 and 1 describing the efficiency electromagnetic radiation is reflected. At the microscopic scale, most materials do not reflect all wavelengths of electromagnetic radiation in the same fashion, therefore, the albedo is a function of wavelength (spectral albedo $\alpha(\lambda)$). In addition, bulk properties, such as surface roughness, have an effect on the albedo. It is not uncommon to use bulk albedo values

over a given spectrum of wavelengths, α,

$$\alpha = \frac{\int_{\lambda_1}^{\lambda^2} \alpha(\lambda) d\lambda}{\int_{\lambda_1}^{\lambda^2} d\lambda}, \tag{1.1}$$

where λ_1 and λ_2 are the wavelengths delimiting the given spectrum. In this work the term albedo will be used to denote bulk albedo for the visible spectrum (Perovich et al., 2002). For the visible spectrum the rule of thumb is: the lighter the shade of a surface, the higher its albedo.

In the climate system, albedos play an important role in determining the radiation balances at given surfaces, particularly for solar shortwave radiation. Most prominent are the top of the atmosphere albedo and the Earth's surface albedo. The top of the atmosphere albedo determines the amount of solar shortwave radiation received by the Earth's surface. Surface albedos determine how much incoming solar shortwave radiation is absorbed as thermal energy (Peixoto and Oort, 1992).

1.2 Sea Ice

Unlike freshwater ice, which is pure frozen water, sea ice is a composite material of ice crystals, brine and air bubbles. The network of brine pockets is a safe haven for micro-organisms. The organisms growing on and in sea ice are the cornerstones of the food web in both the Arctic and the Antarctic. Fig. 1.3 shows both brine pockets and algal growth on an ice core taken of the coast of Barrow, AK in May 2011. The various materials within sea ice form a layered structure rendering it opaque and giving it its high albedo. First-year sea ice has the highest albedo of up to 0.7; as the ice undergoes freeze-thaw cycles, brine is flushed out of the ice and replaced by refreezing melt water. This results in slowly diminishing albedos during melt and an increase in albedo during refreezing as a surface scattering layer, due to air inclusions, forms. The lowest sea ice albedo (around 0.4) is found on ice on which water forms melt ponds (Perovich et al., 2002; Thomas and Dieckmann, 2003).

How sea ice is modeled depends greatly on the scale of processes that are of interest within the model. It is important to understand processes on all scales in order to make informed decisions as to which of them need to be directly or indirectly included and which can be ignored.

Figure 1.3. Sea ice core with algal layer (Krembs and Deming, 2012).

Sea ice micro-physics: Sea water is a solution of water and various salts. The salt concentrations in standard sea water are around 33 ppt, far below the saturation points, but high enough to depress the freezing point by up to 2 K (Assur, 1958; Cox and Weeks, 1983). It is interesting to note that the melting point of all ice in a volume of water is determined by the freezing point of the melt. Even though freshwater ice remains solid up to 273 K it will melt when put in contact with liquid sea water below that temperature. The main component of sea ice is frozen water in the form of hexagonal ice. Single sea ice crystals can be from millimeters to tens of centimeters in size depending on freezing conditions. Hexagonal ice forms a crystal lattice in which few other materials can be incorporated. Thus, the salt ions in sea water cannot be incorporated directly into the crystal lattice. Instead much of the brine is expelled back to the ocean. However, some of the salts will not diffuse away from the encroaching ice water interface fast enough. This causes the formation of brine pockets within the sea ice. It also causes the ice crystals to grow in a lamellar structure where the lamellae are separated by thin layers of brine. The amount of brine incorporated into growing sea ice is directly proportional to the growth rate. The brine inclusions in sea ice vary in size depending on temperature. As sea ice cools below the freezing point of the given salt concentration in its brine pockets, remaining water within these pockets

freezes. This increases the salt concentration within a brine pocket, thus further depressing its freezing point. This change of brine pockets size affects the local concentration of salts, not the bulk salinity of the ice. The effect of brine pockets changing their size is limited by the maximum dissolvable salt concentration, at which the freezing point cannot be depressed any further. And by the fact that the prevalently present salt ions precipitate at specific temperatures, e.g., NaCl will precipitate as hydrohalite at -22 °C. Once precipitated, a salt does not contribute to the freezing point depression any longer. The process of brine pocket incorporation and the lamellar growth from the melt causes sea ice to be full of scatterers and refractive surfaces (Thomas and Dieckmann, 2003; Assur, 1958). At temperatures above -5 °C and bulk ice salinities above 5 ppt sea ice becomes permeable. This is due to brine pockets enlarging enough to form a network of connected cells. Through these brine channels nutrients move up into the ice and meltwater moves down through the ice. This can cause significant changes to the material qualities of sea ice during the melt season (Golden, Ackley, and Lytle, 1998). Constitutional changes in surface ice through the processes described here lead to changes in albedo. Particularly, melt water draining into the ice and refreezing in brine channels makes the ice less saline and darker in color.

Sea ice dynamics: In the Arctic Ocean sea ice is in motion due to ocean currents and wind. During this movement, large masses of ice are driven into each other forming pressure ridges of up of 30 m thick (Leppäranta, 2011). Continuous ice covers are sheared apart to form leads, areas of open water that can be several kilometers wide and tens of kilometers in length (Frederking and Timco, 1984). Leads expose the relatively warm ocean to the cold atmosphere, causing the region downwind of a lead to experience a micro-climate with warmer temperatures and higher precipitation (Esau, 2007).

The prevailing currents in the Arctic Ocean (Fig. 1.4) are an inflow of water through the Bering Strait along the coast of northern Alaska, the Beaufort gyre, which moves clockwise through the Arctic Ocean, centered south of the pole and north of Siberia and Alaska, and the transpolar drift, moving from Siberia towards Greenland. The interplay of these currents results in large amounts of sea ice being shoved against the Canadian archipelago and flushed out of the Arctic through Fram Strait on the Eastern shore of Greenland. Thus, the oldest and thickest sea ice in the Arctic is not found at the pole, but in the Canadian

Figure 1.4. Ocean currents in the Arctic. Cold surface water enters the Arctic through the Bering Strait and leaves the Arctic through Fram Strait and Davis Strait. Warmer Atlantic water flows past Europe and enters the Arctic basin at depth. Illustration by Jack Cook, Woods Hole Oceanographic Institution.

Arctic with multiyear ice up to 10 years old and up to 10 m thick.

Interaction with ocean and atmosphere: Sea ice separates ocean and atmosphere, both of which have very high effective thermal conductivities due to the motion of water and air masses. In the winter, temperature gradients through the ice can be as large as 40 K m^{-1}. This limits the amount of energy exchanged between ocean and atmosphere and effectively insulates the ocean from the atmosphere. The insulating effect can be further enhanced if a snow cover is present on the ice (Curry and Webster, 1999).

Snow: The thermal conductivity of snow is an order of magnitude smaller than that of sea ice. This can have direct implications on the growth dynamics of an ice cover. If snow falls on open ocean it can induce the growth of sea ice by effectively cooling the upper most layer of ocean water. If snow falls on thin sea ice it can hamper the growth of ice by effectively insulating the ice cover from the cold atmosphere. In the spring and summer, snow cover can delay the melting of ice due to high snow albedo (Massom et al., 2001).

1.3 Modeling climate (sub-) systems

General circulation models: The main tool to model Earth's climate are general circulation models. These models describe large-scale interactions between oceans, landmasses and atmosphere reasonably well and include longwave, shortwave radiative budget models, circulation of oceanic and atmospheric flows, and precipitation models. Many physical quantities are parametrized to model sub-grid processes in GCMs. This is necessary because many of the general equations of the underlying physical processes are derived from point measurements that need to be extrapolated to the appropriate grid size, or because the exact equations for underlying physical processes are unknown. In addition, computational limitations prevent GCMs from representing complicated processes directly and parametrizations are used to treat such processes 'by proxy'.

GCMs are computationally very expensive because the spatial resolution in GCMs is between 100 and 50 km while the temporal resolution is on the order of minutes. To ensure convergence, GCMs have to meet the Courant-Friedrichs-Lewy (CFL) condition. This is the reason for such high temporal resolution at relatively coarse spatial resolution. Meeting the CFL condition and availability of computational resources constrains GCMs to relatively few model runs and limited exploration of phase space. This limits the understanding about climate subsystems and seemingly minute parameter variations accessible by GCMs (Randal, 2000). This problem can be exacerbated for subsystems when some parameters, e.g. the actual value of the ice albedo, are used to adjust model performance for other subsystems (Eisenman, Untersteiner, and Wettlaufer, 2007).

Ordinary differential equation models: Smaller scale models provide insight in the dynamics of climate subsystems and parameter variation. The smallest scale models neglect spatial resolution entirely and solve (coupled) ODEs (Maykut and Untersteiner, 1971; Thorndike, 1992; Eisenman and Wettlaufer, 2009; Notz, 2009). ODE models, which are computationally inexpensive, are able to isolate feedback processes and vastly vary parameters for detailed phase space pictures. ODE model results, if interpreted properly, can be utilized to improve parametrizations in GCMs and to study isolated processes such as the ice albedo feedback.

Intermediate models: To link ODE model results to GCM parametrizations it is desirable to have an intermediate class of models available (Bony et al., 2006). To some extent

latitudinal band models (Sellers, 1969; North, 1984; Winton, 2008) can be used to fill this gap. In this approach coupled ODEs for given latitudes are solved. However, the currently available latitudinal band models make heavy use of tabulated values, parametrizations, and/or extrapolations. The weakness of such an approach is that many interconnected parameters are at work, which strongly limits the ability to study isolated effects. In addition, the use of tabulated values derived from measurements are a severe limitation in modeling a future climate under a significantly changed forcing regime.

An ideal model linking ODE models and GCMs would have a high latitudinal resolution and contains basic physics valid over a large range of forcing parameters. The high latitudinal resolution would allow spatial resolution of seasonal changes and interactions between high and moderate latitudes. Relying on basic physics where possible instead of tabulated or extrapolated seasonal variations gives higher confidence that the model will perform well outside the typical parameter regime. This is important when feedbacks are involved that could result in tipping points, because in this case the parameter regime might suddenly shift outside the currently observed envelope. Any result, based on physical principles, or parametrization, leaving the range of known measurements needs to be subject to increased scrutiny.

Parametrizing longwave radiation: To develop parametrizations that span parameter intervals outside what is observed in nature is challenging. One particularly complicated example is the exchange of longwave radiation between the ocean or ice and the atmosphere. The underlying physical principle is the Stefan-Boltzmann law, which has a fourth order dependency on temperature. This in itself makes it very sensitive to small changes. In addition, most materials are not perfect black body emitters. They are grey-body emitters, which are described by their emissivity e. The emissivity is the fraction of actually emitted radiation at a given temperature and the theoretical value of blackbody emissions at the same temperature. For many materials the emissivity is a constant for a large temperature interval, e.g. ice and water have an emissivity of $\varepsilon = 0.97$ (Campbell and Norman, 1998).

Gases and mixtures of gases and water vapor, such as the atmosphere, can change their composition significantly, i.e., an increase in concentration of greenhouse gases affect the longwave radiative budget (Myhre et al., 1998). The emissivity of the atmosphere depends on the exact composition of gases for a given location and an accurate model regarding

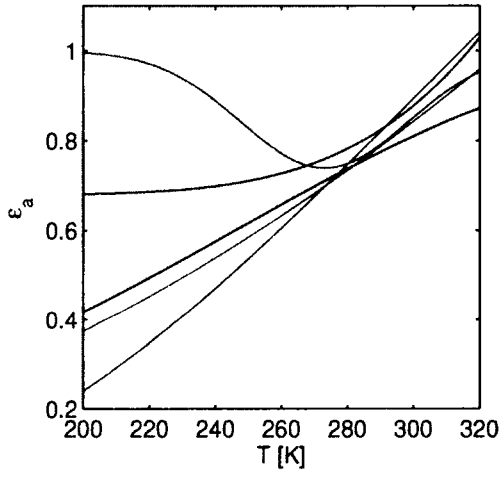

Figure 1.5. Parametrization of atmospheric emissivity for clear sky conditions. Parametrizations are by Satterlund, 1979 [blue]; Swinbank (1963) [red] as given in Crawford and Duchon, 1999; Idso and Jackson (1963) [green] as given in Prata, 1996; Brusaert (1975) [maroon] as given in Prata, 1996; and Anderson (1954) [black] as given in Crawford and Duchon, 1999. Graphs shown are calculated for relative humidity of 80% and saturation vapor pressure calculated using Goff's (1957) equation.

molecular emissions bands for each atmospheric constituent (Siegel and Howell, 1992). Due to the nature of the atmosphere – changing density and temperature with altitude, constant motion, varying saturation vapor pressures with temperature, and underlying surface – it is insufficient to use a laboratory volume of air under controlled conditions to determine the functional relationships governing atmospheric emissivity. Much of the required information for such calculations is either not available or the models required are inaccessible for efficient calculation.

The general approach in such a case is to develop a parametrization based on measurements and basic laws of physics. In the case of the atmospheric emissivity in-situ measurements of the radiation balance are required. There is a multitude of problems with this; Most conspicuous is that any measurement station is subject to local conditions which can deviate significantly from textbook atmosphere, e.g. temperature inversions aloft and lateral heat fluxes can influence measurement. A further obstacle is the presence

of clouds, which are made up of condensed water droplets and not water vapor, effectively changing the atmospheric composition and shielding an air mass and the surface from upwards heat losses into space. The problem here is that ground measurements alone only give information about the cloud ceiling, but not information about cloud thickness, or the possibility of further cloud layers at higher altitudes.

Taking all the obstacles into account many attempts have been made to supply reliable parametrizations of atmospheric emissivities, especially for the case of clear sky conditions (Prata, 1996; Crawford and Duchon, 1999; Satterlund, 1979). Figure 1.5 gives several of the parametrizations for clear skies given in the literature as a function temperature. Many of these parametrizations are a function of saturation vapor pressure as well. Here we assume 80% relative humidity and use Goff's (1957) equation to calculate saturation vapor pressure. As is evident from Fig. 1.5 there are significant deviations between parametrizations. Brusaert's and Anderson's parametrizations turn unphysical, $\varepsilon_a > 1$, for high temperatures. Nonetheless, all parametrizations agree closely around 280 K, which is a relatively typical temperature for moderate latitudes. This illustrates that *a priori* knowledge about the temperature domain of a model and knowledge about the temperature range of the data used to find a particular parametrization is necessary in selecting a suitable one for a model.

1.4 Overview

The research presented in Chapter 2 to 4 introduces a scalable thermodynamic regular network model for an ocean mixed layer that can undergo solid-liquid phase transitions, and is driven by surface radiative forcing and oceanic heat fluxes. Being able to scale the model allows to emulate ODE-type models and investigate which differences in these models result in the differing model dynamics reported in the literature (Thorndike, 1992; Eisenman and Wettlaufer, 2009; Notz, 2009). The understanding about significant contributing factors to model dynamics in this spatially confined model implementation is then used as a guide for the investigation of the dynamics of a retreating Arctic sea ice cover in a regional scale model.

In Chapter 2 a regular network model is introduced to study the ice albedo feedback. An approach to surface radiative forcing parametrizations is introduced. The validity of a

spatially confined model version is explored. The emergence of bistability under surface forcing and ice albedo changes with a step-like albedo parametrization is studied.

In Chapter 3 the longwave radiative forcing has been modified and based on a set of measurements from Barrow, AK and is compared to other longwave parametrizations used in ODE models. The importance of seasonally varying (instantaneous) surface forcing fixed-points for the existence of bistability is studied, and the interaction of model trajectories with the instantaneous fixed points is illustrated. The shape of the albedo parametrization close to the phase transition is identified as a significant inter-model difference resulting in reversible or irreversible sea ice retreat. Sharp step-like and more gradual albedo parametrizations, motivated by the differences observed in ODE models, are compared to local measurements and their impact on the asymptotic behavior on Arctic sea ice is investigated in the regular network model.

Chapter 4 describes a regular network model with a high resolution lateral extent (latitude 60° to 90° N) and vertical spatial resolution. The significance of the ice albedo parametrization to the dynamics of a receding ice cover is explored. A double-step albedo parametrization is introduced, based on gradients in albedo slightly before the phase transition as observed in measurements. The existence of a regime change from perennial to seasonal ice at the pole is investigated, and the signature of the regime change in model data is compared to measurements. An explanation is offered regarding the reasons why a sharp step-like albedo parametrization produces bistability in a spatially confined model, but not in a regional model.

The discussion in Chapter 5 sets the entirety of the results from Chapters 2 to 4 into the context of the literature on modeling approaches of Arctic sea ice retreat at differing scales. It is shown that the scalable model presented in this work offers connections between local effects, as observed in low order models, and how these effects apply to GCMs.

References

Armour, K, I Eisenman, E Blanchard-Wrigglesworth, K McCusker, and C Bitz (2011). "The reversibility of sea ice loss in a state-of-the-art climate model". In: *Geophysical Research Letters* 38.16.

Assur, A. (1958). "Arctic sea ice". In: National Academy of Sciences - National Research Council. Chap. Composition of sea ice and its tensile strength, pp. 106–138.

Bony, S, R Colman, V Kattsov, R Allan, C Bretherton, J Dufresne, A Hall, S Hallegate, M Holland, W Ingram, D Randall, B Soden, G Tselioudis, and M Webb (Aug. 2006). "How well do we understand and evaluate climate change feedback processes?" In: *Journal of Climate* 19, pp. 3445–3482.

Brigham, L (2007). "Thinking about the {A}rctic's future: Scenarios for 2040". In: *The Futurist* 51.5, pp. 27–34.

Budyko, M (1969). "The effect of solar radiation variations on the cliate of the Earth". In: *Tellus* 21.5, pp. 611–619.

Campbell and J Norman (1998). *Introduction to environmental biophysics*. Second. New York, NY: Springer Science+Business Media.

Cox, G and W Weeks (1983). "Equations for determining the gas and brine volumes in sea ice samples". In: *Journal of Glaciology* 29.102, pp. 306–316.

Crawford, T and C Duchon (Apr. 1999). "An improved parameterization for estimating effective atmospheric emissivity for use in calculating daytime downwelling longwave radiation". In: *Journal of Applied Meteorology* 38.4, pp. 474–480.

Curry, J and P Webster (1999). *Thermodynamics of atmosphere and oceans*. Academic Press.

Eisenman, I, N Untersteiner, and J Wettlaufer (May 2007). "On the reliability of simulated Arctic sea ice in global climate models". In: *Geophysical Research Letters* 34.10, pp. 1–4.

Eisenman, I and J Wettlaufer (Jan. 2009). "Nonlinear threshold behavior during the loss of Arctic sea ice". In: *PNAS* 106.1, pp. 28–32.

Esau, I (2007). "Amplification of turbulent exchange over wide Arctic leads: Large-eddy simulation study". In: *Journal of Geophysical Research* 112, p. D08109.

Frederking, R and G Timco (1984). "Measurement of shear strength of granular/discontinuous-columnar sea ice". In: *Cold Regions Science and Technology* 9.3, pp. 215–220.

Goff, J (1957). "Saturation pressure of water on the new Kelvin temperature scale". In: *Transactions of the American society of heating and ventilating engineers*, pp. 347–354.

Golden, K, S Ackley, and V Lytle (Dec. 1998). "The percolation phase transition in sea ice". In: *Science* 282.5397, pp. 2238–2241.

IPCC (2007). *Climate Change 2007: The physical science basis, summary for policymakers.* Tech. rep. Intergovernmental Panel on Climate Change.

Krembs, C and J Deming (2012). *Sea ice: a refuge for life in polar seas?* URL: http://www.arctic.noaa.gov/essay_krembsdeming.html (visited on 2011).

Leppäranta, M (2011). *The Drift of Sea Ice.* 2nd ed. Springer.

Massom, R, H Eicken, C Hass, M Jeffries, M Drinkwater, M Sturm, A Worby, X Wu, V Lytle, S Ushio, K Morris, P Reid, S Warren, and I Allison (2001). "Snow on Antarctic sea ice". In: *Review of Geophysics* 39.3, pp. 413–445.

Maykut, G and N Untersteiner (1971). "Some results from a time-dependent thermodynamic model of sea-ice". In: *Journal of Geophysical Research* 76, pp. 1550–1575.

Müller-Stoffels, M and H Eicken (2011). "Futures of Arctic Marine Transport 2030 - an Explorative Scenario Approach". In: *North by 2020: Perspectives on Alaska's Changing Social-Ecological Systems.* Ed. by H Eicken and A Lovecraft. University of Alaska Press.

Myhre, G, E Highwood, K Shine, and F Stordal (1998). "New estimates of radiative forcing due to well mixed greenhouse gases". In: *Geophysical Research Letters* 25.14, pp. 2712–2718.

North, G (1984). "Small Ice Cap Instability in Diffusive Climate Models". In: *Journal of the Atmospheric Sciences* 41.23, pp. 3390–3395. ISSN: 1520-0469.

Notz, D (Dec. 2009). "The future of ice sheets and sea ice: Between reversible retreat and unstoppable loss". In: *PNAS* 106.49, pp. 20590–20595.

Overeem, I, R Anderson, C Wobust, G Clow, F Urban, and N Matell (2011). "Sea ice loss enhances wave action at the Arctic coast". In: *Geophysical Research Letters* 38.17, pp. 1–6.

Peixoto, J and A Oort (1992). *Physics of Climate.* Woodbury, NY, USA: AIP Press.

Perovich, D, T Grenfell, B Light, and P Hobbs (Oct. 2002). "Seasonal evolution of the albedo of multiyear Arctic sea ice". In: *Journal of Geophysical Research* 107.C10.

Prata, A (July 1996). "A new long-wave formula for estimating downward clear-sky radiation at the surface". In: *Quarterly Journal of the Royal Meteorological Society* 122.533, pp. 1127–1151.

Randal, D, ed. (2000). *General circulation model development.* Vol. 20. San Diego, CA, USA: Academic Press.

Satterlund, D (1979). "An improved equation for estimating long-wave radiation from the atmosphere". In: *Water Resources Research* 15.6, pp. 1649–1650.

Sellers, W (1969). "A global climatic model based on the energy balance of the Earth-atmosphere system". In: *Journal of Applied Meteorology* 8, pp. 392–400.

Shine, K and A Henderson-Sellers (1985). "The sensitivity of a thermodynamic sea ice model to changes in surface albedo parameterization". In: *Journal of Geophysical Research* 90.D1, pp. 2243–2250.

Siegel, R and J Howell (1992). *Thermal Radiation Heat Transfer*. 3rd. Washington: Hemisphere Publishing Corporation.

Stroeve, J, M Holland, W Meier, T Scambos, and M Serreze (2007). "Arctic sea ice decline: Faster than forecast". In: *Geophysical Research Letters* 34, p. L09501. DOI: doi:10.1029/2007GL029703, 2007.

Thomas, D and G Dieckmann (2003). *Sea Ice: An Introduction to physics, chemistry, biology and geology*. Malden, MA 02148-5020, USA: Blackwell Science Ltd.

Thorndike, A (June 1992). "A toy model linking atmospheric and thermal radiation and sea ice growth". In: *Journal of Geophysical Research* 97.C6, pp. 9401–9410.

Walker, G (2006). "The tipping point of the iceberg". In: *Nature* 441, p. 802.

Winton, M (2008). "Sea-ice albedo feedback and nonlinear Arctic climate change". In: *Arctic sea ice decline: observations, projections, mechanisms, and implications*. Ed. by C. M. Bitz E. T. DeWeaver and L. B. Tremblay. American Geophysical Union, pp. 111–131.

Chapter 2

Regular network model for the sea ice-albedo feedback in the Arctic[1]

2.1 Abstract

The Arctic Ocean and sea ice form a feedback system that plays an important role in the global climate. The complexity of highly parameterized global circulation (climate) models makes it very difficult to assess feedback processes in climate without the concurrent use of simple models where the physics is understood. We introduce a two-dimensional energy-based regular network model to investigate feedback processes in an Arctic ice-ocean layer. The model includes the nonlinear aspect of the ice-water phase transition, a nonlinear diffusive energy transport within a heterogeneous ice-ocean lattice, and spatiotemporal atmospheric and oceanic forcing at the surfaces. First results for a horizontally homogeneous ice-ocean layer show bistability and related hysteresis between perennial ice and perennial open water for varying atmospheric heat influx. Seasonal ice cover exists as a transient phenomenon. We also find that ocean heat fluxes are more efficient than atmospheric heat fluxes to melt Arctic sea ice.

2.2 Abstract - General audience

Thinning and retreating Arctic sea ice during recent decades point to a warming climate in the Arctic. Global circulation (climate) models (GCMs) are currently the primary tool used to project climate over the next century. While they describe large-scale interactions between oceans, landmasses and atmosphere reasonably well, they are too complex and computationally too expensive to understand isolated climate subprocesses. We introduce a complex systems model to investigate the short- and long-term behavior of model Arctic sea ice. A lattice of ice-ocean cells is driven by radiative atmospheric and oceanic heat influxes; the cells can undergo an ice-water phase transition and transport energy. We find that the longterm behavior for a horizontally homogeneous ice-ocean layer is either perennial ice cover or perennial open water. Seasonal ice can exist as transient behavior. A lack of reversibility in the system implies that significant cooling has to take place for an ice cover to re-establish once it is lost. We also find that heat entering at the bottom of the ice

[1]This chapter is published as: Müller-Stoffels, M and R Wackerbauer, *Regular network model for the sea ice-albedo feedback in the Arctic*, Chaos **21**, 013111, 2011.

sheet is more efficient than atmospheric heat influxes to melt Arctic sea ice, indicating that the understanding of ocean currents is crucial to the understanding of retreating Arctic sea ice.

2.3 Introduction

The Arctic Ocean and sea ice form a feedback system that plays an important role in the global climate. Variations of the global ice and snow distribution have a significant effect on the planetary albedo. This is because snow and ice efficiently reflect incident short wave radiation while open water absorbs most incident short wave radiation (Peixoto and Oort, 1992; Thomas and Dieckmann, 2003). Hence, the melting of large portions of sea ice will have an impact on the Arctic and on the global climate (Barry et al., 1993; Bony et al., 2006), since more open water absorbs a higher portion of solar energy, which in turn melts more ice and generates more open water (ice-albedo feedback system).

Retreating summer sea ice during recent decades with record lows in ice extent (Stroeve et al., 2005; Walker, 2006; National Oceanic and Atmospheric Administration (NOAA), 2009) as well as the thinning of the Arctic sea-ice at a remarkable rate over the past few decades (Rothrock, Yu, and Maykut, 1999; Bitz and Roe, 2004) strongly indicate a warming climate in the Arctic. Significant modeling efforts are undertaken to gain insight into whether Arctic sea ice will be perennial, seasonal or completely gone in the near future. The Arctic ocean, sea ice, and atmosphere make up a highly complex thermodynamic dynamical system, which includes many subprocesses, such as cloud formation, precipitation, melt pond formation, and lead and pressure ridge formation (Peixoto and Oort, 1992; Thomas and Dieckmann, 2003). A good physical understanding of climate feedbacks is lacking (Bony et al., 2006), and parameterization of processes is usually necessary to capture subgrid scale phenomena.

Global circulation models (GCMs) are currently the primary tool used to project climate over the next century. One strength of these models is that they are very sophisticated and include many climate components, although often in form of parameterization. About twenty GCMs were evaluated in the Fourth Assessment Report of the Intergovernmental Panel on Climate Change (IPCC). All of these GCMs were simulating present-day sea ice conditions in reasonable agreement with observations (Parkinson, Vinnikov, and

Cavalieri, 2006). A recent study (Eisenman, Untersteiner, and Wettlaufer, 2007) shows that the same GCM simulations for the IPCC report also display large inter-model differences in Arctic cloud cover, which are associated with significant differences in downwelling longwave radiation. These differences cause large ice thickness variations between 1m to more than 10m. This study further revealed that the ice-albedo parameter would need to be tuned by only 0.1 if this parameter alone were used to compensate the effects of the differences in longwave radiation and to explain the inter-model agreement in simulated present-day sea ice (Eisenman, Untersteiner, and Wettlaufer, 2007; DeWeaver, Hunke, and Holland, 2008; Eisenman, Untersteiner, and Wettlaufer, 2008). This example demonstrates that one has to be cautious when assessing GCMs (and complex models with lots of components, in general); it is also consistent with the remark by Bony et al (Bony et al., 2006) that the complexity of climate models (GCMs) makes it very difficult to assess feedbacks. In addition GCMs are computationally too expensive to perform extensive parameter variations to understand climate and subsystems of the climate.

The other class of commonly used models represents one-dimensional sea-ice models (ordinary differential equations) (Thorndike, 1992; Curry, Schramm, and Ebert, 1995; Björk and Sönderkvist, 2002; Eisenman, Untersteiner, and Wettlaufer, 2007; Eisenman and Wettlaufer, 2009) that necessarily assume that the Arctic is spatially homogeneous unless several column models are used. These thermodynamic models focus on subsystems of the climate to derive understanding for simple model feedback processes, and are based upon pioneering work by Untersteiner (Untersteiner, 1964) and Maykut (Maykut and Untersteiner, 1971). Thorndike showed (Thorndike, 1992) in a one-dimensional model of Arctic sea ice that the only stable solutions are either a permanent ice cover in most of the Arctic ocean or no ice cover. Recently, an extension of this model (Eisenman and Wettlaufer, 2009) revealed that a seasonal ice cover could be stable too, if ice export is taken into account. The coupled column model of ice, ocean, atmosphere by Bjork and Sonderkvist (Björk and Sönderkvist, 2002) reveals that the ice cover is highly sensitive to the poleward energy flux, with the ice thickness decreasing drastically for fluxes above a critical value.

Hierarchical modeling is necessary to improve the understanding of complex climate processes and feedbacks. It is not possible to tease out the complex feedbacks in a highly parameterized full GCM without the concurrent use of simple models where the physical

processes can be understood (Bony et al., 2006). We have developed a two-dimensional (vertical) energy-based lattice model to investigate transient and asymptotic behavior of thermodynamic processes in an Arctic sea ice and ocean system. The model includes the nonlinear aspect of the ice-water phase transition, a nonlinear diffusive energy transport within a heterogeneous ice-ocean lattice, and spatiotemporal atmospheric and oceanic forcing at the boundaries. The network structure of the ice-ocean lattice easily allows to implement spatial and temporal heterogeneities in the albedo and in the local diffusivities that are caused by the presence of water, ice, and snow. The model is introduced in Sect. II. First results for a horizontally homogeneous ice-ocean layer are discussed in Sect. III, including bistability between perennial ice and perennial open water, related hysteresis, and transient seasonal ice cover.

2.4 Model

We introduce a complex systems model to investigate thermodynamic feedback processes in an Arctic ice-ocean layer (Fig. 2.1). The ice-ocean layer is represented as a regular network (lattice) of diffusively coupled cells (model domain). The state of each cell is determined by its energy content $E_{i,j}$, which also defines the phase of the cell (solid, liquid). Each cell can exchange energy with its nearest neighbors via nonlinear diffusive coupling. Since energies are transported faster in ice than in open water, the local diffusion constants differ as they depend on the phase of the cell. The ice-ocean layer interacts with the atmosphere; atmospheric heat fluxes (down and upwelling longwave radiation, shortwave solar radiation, and lateral heat fluxes from lower latitudes) are entering the upper surface (top row) as a spatiotemporal drive. Ocean heat fluxes provide a drive to the cells in the bottom row of the ice-ocean layer.

Various studies show that the collective time evolution of large networks of nonlinear dynamical elements is often dominated by the coupling properties rather than by the dynamical details of the elements as long as some core nonlinear characteristic physics is captured at the local scale (Cross and Hohenberg, 1993; Pecora and Hohenberg, 1998). In this sense we are not concerned with a complete description of the underlying thermodynamics of sea-ice growth, like the influence of brine on the growth and solidification

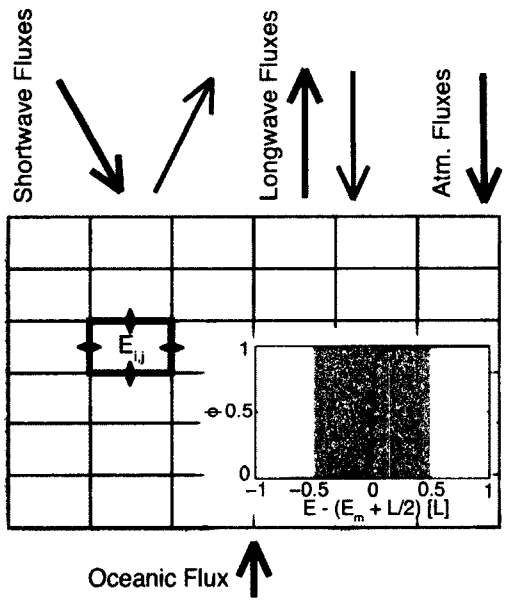

Figure 2.1. The thin vertical ice-ocean layer is modeled by a regular network of diffusively interacting ice-ocean cells. The state of each cell is given by its energy content $E_{i,j}$, which also defines the phase of the cell (ice, water). Each cell can exchange energy with its nearest neighbors via state-dependent nonlinear diffusion. Atmospheric heat fluxes are entering at the upper surface (top row), and oceanic heat fluxes are entering at the bottom row of the ice-ocean layer. The inset shows the steplike phase transition between ice ($\Phi = 0$) and water ($\Phi = 1$) and the gradual release of latent heat L as the energy of a cell increases (shaded area).

of sea ice [2] (Weeks and Hibler, 2010; Golden, Ackley, and Lytle, 1998; Thomas and Dieckmann, 2003). At the local scale the model considers the core nonlinear process of freezing and melting and the associated release and absorption of latent heat. At the global scale the model considers interacting ice-water cells with heterogeneous and nonlinear diffusive energy transport properties and subject to a nonlinear spatiotemporal drive.

2.4.1 Model equations

The *state of a cell* (i,j) at temperature T is determined by its total energy content $E_{i,j}$,

$$E_{i,j} = e_{i,j} + L\phi(E_{i,j}), \quad i = 1,..,N; j = 1,..,M. \tag{2.1}$$

$e_{i,j}$ is the amount of sensible heat (thermal energy without latent heat that is directly accessible to temperature changes), and L is the volumetric latent heat of fusion [3] . The physical constants and fixed system parameters used in this paper are summarized in reference [4] . $\phi(E_{i,j})$ is a phase factor that controls the liquid-solid phase transition; it is chosen to follow a smooth step-like function,

$$\phi(E_{i,j}) = \frac{1}{\pi}\arctan[c(E_{i,j} - E_m - \frac{L}{2})] + \frac{1}{2}, \tag{2.2}$$

that is centered at the middle of the latent heat release (inset of Fig. 2.1). The melting energy, $E_m = C_I h^3 T_0$, refers to the energy content of a cell of ice at temperature $T_0 = 273K$, with C_I the volumetric heat capacity of ice, and h the dimension of the cubic cell. The

[2] Thermodynamic processes in sea ice are distinctly different from those in fresh water ice, since sea ice grows from a solution of water and various ions. Many of the physical variables depend on temperature, salinity or the age of the ice (Weeks and Hibler, 2010). The phase transition does not occur suddenly, that is, a volume of sea ice at the generally accepted freezing point of about -1.8 °C does contain a considerable fraction of brine, which will solidify at lower temperatures (Golden, Ackley, and Lytle, 1998; Golden, 2001). Nonetheless, the core process of freezing and melting is similar to that of a pure water system in that during freezing latent heat is released and during melting latent heat is absorbed.

[3] The volumetric latent heat of fusion is calculated as $L = lh^3\frac{\rho_I+\rho_W}{2}$, with l the latent heat of fusion, h the dimension of a cubic cell, and $\rho_{I/W}$ the densities of ice/water. Temperature dependent density changes are ignored, except averaging over the density of water ρ_W and the density of ice ρ_I during the release of latent heat L. $L = 8.6710^6 J$ for a single cell.

[4] Physical constants and fixed system parameters used in this paper: size of ice-ocean layer: $N = 16, M = 100$; dimension of cubic cell $h = 0.3m$; sharpness factor $c = 10^{-5}$; density of water $\rho_W = 1000kg/m^3$; density of ice $\rho_I = 917kg/m^3$; latent heat of fusion $l = 3.3510^5 J/kg$; volumetric heat capacity of water $C_W = 4.1810^6 J/(m^3K)$; volumetric heat capacity of ice $C_I = 1.9310^6 J/(m^3K)$; coupling constant $\zeta = 1.6 \times 10^5 s/m^2$; thermal conductivity of water $k_W = 0.6W/(mK)$; thermal conductivity of ice $k_I = 2.2W/(mK)$, atmospheric transmittance $\tau = 0.7$, albedo of open water $\alpha_W = 0.07$, latitude $\Phi = 80°N$.

sharpness of the phase transition is determined by c. In the asymptotic case, the phase factor is $\Phi = 0$ for ice and $\Phi = 1$ for water. These asymptotic values are reached within 1% at the beginning ($E_{i,j} = E_m$) and at the end of the latent heat release ($E_{i,j} = E_m + L$) for a sharp phase transition with $c = 10^{-5}$.

The energy content of a cell in the solid phase is converted into temperature with $E_{i,j} = C_I h^3 T$ and $T \leq T_0$, and in the liquid phase the energy is converted with $E_{i,j} = E_m + L + C_W h^3 (T - T_0)$ and $T > T_0$. For energies during the phase transition $E_m \leq E_{i,j} \leq E_m + L$ the temperature is constant at $T = T_0$.

The *time evolution of the energy content of a cell* in a two-dimensional vertical ice-ocean layer is modeled as a driven and diffusively coupled map lattice,

$$\begin{aligned} E_{i,j}^{n+1} &= E_{i,j}^{n} \\ &+ \zeta \sum_{k=-1}^{1} D_{[i,i+k],j}(E_{i+k,j}^{n} - E_{i,j}^{n}) \\ &+ \zeta \sum_{k=-1}^{1} D_{i,[j,j+k]}(E_{i,j+k}^{n} - E_{i,j}^{n}) \\ &+ \delta_{1i}\zeta h^4 (R_{SW} + R_{LW} + F_a) + \delta_{Ni}\zeta h^4 F_o. \end{aligned} \tag{2.3}$$

The energy content $E_{i,j}^{n+1}$ of cell (i,j) at discrete time $n+1$ depends on the energy content $E_{i,j}^{n}$ of this cell at the previous time step n ($n \in \mathrm{N}_0$) and on the gradient-driven energy transport between neighboring cells. D refers to a heterogenous and nonlinear diffusion constant. Radiative and atmospheric heat fluxes provide a spatiotemporal drive to the cells in the upper surface ($i = 1$) of the ice-ocean layer; they include solar shortwave radiation flux density R_{SW}, longwave radiative flux balance density R_{SW}, and lateral atmospheric flux density F_a. R_{SW} as well as R_{LW} depend on the state of the cell $E_{i,j}$. The ocean heat flux density F_o provides a spatiotemporal drive to the cells in the bottom surface ($i = N$) of the ice-ocean layer. δ_{ij} represents the Kronecker delta, and ζ is a global coupling constant [5] . For a cell at a boundary only energy gradients to its linked neighboring cells enter into Eq. (2.3).

Nonlinear and heterogeneous diffusivities govern the energy transport within the ice-ocean

[5]The global coupling constant $\zeta = \frac{\Delta t}{h^2} = 1.6 \times 10^5 s/m^2$ (with a cell dimension of $h = 0.3m$ and a time step of $\Delta t = 4h$) used for the coupled map lattice in this paper corresponds to (but must not be limited to) the discretized energy diffusion equation (PDE) for constant diffusivities.

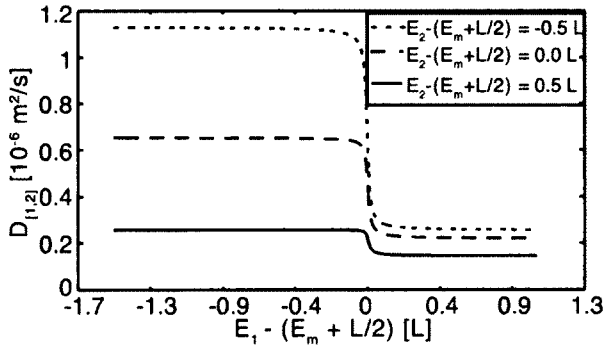

Figure 2.2. The diffusivity $D_{[1,2]}$ between two cells, labeled 1 and 2, as a function of the energy E_1 of cell 1 in the neighborhood of the phase transition. The energy E_2 of cell 2 is at the melting energy $E_2 = E_m$ (dotted line), in the middle of the phase transition $E_2 = E_m + L/2$ (dashed line), and immediately after the release of latent heat $E_2 = E_m + L$ (full line). Since only two cells are considered, the index j in Eq. (2.5) is neglected.

layer. The local thermal diffusion constant $D_{i,j}$ within a cell (i,j) depends nonlinearly on the state $E_{i,j}$ according to

$$D_{i,j} = \frac{k_I + (k_W - k_I)\cdot\phi(E_{i,j})}{C_I + (C_W - C_I)\cdot\phi(E_{i,j})}, \tag{2.4}$$

where $k_{I/W}$ are the thermal conductivities of ice/water. If neighboring cells are in different states, the local diffusivities are determined from a superposition of thermal conductances (Campbell and Norman, 1998). This leads to following diffusivity $D_{[i_1,i_2],j}$ between two cells, (i_1,j) and (i_2,j):

$$D_{[i_1,i_2],j} = 2\frac{D_{i_1,j}D_{i_2,j}}{D_{i_1,j} + D_{i_2,j}}. \tag{2.5}$$

The diffusivities $D_{i,[j_1,j_2]}$ between two neighboring horizontal cells follow in analogy by transposition. Figure 2.2 shows the diffusivity $D_{[1,2]}$ [neglecting the index j in Eq. (2.5)] between two cells, labeled 1 and 2, for states in the neighborhood of the liquid-solid phase transition. The diffusivity can differ up to a factor of eight. It is highest, if adjacent cells are both frozen [$E_i - (E_m + L/2) < 0$, and $i = 1,2$)], and diminishes rapidly with the onset of melting until its lowest value is reached when adjacent cells are both liquid [$E_i - (E_m + L/2) > 0$, and $i = 1,2$]. From Eqs. (2.4) and (2.5) follows the asymptotic value for the diffusivity between two frozen cells with phases $\Phi = 0$ as $D_{[1,2]} = k_I/C_I$ and in analogy between two liquid cells with phases $\Phi = 1$ as $D_{[1,2]} = k_W/C_W$; the diffusivity between one liquid and one

frozen cell in the asymptotic case of $\Phi(E_1) = 1$ and $\Phi(E_2) = 0$ is $D_{[1,2]} = \frac{2k_I k_W}{k_I C_W + k_W C_I}$. Figure 2.2 also shows that for a fixed energy E_2 the diffusivity $D_{[1,2]}$ is rather constant over a range of energies E_1, i.e. the asymptotic values are "reached" close to the center of the phase transition where $E_1 - (E_m + L/2) \approx 0$.

2.4.2 Spatiotemporal Drive

Atmospheric heat fluxes provide a spatiotemporal drive to the cells in the upper surface of the ice-ocean layer [Eq. (2.3)], including main features of longwave radiative flux balance, the absorbed solar shortwave radiative flux balance, and lateral atmospheric heat fluxes entering from lower latitudes. Ocean heat fluxes enter at the bottom of the ice-ocean layer (Fig. 2.1).

The *longwave radiative flux balance density* R_{LW} is determined from the difference of thermal radiation emitted from the atmosphere and emitted from the surface of the ice-ocean layer,

$$R_{LW} = [\varepsilon_a(T) - \varepsilon_s]\sigma T^4, \tag{2.6}$$

with surface temperature T and Stefan Boltzmann constant σ. Sea ice and ocean are near perfect blackbody emitters, and their thermal radiation can be calculated from Stefan-Boltzmann's law for greybody emitters with $\varepsilon_s = 0.96$ being a good approximation for sea ice's and ocean's surface emissivity. The emissivity of the atmosphere $\varepsilon_a(T)$ depends on spatiotemporal variations in emissivity due to cloud cover, water vapor pressure, temperature and local pressure, and is a topic of much debate (Campbell and Norman, 1998; Bony et al., 2006). We limit our model to clear sky conditions [6] and calculate the emissivity $\varepsilon_a(T)$ for a water air mixture (Siegel and Howell, 1992),

$$\varepsilon_a = a_0 \left[1 - \exp\left(-a_1 \left(\frac{p_w L_e 300 (p_a + b p_w)}{T} \right)^{\frac{1}{2}} \right) \right]. \tag{2.7}$$

$p_w[atm]$ is the saturation vapor pressure [Eq. (2.8)], and p_a is assumed to be the standard atmospheric pressure ($p_a = 1atm$). $a_0 = 0.683$ and $a_1 = 1.17$ are empirical coefficients for $T = 300K$, $b = 5(300/T)^{1/2} + 0.5$ is the self-broadening coefficient for water vapor, and L_e is the mean beam length of the gas ($L_e = 40m$).

[6] Assuming surface temperature for the atmosphere's longwave radiation in Eq. (2.6) corresponds to an effective cloud cover, as actual clear sky would have a temperature around $T = 5K$.

The saturation vapor pressure p_w that is entering into Eq. (2.7) is calculated from the World Meteorological Organizations recommended parameterization by Goff (1957)[7],

$$\begin{aligned} \log_{10} p_w &= 10.79574(1 - 273.16/T) \\ &- 5.02800 \log_{10}(T/273.16) + 0.78614 \\ &+ 1.50475 \times 10^{-4}(1 - 10^{8.2969(T/273.16-1)}) \\ &+ 0.42873 \times 10^{-3}(10^{4.76955(1-273.16/T)} - 1), \end{aligned} \tag{2.8}$$

where temperature T is in K and the vapor pressure p_w is in hPa.

Figure 2.3 (a) shows a steep increase of the atmospheric emissivity ε_a as a function of the surface cell energy E in an energy interval of about $2L$ around the phase transition. Only slight changes in surface cell energy can strongly influence the sky's emissivity. Outside of this energy interval as well as during the phase transition, ε_a is rather independent of changes in energy content. Figure 2.3(b) illustrates that the longwave radiative flux balance density R_{LW} [Eq. (2.6)] is negative for all surface cell energies (and in analogy for all surface temperatures). This drive alone would lead to a completely frozen ice-ocean layer. The figure also reveals a weak local minimum around the phase transition (i.e. around the freezing temperature T_0) [8] . This corresponds to a stabilizing effect of the longwave radiative balance on the energy budget of the ice-ocean layer, especially during the Arctic night where solar (shortwave) radiation is absent. Below the phase transition [Fig. 2.3(b)], longwave radiative losses become smaller (R_{LW} increases) as the surface gets colder. Above the phase transition, the longwave radiative losses decrease also (R_{LW} increases locally) as the surface warms slightly before increasing rapidly. This increase indicates a stable state in the liquid phase [9] .

[7] Parameterizations for saturation vapor pressure over ice and water differ, but they are negligibly small in the temperature range considered here (Goff, 1957). We further assume that the atmosphere is saturated with water vapor at the interface between atmosphere and ice-ocean layer.

[8] A weak local minimum in R_{LW} around the freezing temperature T_0 was also reported by Thorndike (Thorndike, 1992) in a significantly different model. Instead of an atmospheric spatiotemporal drive acting on an extended ice-ocean layer, Thorndike uses an atmospheric model coupled to a 1-dimensional ice-ocean model.

[9] A qualitative argument for the stable state in the liquid phase is presented. If solar radiation is assumed to be constant in time (e.g. replaced with its yearly average), the total drive is given by a shift in R_{LW} [Fig. 2.3(b)] such that it vanishes at three discrete energies. In the spatially homogeneous case a zero drive yields $E_{i,j}^{n+1} = E_{i,j}^{n}$ in Eq. (2.3). The fixed point with $E - (E_m + L/2) > 1$ is stable due to the negative slope of the shifted R_{LW}-curve in this E-regime. In addition simulations of Eq. (2.3) reveal a stable asymptotic cycle for OW in the "$\Delta E/\Delta t$

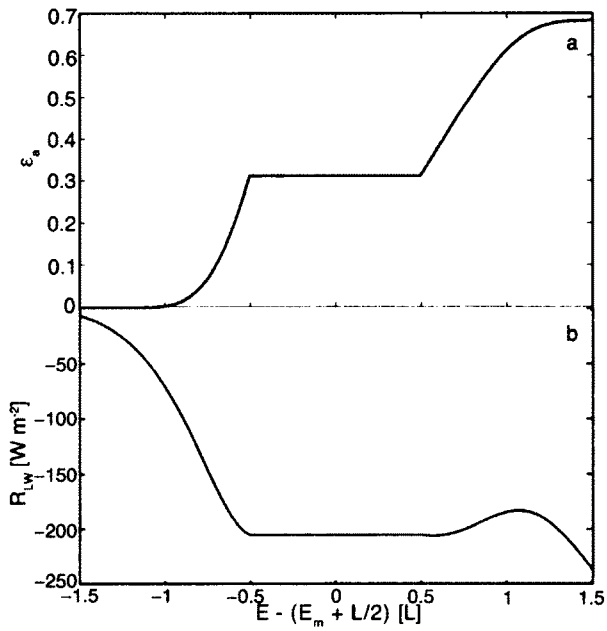

Figure 2.3. Atmospheric emissivity and longwave radiative flux balance. (a) Atmospheric emissivity ε_a versus energy content E of a cell, calculated from Eqs. (2.7, 2.8) with $p_a = 1atm$, $a_0 = 0.683$, $a_1 = 1.17$, $b = 5(300/T)^{1/2} + 0.5$, $L_e = 40m$. (b) Longwave radiative flux balance density R_{LW} in relation to surface cell energy E, following Eq. (2.6). The horizontal part of the graphs in (a) and (b) indicate the phase transition. ε_a and R_{LW} are T-dependent and therefore not affected by the energy change due to latent heat release during the phase transition. The conversion between temperature and energy is given in Sect. II A.

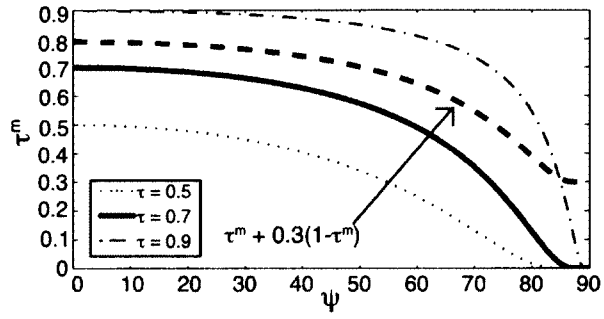

Figure 2.4. Atmospheric attenuation factor τ^m for direct solar radiation flux density in Eq. (2.9) versus zenith angle ψ for different atmospheric transmittances τ. Standard atmospheric pressure $p_a = 101.3kPa$ was used for the optical air mass number m in Eq. (2.10). The curve marked with an arrow corresponds to the total attenuation factor $\tau^m + 0.3(1-\tau^m)$ for direct and diffuse solar radiation flux density [Eq. (2.9)] with $\tau = 0.7$. The bold lines correspond to the parameter used in this paper ($\tau = 0.7$).

Incoming solar radiation onto the surface of the ice-ocean layer is considerably reduced due to scattering in the atmosphere. The *solar shortwave radiation flux density* R_{SW} that is absorbed at the surface of the ice-ocean layer is given by (Campbell and Norman, 1998)

$$R_{SW} = (1-\alpha)S_{p0}[\tau^m + 0.3(1-\tau^m)]. \tag{2.9}$$

$(1-\alpha)$ is the portion of incoming solar radiative flux density that is absorbed at the surface of the ice-ocean layer, and α is the surface albedo [10] . $S_{p0} = S_0 \cos\psi$ is the extraterrestrial solar flux density on a surface perpendicular to the incoming flux; it depends on the zenith angle ψ ($\psi \leq 90°$) [11] and the solar constant $S_0 = 1367W/m^2$.

The factor in square brackets in Eq. (2.9) describes the interaction of the solar radiation with the atmosphere (Campbell and Norman, 1998). Due to scattering processes only a portion τ^m of the extraterrestrial solar flux density S_{p0} reaches the surface of the earth

vs E'' phase space (Δt = 1 day). An analogous argument and simulation holds for the stable state in the solid phase.

[10]The spectral albedo $\alpha(\lambda)$ for a given wave length λ is defined as the ratio of reflected $R^{\uparrow}_{SW}$ to incoming $R^{\downarrow}_{SW}$ shortwave solar radiation, $\alpha(\lambda) = \frac{R^{\uparrow}_{SW}(\lambda)}{R^{\downarrow}_{SW}(\lambda)}$. The albedo α used throughout the paper is defined as the integral of the spectral albedo over the solar shortwave radiation spectrum.

[11]Diffuse solar radiation received during twilight ($\psi \in [90°, 96°]$) and corresponding corrections to the formula for the extraterrestrial solar flux density S_{p0} are neglected. In addition, the error in omitting the eccentricity e in the extraterrestrial solar flux density, $S_{p0} = S_0 e \cos\psi$, is considered small since $e \in [0.97, 1.03]$.

directly as attenuated solar beam (direct solar radiation flux density). The other portion $1-\tau^m$ of the extraterrestrial solar flux density is scattered diffusely in all directions; it is assumed that 30% of the diffuse solar radiation flux density eventually reaches the surface of the earth.

τ represents the atmospheric transmittance. The optical air mass number m refers to an effective path length of the solar radiation through the atmosphere and depends on the zenith angle ψ,

$$m = \frac{p_a}{101.3\cos\psi}, \tag{2.10}$$

where p_a is the atmospheric pressure in kPa (we use standard pressure, $p_a = 101.3kPa$).

Figure 2.4 shows the decrease of direct solar radiation flux density with zenith angle ψ, as it is expressed in the attenuation factor τ^m for the earth's surface. It also reveals that diffuse solar radiation plays an important role in the shortwave energy budget at high zenith angles, i.e. when the sun is low above the horizon. While diffuse solar radiation could be ignored for lower latitudes, it cannot be discarded for the Arctic region where high zenith angles are very common early and late during the Arctic day.

The solar shortwave component R_{SW} of the spatiotemporal drive is explicitly time dependent due to the annual and daily cycle of the zenith angle. The zenith angle ψ depends on the declination angle δ, the latitude Φ, the time of day $t[h]$, and the time of solar noon $t_0[h]$,

$$\cos\psi = \sin\Phi\sin\delta + \cos\Phi\cos\delta\cos[15(t-t_0)]. \tag{2.11}$$

Since solar time is considered in this paper, solar noon occurs at $t_0 = 12$ hours. The factor 15 converts solar time to hour angles. Zenith angles greater than 90° mean the sun is below the horizon. The declination angle δ is calculated through the empirical equation

$$\sin\delta = 0.39785 \times \tag{2.12}$$
$$\sin[278.97 + 0.9856J + 1.9165\sin(356.6 + 0.9856J)],$$

where J is the number of the calendar day.

The solar shortwave radiation flux density R_{SW} in Eq. (2.9) is also evolving in time since the surface albedo α depends on the state $E_{i,j}$ of the cell,

$$\alpha = \alpha_I + (\alpha_W - \alpha_I)\phi(E_{i,j}). \tag{2.13}$$

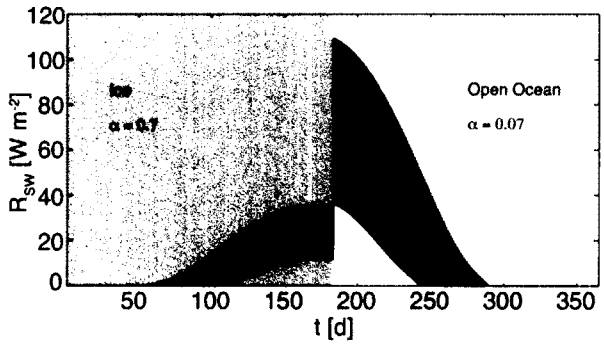

Figure 2.5. Annual cycle of the solar shortwave radiative flux density R_{SW} [Eq. (2.9)] at the surface of an ice-ocean layer at latitude $\Phi = 80°N$. For the first half of the year (shaded gray) an ice covered ocean ($\alpha = 0.7$) was assumed, and for the second half an open ocean with albedo $\alpha = 0.07$. The black bands mark the minimum and maximum of the daily oscillations in R_{SW}. For a constant albedo throughout the year, either of the black bands would be symmetrically continued/mirrored into the other half of the year.

$\alpha_{I/W}$ represent the albedo for ice/water[11] . Sea ice is reflecting a large portion of the incoming solar radiation, its albedo α_I is relatively high with empirical values between 0.5 and 0.9. Open water absorbs nearly all solar radiation, and its albedo is very low, $\alpha_W = 0.07$. These albedo values are based on empirical data integrated over the visible spectrum (Eicken, 2003).

Figure 2.5 shows an annual cycle of absorbed solar shortwave radiative flux density R_{SW} [Eq. (2.9)] at the earth's surface at latitude $80°N$. An ice covered surface with $\alpha = 0.7$ was assumed for the first half of the year (shaded gray), and open water surface with $\alpha = 0.07$ was assumed for the second half. The energy uptake of open ocean is up to a factor of 4 larger. The seasonality of the shortwave energy budget is obvious in the figure, starting with zero absorbed solar radiation during the Arctic night (sun below horizon), and followed by oscillating, but permanent, solar radiation during the Arctic day.

The spatiotemporal drive at the top surface of the ice-ocean layer further includes the *lateral atmospheric heat flux density* F_a(Fig. 2.1), which represents heat sources entering from lower latitudes. This component of the drive currently enters into the model [Eq. (2.3)] as a system parameter. Ocean heat fluxes provide a drive to the cells in the bottom row of the ice-ocean layer (Fig. 2.1). The *ocean heat flux density* F_o represents the energy source

due to warmer (non-freezing) ocean temperatures below the ice-ocean layer as well as lateral ocean heat sources from lower latitudes. All ocean heat flux densities are currently represented by the parameter F_o. Lateral atmospheric heat flux density F_a and oceanic heat flux density F_o are a major component to the total heat budget of the Arctic region (Serreze et al., 2007). Atmospheric heat flux densities for the Arctic are usually on the order of $100W/m^2$, while oceanic heat flux densities are on the order of $1W/m^2$.

Figure 2.6 shows a typical annual cycle of the *total surface radiative drive* R_S, including longwave, shortwave and lateral atmospheric heat flux densities, $R_S = R_{LW} + R_{SW} + F_a$ [Eq. (2.3)]. All cells of the ice-ocean layer were initially below but close to the solid-liquid phase transition, with a linear vertical energy profile and a homogeneous horizontal energy distribution. At the beginning of the annual cycle the sun is below the horizon (Arctic night), and the total surface radiative drive is negative and rather constant; this is due to negligible changes in surface temperature that yield a rather robust longwave radiative energy loss and due to constant positive lateral atmospheric heat fluxes. After about 50 days, R_S starts to significantly increase and to oscillate due to the solar shortwave radiation R_{SW} when the sun is permanently above the horizon during the Arctic day ($80°N$). Accompanied by this is a slightly decreasing albedo α (Fig. 2.6), with the surface still frozen, $\alpha \approx \alpha_I$. At about 170 days there is a sharp increase in total surface heat influx due to the phase transition of the surface from ice to water; clearly more solar radiation is absorbed as the albedo decreases [Eq. (2.9)]. After about 170 days the high total surface radiative drive gradually decreases due to the change of the solar path (zenith angle) until the Arctic night is reached with a relatively constant total heat loss. A comparison of Figs. 2.5 and 2.6 shows that during the Arctic day the total surface radiative forcing R_S resembles the shortwave radiative budget R_{SW}, while during the Arctic night the heat flux remains relatively constant.

This model was designed to systematically explore a variety of physical parameters and spatiotemporal inhomogeneities. The network structure of the dynamical elements close to the ice-water phase transition allows to introduce spatial and temporal inhomogeneities due to different types of ice cover, snow cover, or melt ponds; the spatiotemporal atmospheric and oceanic drive can cover inhomogeneities due to cloud cover or ocean currents. As a first step however, the dynamics needs to be understood in more simple

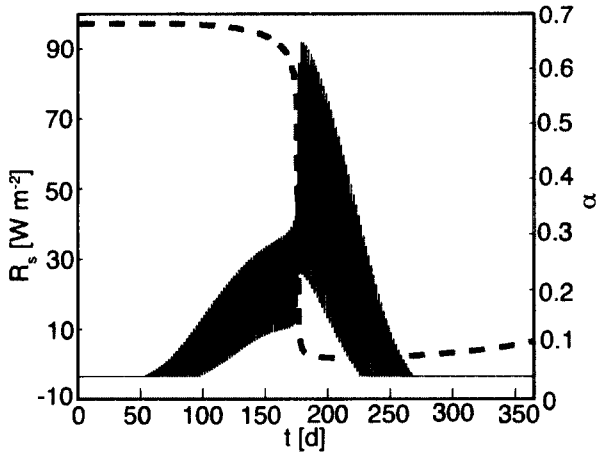

Figure 2.6. Total surface radiative drive, $R_S = R_{LW} + R_{SW} + F_a$ [Eq. (2.3), solid line] for a typical annual cycle with melting surface ice. The corresponding surface albedo α [Eq. (2.13), dashed line] is plotted on the right axis. A vertically linear and horizontally homogeneous energy profile was considered as initial condition, with $E_{1,j} = E_m - 0.0819L$ in the top row, and $E_{16,j} = E_m - 0.0493L$ in the bottom row of the ice-ocean layer ($N = 16$, $M = 100$). Other system parameters are $\alpha_I = 0.7$, $F_a = 185.25W/m^2$, and $F_o = 0.1W/m^2$ besides the standard parameters[4] in this paper.

situations (Sect. 2.5) that can be compared to relevant findings in one-dimensional analytical and numerical models (Thorndike, 1992; Eisenman, Untersteiner, and Wettlaufer, 2007; Eisenman and Wettlaufer, 2009). The model also fulfills the following benchmarks: (i) the energy is conserved in a closed system, and (ii) the ice thickness follows a Stefan-Model-like ice growth (Carslaw and Jaeger, 1959), i.e. the ice thickness increases as the square root of time under constant heat input at the bottom and constant heat removal at the top of the grid.

Several studies of the Arctic sea ice (Björk and Sönderkvist, 2002; Eicken, 2003; Bitz and Roe, 2004; Bony et al., 2006) motivate the variation of following relevant physical parameters in the model. Lateral atmospheric heat flux F_a and ocean heat flux F_o are major sources of energy intake into the ice-ocean layer, their values and properties are still open for debate. The sea-ice albedo α_I is a critical parameter that enters into the solar shortwave radiative drive; observations reveal that α_I varies drastically depending on the type of ice. In addition the total initial energy and its distribution over the ice-ocean layer determine the system dynamics; diffusivities, longwave radiative drive, and albedo depend nonlinearly on the energy content of a cell.

2.5 Model Results

This model is explored for an ice-ocean layer with various vertical initial energy profiles and a spatially homogeneous energy distribution in the horizontal direction. The spatiotemporal drive of the ice-ocean layer is varied through parameter changes in the ice albedo α_I, the lateral atmospheric heat flux F_a and the ocean heat flux F_o. A cell (i,j) is considered frozen if its energy content is $E_{i,j} < E_m + L/2$, which corresponds to a phase factor of $\Phi < 0.5$ [Fig. 2.1]; otherwise the cell is considered to be in its liquid state.

2.5.1 Bistable System: An Example

All our simulations show that the model exhibits two qualitatively different asymptotic stable steady states in the parameter regime of interest. The open water state (OW) refers to an ice-ocean layer (model domain) that is entirely in the liquid phase throughout the year, and the ice-covered state (IC) refers to an ice-ocean layer with perennial ice. In the IC state the model domain is mainly in the solid phase with a liquid layer at the bottom due

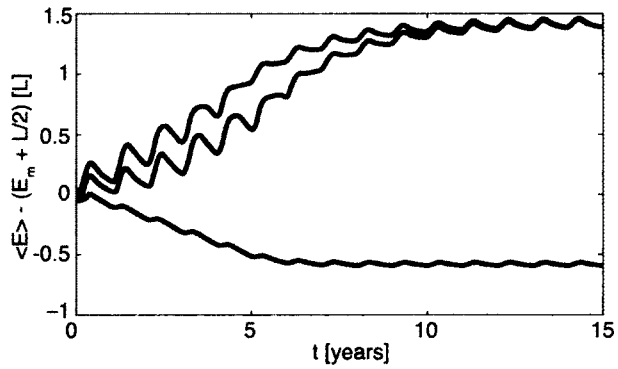

Figure 2.7. Average cell energy $\langle E \rangle$ of the ice/ocean layer ($N = 16$, $M = 100$) as a function of time t for three slightly different initial energies. The initial condition for the bottom graph is a thin ice layer with $E_{1,j} = E_m$, $E_{2,j} = E_m + \frac{L}{3}$, $E_{i>2,j} = E_m + 0.55L$. For the middle graph these initial energies were increased by 1%, and for the top graph by 5%. All other parameters where fixed to $\alpha_I = 0.7$, $F_a = 185.25$ Wm^{-2}, and $F_o = 0.1$ Wm^{-2} besides the standard parameters[4] in this paper.

to the ocean heat influx. Seasonal ice cover exists in this model as a transient phenomenon.

A qualitative argument for the existence of two stable states follows from the shape of the longwave radiative flux balance density R_{LW} in Fig. 2.3b. If the energy of a frozen surface cell decreases, its longwave radiative losses R_{LW} decrease as well; in a stable ice-covered state this energy loss is balanced by the positive shortwave radiation flux density R_{SW} and the positive constant lateral atmospheric heat flux density F_a. On the other side if the energy of a sufficiently warm liquid cell increases, the longwave radiative losses increase also; in a stable OW state this energy loss is balanced by the positive solar shortwave radiation and F_a.

A representative example for the evolution of an ice-ocean layer that is initially covered with a thin layer of ice is shown in Fig. 2.7 for slightly different initial energies and a fixed, typical spatiotemporal atmospheric and oceanic drive. The average cell energy, $\langle E \rangle = \frac{1}{NM} \sum_{i,j=1}^{N,M} E_{i,j}$, decreases to reach the asymptotic state of perennial ice cover. An increase of the initial energy of each cell by 1% and 5% respectively yields the asymptotic state of open water. The large annual oscillations during the transient phase to the OW state are due to the ice-albedo feedback; as the initially thin layer of surface ice melts the surface albedo α decreases and the absorption of shortwave radiation increases to facilitate further melting

of sea-ice during the Arctic summer [Eq. (2.9)]. These oscillations become weaker closer to the asymptotic state as the annual albedo changes are small in the absence of a seasonal ice-cover.

Changes in the distribution of initial cell energies (with a fixed total initial energy) can also alter the asymptotic state from IC to OW. For example, randomly reshuffling the initial cell energies allows for water cells at the top surface of the ice-ocean layer, which have a clearly reduced albedo and thus a clearly increased absorption of short wave radiation to facilitate the open water asymptotic state. These preliminary results indicate that the introduction of spatial inhomogeneities in the ice albedo will influence the transient and asymptotic dynamics of an ice-ocean layer, not discussed within this paper.

2.5.2 Separatrix between Open Water and Ice-Covered Asymptotic State

The bistable system is studied in a 2-dimensional parameter space spanned by the ice albedo α_I and the lateral atmospheric heat flux F_a. Both of these parameters are critical for an understanding of Arctic sea ice and crucial to further studies on sea ice with spatial inhomogeneities due to different types of ice or snow cover. Figure 2.8 points to a linear separatrix between the IC and the OW asymptotic state. Due to the increasingly slower convergence of $\langle E \rangle$ closer to the critical parameters, a lower and upper bound for the separatrix is presented.

The linear separatrix within the "F_a vs α_I" parameter space indicates that the location of the critical IC states (states close to the transition between IC and OW) is only weakly, if at all, coupled to the longwave radiative drive component R_{LW}. The argumentation is as follows: If the system is in a critical IC state, then a fixed increase in the ice-albedo, $\Delta\alpha_I$ corresponds to a unique increase ΔF_a for the system to be in another critical IC state (everywhere along the separatrix curve), since $\frac{\Delta F_a}{\Delta \alpha_I}$ is constant. Since R_{SW} depends linearly on α and $\alpha \approx \alpha_I$ for a frozen cell, it also follows that $\frac{\Delta F_a}{\Delta R_{SW}}$ is constant. This indicates that critical IC states are related to each other via specific changes in solar radiation and in lateral atmospheric drive, at least at this macroscopic level of system description.

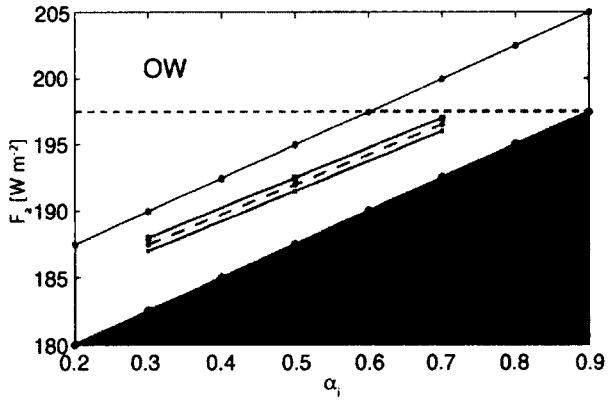

Figure 2.8. Separatrix between the open water (OW) and the ice-covered (IC) asymptotic stable state in the 2-dimensional parameter space spanned by the lateral atmospheric heat flux F_a and the ice albedo α_I. All simulations started with an initially frozen ice-ocean layer with a linear energy profile between $E_{1,j} = E_m - 0.12L$ and $E_{16,j} = E_m - 0.09L$. The parameter resolution is $\Delta\alpha_I = 0.1$ and $\Delta F_a = 0.5 Wm^{-2}$. Simulations within the white (dark gray) triangle, including its boundaries, converge to the OW (IC) stable state within 27 years of real time, whereas simulations within the light gray area have not converged during that time. Symbols denote actual data points. The two solid lines within the light gray area mark simulations which have converged after 41 years of real time to the IC state (lower line) or to the OW state (upper line). The dashed line further narrows down the location of the separatrix; simulations below (on and above) the dashed line have not converged but show a negative (positive) rate of change of average cell energy $\langle E \rangle$ from the second to last to the last annual cycle and are expected to eventually reach the IC (OW) state. The parameters are $F_o = 2$ Wm^{-2} and the standard parameters[4] . The horizontal line marks the parameters explored in Fig. 2.9.

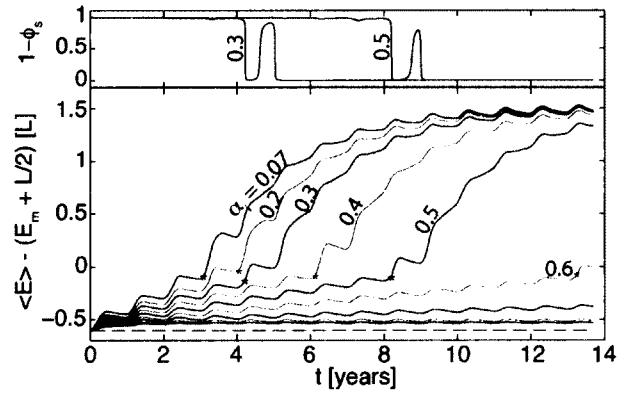

Figure 2.9. Time evolution of the average cell energy. Lower figure: Time evolution of the average cell energy $\langle E \rangle$ of an initially frozen ice-ocean layer for varying ice albedos α_I along the horizontal line in Fig. 2.8 at $F_a = 197.5 Wm^{-2}$. From top to bottom the graphs correspond to $\alpha_I = 0.07$ (black, thick line), 0.2 (grey), 0.3 (black), 0.4 (grey, thick line), 0.5 (black), 0.6 (grey), 0.7 (black), 0.8 (grey) and 0.9 (black). All simulations for $\alpha_I \leq 0.7$ reach the OW asymptotic state, while simulations with $\alpha_I = 0.8$ and 0.9 approach their respective IC asymptotic states [cf. Fig. 2.8]. The symbol "$\star$" on each graph marks the loss of perennial sea ice. The dashed horizontal line denotes the initial average cell energy. The upper figure shows the surface phase factor $\Phi_S = \Phi(E_{1,j})$ of the top row in the ice-ocean layer for simulations with $\alpha_I = 0.3$ and $\alpha_I = 0.5$. The convergence behavior to the OW states is not plotted in the panels to better resolve the transition dynamics.

2.5.3 Characteristics of the Ice-Ocean Layer for Varying Ice Albedos

The albedo of sea ice is not a constant. It can vary significantly due to numerous effects such as conditions of ice formation, age of ice, and snow cover. While the current model neglects changes of ice albedo over time, a basic understanding of the effect of lowering or raising the ice albedo is needed to gain insight into the robustness of transient and asymptotic dynamics.

Figure 2.9 shows the evolution of the average cell energy $\langle E \rangle$ of an initially frozen ice-ocean layer for varying ice albedos α_I. Lower ice albedos cause an earlier warming due to higher uptake of solar shortwave radiation during ice covered surface conditions. High ice albedos ($\alpha_I = 0.8$ and 0.9 in Fig. 2.9) cause comparatively small absorption of solar radiation; the system stays in a state of perennial ice cover and asymptotically reaches the IC state. The simulation with $\alpha_I = \alpha_W = 0.07$ is a control run for the absence of albedo feedback. In this case, the absorption of solar radiation does not differ between ice and water, but energy-dependent physical material properties (D) change due to the phase transition, and longwave radiative drive R_{LW} varies with the surface energy (temperature).

The warming of the ice-ocean layer can be broken down into three regimes: (i) Slow warming under ice covered conditions (until time marked by symbol "$\star$"), (ii) rapid warming after surface ice melt (e.g., from 2 to about 6 years in case of $\alpha_I = 0.07$), and (iii) slow approach of asymptotically stable OW state. For comparison, the times for perennial ice cover, seasonal ice cover, and open water are presented by the phase factor $\Phi(E_{1,j})$ of the top row of the ice-ocean layer, and plotted in the upper part of Fig. 2.9 for two different ice albedos.

During perennial ice-cover [phase (i)] the average cell energy $\langle E \rangle$ increases gradually (linearly) with time for all α_I with transition to the OW state. A comparatively larger ice albedo corresponds to a smaller rate of energy change and longer times to reach the first surface ice melt. Superimposed to this linear energy increase are smaller amplitude oscillations that originate from the absorption of solar radiation during the Arctic summer and from the absence of solar radiation during the Arctic winter. At the times marked by symbol "$\star$", surface ice starts to melt which induces a change in warming behavior (phase ii). A short period of seasonal ice is followed by perennial open water. During seasonal ice cover the average energy increases sharply, starting with a kink in the graphs that indicate

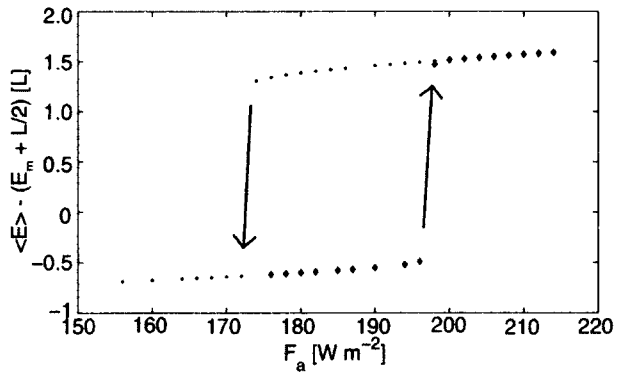

Figure 2.10. Hysteresis of the average cell energy $\langle E \rangle$ as a response to varying atmospheric lateral heat flux F_a. Simulations with an initially ice-covered state (diamonds) started with a linear energy profile between the top row $E_{1,j} = E_m - 0.07L$ and the bottom row $E_{16,j} = E_m - 0.04L$, i.e. the entire ice-ocean layer is initially frozen with a surface albedo of $\alpha(t = 0) = 0.7$. Simulations with an initially open water state (dots) were initiated with a linear energy profile ranging from $E_{1,j} = E_m + 2.4L$ at the surface to $E_{16,j} = E_m + 2.7L$ at the bottom; the initial surface albedo is $\alpha(t = 0) = 0.07$. Each data point corresponds to the asymptotic state reached by a single simulation. The arrows mark the jump in the hysteresis curve. The system parameters are $\alpha_I = 0.7$ and $F_o = 2Wm^{-2}$ besides the standard parameters[4] in this paper.

the onset of the albedo feedback. Melting of ice causes higher uptake of solar radiation to amplify the melting of ice. Once perennial water conditions are reached under the rapid warming regime (phase ii), the reduced longwave radiative energy loss in the range $E - (E_m + L/2) \in [0.6L, 1.3L]$ [Fig. 2.3b] is the significant driver for the rapid warming. All the simulations approaching the OW state are now governed by the same physical parameters as no ice is left, and the differences in ice-albedo are only manifested in slightly different energies at the beginning of perennial open water. All of these simulations converge to the same OW state but with different transient time (phase iii), much in analogy to the case discussed in Fig. 2.7.

2.5.4 Hysteresis in the "Future" of Arctic Model Sea Ice

An important question concerning sea ice retreat in the Arctic is under which conditions a perennially ice-free ocean (OW stable state) would return to being perennially ice covered. We therefore study the response of Arctic sea ice $\langle E \rangle$ to varying inputs of lateral atmo-

spheric heat flux F_a. Starting with an initially ice-covered state (diamonds in Fig. 2.10), the system reaches the IC stable asymptotic state for atmospheric lateral heat fluxes below a critical value of $F_a \approx 198 Wm^{-2}$. Once F_a exceeds the critical value, the system transitions to the OW stable asymptotic state. These findings can be understood as the initial albedo is that of ice, $\alpha(t = 0) = \alpha_I = 0.7$, which strongly limits the energy up-take due to solar radiation R_{SW} [Fig. 2.5], unless F_a reaches a level high enough to induce surface melting. The albedo of water is $\alpha_W = 0.07$, and the now enhanced absorption of solar radiation causes a transition to the OW stable state. Once the OW stable state is reached F_a has to be reduced significantly, to approximately $174 Wm^{-2}$, to return the model domain back to the IC stable state. This is due to the reverse effect as the initially open water state absorbs comparatively large amounts of shortwave radiation, which keeps the model domain perennially unfrozen. If F_a is reduced to the point that the total heat loss in the winter months, due to the negative longwave energy budget R_{LW} [Fig. 2.3b], induces freezing of the surface cells, then the surface albedo increases to reduce the shortwave energy uptake. For each of the asymptotic states a linear relation between $\langle E \rangle$ and F_a is revealed in Fig. 2.10.

The lack of reversibility between stable asymptotic states under changing system input is a typical phenomenon in bistable systems. For a given lateral atmospheric heat flux F_a within the parameter regime of coexistence of the two stable states, the asymptotic state cannot be predicted without information about the history of the system. Re-establishing the Arctic sea ice after it is gone requires a drastic reduction of lateral atmospheric heat flux.

2.5.5 Ocean Heat Flux versus Lateral Atmospheric Heat Flux

An ice-ocean layer whose surface is initially homogeneously covered with ice experiences a constant sum of ocean heat flux and lateral atmospheric heat flux, $F_a + F_o = 185.25 Wm^{-2}$, while their ratio is varied. Figure 2.11 shows that the system asymptotically reaches the OW state for ocean heat fluxes above a critical value; otherwise it asymptotically reaches the IC state. The time it takes the system to converge to the stable state increases drastically for ocean heat fluxes close to the critical value. This figure also indicates clearly that ocean heat flux is more efficient than atmospheric heat flux to melt Arctic sea ice; only small portions of heat entering from the bottom already induce transitions to the OW state. This is

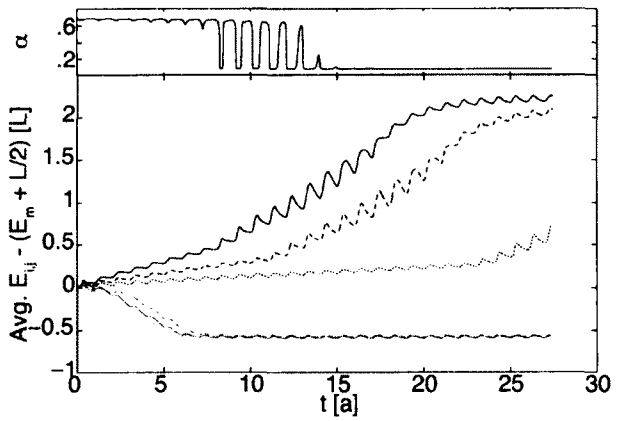

Figure 2.11. Temporal variation of the average cell energy. Lower panel: Temporal variation of the average cell energy $\langle E \rangle$ for an initially ice-covered ice-ocean layer close to the phase transition. The sum of lateral atmospheric heat flux F_A and ocean heat flux F_o is kept constant, $F_a + F_o = 185.25$ W m^{-2}; their ratio is varied with the ocean heat flux decreasing from top to bottom, $F_o = 20$ W m^{-2}, $F_o = 17$ W m^{-2}, $F_o = 15$ W m^{-2}, $F_o = 10$ W m^{-2}, $F_o = 7$ W m^{-2}, and $F_o = 5$ W m^{-2}. The upper three curves asymptotically approach their respective OW state, whereas the lower curves approach their IC state. Initial condition and all other system parameters are the same as in Fig. 2.7. The top panel shows the time evolution of the albedo α for the simulation in the lower panel with $F_o = 20$ W m^{-2}. The convergence behavior to the OW states is not plotted in the panels to better resolve the transition dynamics.

understandable as heat F_o entering at the bottom of the ice-ocean layer cannot escape it immediately, but has to diffuse to the upper surface, which is the only location where heat loss occurs. In contrast, at least parts of F_a can escape the model domain immediately as longwave radiative loss R_{LW}. The findings in Fig. 2.11 tell that ocean heat fluxes should not be underestimated regarding its consequences for Arctic sea ice melting. They are consistent with recent observations in the Canada Basin(Shimada et al., 2006), where patterns of ice reduction in the Arctic Ocean correlated well with the inflow of warm Pacific summer water.

The time-evolution of those simulations transitioning towards the OW stable state is governed by three regimes, a slow increase of energy during perennial ice cover, a strong increase in energy during a transient phase with seasonal ice during the winter months, and a slow convergence towards the respective asymptotic OW state. This follows from the time variation of $\langle E \rangle$ for $F_o = 20 Wm^{-2}$ (bottom panel, Fig. 2.11) in comparison to the time variation of the surface albedo α (top panel, Fig. 2.11), a direct indicator of ice cover. The onset of the strong increase in $\langle E \rangle$ at $t \approx 7$ years, coincides with the first ice free summer during which the surface albedo is only $\alpha_W = 0.07$, and thus clearly indicates an albedo feedback effect. The seasonal oscillations in $\langle E \rangle$ are amplified during this transient phase, and decrease again - somewhat delayed - after the start of perennial open water. The reduced longwave radiative energy loss in the range $E - (E_m + L/2) \in [0.6L, 1.3L]$ [Fig. 2.3b] additionally drives the strong energy uptake in this phase. With further increasing (surface) cell energy the longwave radiative energy loss continues to grow until it is balanced by the incoming shortwave solar radiation; the system converges to its respective OW state.

2.6 Conclusion

Between global circulation (climate) models and one-dimensional models of climate subsystems exits a knowledge gap. While the global climate models describe large-scale interactions between oceans, landmasses and atmosphere reasonably well, their high degree of parameterization and their large number of variables make it difficult to isolate and understand single climate processes such as the ice albedo feedback (Bony et al., 2006). On the other hand, one-dimensional sea-ice models (Thorndike, 1992; Eisenman and Wet-

tlaufer, 2009) provide theoretical insight into subsystems of climate; they are computationally cheap, but make it difficult to model spatial inhomogeneities such as heterogeneous ice albedo. Network (lattice) models may serve as an interface between these two model classes, opening a pathway to study isolated processes of spatially extended and possibly inhomogeneous climate sub-systems; they are computationally cheap enough to allow for detailed parameter variations.

We have introduced a two-dimensional energy-based lattice model with nonlinear diffusive coupling to investigate thermodynamic feedback processes in an Arctic ice-ocean layer. The state and phase of a lattice node is determined from the energy content of an ice-ocean cell. The interaction of the ice-ocean layer with the atmosphere is modeled as a spatiotemporal drive including shortwave solar radiation, longwave radiation budget and a lateral atmospheric heat flux that accounts for heat influxes from lower latitudes. Solar shortwave radiation includes diurnal and seasonal variations, and it is mitigated through an optical thickness parameterization of the atmosphere; cloud cover is not implemented to reduce the number of possible feedbacks. The longwave radiation budget between surface and atmosphere is based on Stefan Boltzmann's equation with a grey body emissivity for the surface and a parameterized temperature dependent emissivity of an air-water mixture for the atmosphere. The interaction of the ice-ocean layer with the deep ocean is modeled by the ocean heat flux parameter.

The network structure of the model is designed to introduce spatial and temporal inhomogeneities in the ice-ocean layer as well as in the atmospheric and oceanic drive. Before that however, the model dynamics needs to be understood in more simple situations. This paper also presents first results for a horizontally spatially homogeneous Arctic and time-independent model parameters; the results are promising insofar as they are consistent with results reported for one-dimensional analytical models (Thorndike, 1992; Eisenman and Wettlaufer, 2009).

The system is bistable. One asymptotic stable state refers to an ice-ocean layer that is perennially open water, and the other asymptotic stable state refers to an ice-ocean layer that is perennially ice covered. Seasonal ice cover only appears as a transient state. These results are in analogy to one-dimensional thermodynamics sea-ice models (Thorndike, 1992; Eisenman and Wettlaufer, 2009) that implement a rather involved approach to modeling

an atmosphere above the ice-ocean layer. As it is typical for bistable systems there exists a lack of reversibility (hysteresis) between these two stable states when varying the input, i.e. the lateral atmospheric heat flux. The implication is that once an ice covered ocean looses its perennial ice cover, significant cooling has to take place for an ice cover to re-establish.

We also find that ocean heat fluxes are more efficient than atmospheric heat fluxes to melt Arctic sea ice; only small portions of heat entering from the bottom of the ice-ocean layer induce already a transition to the stable asymptotic state with perennial open water. This indicates that ocean currents, understood as heat conveyors, can play a significant role in melting continuous ice covers. Recent observations in the Canada Basin(Shimada et al., 2006) show that patterns of ice reduction in the Arctic Ocean correlated well with the inflow of warm Pacific summer water. In future studies spatial and temporal variations of ocean heat fluxes, and the timing of warm water inflow may have a strong impact on year to year variations of Arctic sea ice cover and its transition to perennial open water.

The real strength of the network structure of the model lies in the fact that surface heterogeneities can be easily implemented. This is especially interesting on a small scale ($\approx 100m$) to study the effect of ice albedo variations, a natural effect due to ice formation in moving water (pancake ice) and the processes of aging ice and wind-blown snow cover. Preliminary results suggest that slight heterogeneities can have a significant effect on transient behavior. On a large scale (100 km) surface heterogeneities are relevant to study the effect of seasonal progression in the North-South direction. We expect interesting pattern formation phenomena in Arctic model sea ice when introducing various types of inhomogeneities and gradients in future studies.

Acknowledgments

This research is supported by a 2009 Global Change Student Research Grant sponsored by the Cooperative Institute for Alaska Research (CIFAR), and by a UAF graduate fellowship.

References

Barry, R, M Serreze, J Maslanik, and R Preller (1993). "The Arctic Sea Ice-Climate System: Observations and Modelling". In: *Reviews of Geophysics* 31.4, pp. 397–422.

Bitz, C and G Roe (2004). "A Mechanism for the High Rate of Sea Ice Thinning in the Arctic Ocean". In: *Journal of Climate* 17.18, pp. 3623–3632.

Björk, G and J Sönderkvist (2002). "Dependence of the Arctic Ocean ice thickness distribution on the poleward energy flux in the atmosphere". In: *Journal of Geophysical Research* 107.C10.

Bony, S, R Colman, V Kattsov, R Allan, C Bretherton, J Dufresne, A Hall, S Hallegate, M Holland, W Ingram, D Randall, B Soden, G Tselioudis, and M Webb (Aug. 2006). "How well do we understand and evaluate climate change feedback processes?" In: *Journal of Climate* 19, pp. 3445–3482.

Campbell and J Norman (1998). *Introduction to environmental biophysics*. Second. New York, NY: Springer Science+Business Media.

Carslaw, H and J Jaeger (1959). *Conduction of Heat in Solids*. 2nd. Oxford: Oxford Science Publications.

Cross, M and P Hohenberg (1993). "Pattern formation outside of equilibrium". In: *Reviews of Modern Physics* 65, pp. 851–1112. DOI: doi:10.1103/RevModPhys.65.851.

Curry, J, J Schramm, and E Ebert (1995). "Sea ice-albedo climate feedback mechanism". In: *Journal of Climate* 8, pp. 240–247.

DeWeaver, E, E Hunke, and M Holland (May 2008). "Comment on"On the reliability of simulated Arctic sea ice in global climate models"by I. Eisenman, N. Untersteiner, and JS Wettlaufer". In: *Geophysical Research Letters* 35.4, p. 4501.

Eicken, H (2003). "From the microscopic to the macroscopic to the regional scale: Growth, microstructure and properties of sea ice". In: *Sea Ice: An Introduction to physics, chemistry, biology and geology*. Ed. by D. N. Thomas and G. S. Dieckmann. Blackwell Science Ltd., pp. 22–81.

Eisenman, I, N Untersteiner, and J Wettlaufer (May 2007). "On the reliability of simulated Arctic sea ice in global climate models". In: *Geophysical Research Letters* 34.10, pp. 1–4.

Eisenman, I., N. Untersteiner, and J Wettlaufer (May 2008). "Reply to comment by ET DeWeaver et al. on" On the reliability of simulated Arctic sea ice in global climate models"". In: *Geophysical Research Letters* 35.4, pp. 1–4. DOI: 10.1029/2007GL032173.

Eisenman, I and J Wettlaufer (Jan. 2009). "Nonlinear threshold behavior during the loss of Arctic sea ice". In: *PNAS* 106.1, pp. 28–32.

Goff, J (1957). "Saturation pressure of water on the new Kelvin temperature scale". In: *Transactions of the American society of heating and ventilating engineers*, pp. 347–354.

Golden, K (2001). "Brine percolation and the transport properties of sea ice". In: *Annals of Glaciology, Vol 33*. ANNALS OF GLACIOLOGY 33, pp. 28–36.

Golden, K, S Ackley, and V Lytle (Dec. 1998). "The percolation phase transition in sea ice". In: *Science* 282.5397, pp. 2238–2241.

Maykut, G and N Untersteiner (1971). "Some results from a time-dependent thermodynamic model of sea-ice". In: *Journal of Geophysical Research* 76, pp. 1550–1575.

National Oceanic and Atmospheric Administration (NOAA) (2009). *Arctic Change - Ice - Sea Ice*. URL: `http://www.arctic.noaa.gov/detect/ice-seaice.shtml`.

Parkinson, C, K Vinnikov, and D Cavalieri (2006). "Evalutation of the simulation of the annual cycle of Arctic and Antarctic sea ice coverages by 11 major global climate models". In: *Journal of Climate* 17, p. 3623.

Pecora, L and P Hohenberg (1998). "Master stability functions of synchronized coupled systems". In: *Physical Review Letters* 80, p. 2109.

Peixoto, J and A Oort (1992). *Physics of Climate*. Woodbury, NY, USA: AIP Press.

Rothrock, D, Y Yu, and G Maykut (1999). "Thinning of the Arctic Sea-Ice Cover". In: *Geophysical Research Letters* 26.23, pp. 3469–3472.

Serreze, M, A Barrett, A Slater, M Steele, J Zhang, and K Trenberth (2007). "The large-scale energy budget of the Arctic". In: *Journal of Geophysical Research* 112.

Shimada, K, T Kamoshida, M Itoh, S Nishino, E Carmack, F McLaughlin, S Zimmermann, and A Proshutinsky (2006). "Pacific Ocean inflow: Influence on catastrophic reduction of sea ice cover in the Arctic Ocean". In: *Geophysical Research Letters* 33.

Siegel, R and J Howell (1992). *Thermal Radiation Heat Transfer*. 3rd. Washington: Hemisphere Publishing Corporation.

Stroeve, J, M Serreze, F Fetterer, T Arbeter, W Meier, J Maslanik, and K Knowles (2005). "Tracking the Arctics shrinking ice cover: Another extreme September minimum in 2004". In: *Geophysical Research Letters* 32, p. L04501.

Thomas, D and G Dieckmann (2003). *Sea Ice: An Introduction to physics, chemistry, biology and geology*. Malden, MA 02148-5020, USA: Blackwell Science Ltd.

Thorndike, A (June 1992). "A toy model linking atmospheric and thermal radiation and sea ice growth". In: *Journal of Geophysical Research* 97.C6, pp. 9401–9410.

Untersteiner, N (1964). "Calculations of temperature regime and heat budget of sea ice in the central Arctic". In: *Journal of Geophysical Research* 69, p. 4755.

Walker, G (2006). "The tipping point of the iceberg". In: *Nature* 441, p. 802.

Weeks, W and B Hibler (2010). *On Sea Ice*. University of Alaska Press.

Chapter 3

Albedo Parametrization and Reversibility of Sea Ice Decay[1]

3.1 Abstract

The Arctic's sea ice cover has been receding rapidly in recent years, and global climate models typically predict a further decline over the next century. It is an open question whether a possible loss of Arctic sea ice is reversible. We study the stability of Arctic model sea ice in a conceptual, two-dimensional energy-based regular network model of the ice-ocean layer that considers ARM's longwave radiative budget data and SHEBA albedo measurements. Seasonal ice cover, perennial ice and perennial open water are asymptotic states accessible by the model. We show that the shape of albedo parameterization near the melting temperature differentiates between reversible continuous sea ice decrease under atmospheric forcing and hysteresis behavior. Fixed points induced solely by the surface energy budget are essential for understanding the interaction of surface energy with the radiative forcing and the underlying body of ice/water, particularly close to a bifurcation point. Future studies will explore ice edge stability and reversibility in this lattice model, generalized to a latitudinal transect with spatiotemporal lateral atmospheric heat transfer and high spatial resolution.

3.2 Introduction

The future state of the Arctic's sea ice cover is subject to a multi-faceted discussion in the literature. Results of general circulation models (GCMs) are scrutinized regarding the ice extent under various forcing scenarios [Fourth Assessment Report of the Intergovernmental Panel on Climate Change (IPCC, 2007)]. Single column models [ODE, by e.g., Maykut and Untersteiner, 1971, Thorndike, 1992, Eisenman and Wettlaufer, 2009, Notz, 2009, Müller-Stoffels and Wackerbauer, 2011] and energy balance models [EBM, by e.g., Sellers, 1969, North, 1984] are used to discuss the stability of Arctic sea ice in terms of few interacting climate components. While GCMs contain the most detail of physical features found in the climate system and describe large-scale interactions between oceans, landmasses and atmosphere reasonably well, their complexity and high-dimensional parameter space

[1] This chapter is published as: Müller-Stoffels, M and R Wackerbauer, *Albedo parametrization and reversibility of sea ice decay*, Nonlinear Processes in Geophysics **19**, 81-94, 2012.

require hierarchical modeling in order to understand complex climate processes and feedbacks (Bony et al., 2006).

Arctic sea ice has a relatively high albedo in the visible shortwave spectrum, while open water has a low albedo. When sea ice melts, the surface turns from a very good reflector of sunlight to a very good absorber; more open ocean absorbs more solar energy to melt more ice. This ice albedo feedback is one of several known major feedbacks of similar magnitude in the Arctic (Bony et al., 2006) and its understanding is crucial to the understanding of the stability of sea ice.

A variety of albedo parameterizations are used in the literature, ranging from steplike to more gradual albedo changes around the melting point. Albedo parameterizations in GCMs can depend on snow depth, ice thickness, and the frequency band of shortwave radiation, and typically exhibit a sharp step in some neighborhood of the phase transition (e.g., Bony et al., 2006; Eisenman, Untersteiner, and Wettlaufer, 2007; DeWeaver, Hunke, and Holland, 2008; Shine and Henderson-Sellers, 1985; Winton, 2008; Liu, Zhang, and Horton, 2007). Small tuning of the ice albedo value severely changes the outcome of GCM's ice extent predictions (Eisenman, Untersteiner, and Wettlaufer, 2007). The IPCC, 2007 reports large intra- and inter-model differences in ice extent and ice volume for the coming century, but these GCMs do not only differ by the albedo parameterization. In EBM models the form of the albedo parametrization influences the existence of a small ice cap instability (North, 1984). In ODE models the loss of Arctic sea ice is found to be reversible or nonreversible (Thorndike, 1992; Eisenman and Wettlaufer, 2009; Notz, 2009; Müller-Stoffels and Wackerbauer, 2011).

ODE-type ice albedo feedback models differ in forcing components and albedo parameterization, and are realized in energy (Müller-Stoffels and Wackerbauer, 2011), enthalpy (Eisenman and Wettlaufer, 2009), or temperature space (Thorndike, 1992; Notz, 2009). Parameterizations for longwave radiative balances are similar among models insofar as radiative surface heat loss increases with temperature; they are assumed to be seasonally dependent (e.g., Thorndike, 1992; Eisenman and Wettlaufer, 2009) or only dependent on temperature (e.g., Notz, 2009; Müller-Stoffels and Wackerbauer, 2011). Shortwave forcing was modeled as constant (Notz, 2009), binary on-off (Thorndike, 1992), monthly (Eisenman and Wettlaufer, 2009) and hourly (Müller-Stoffels and Wackerbauer, 2011) surface heat in-

flux. These differences in shortwave forcing did not result in qualitatively different model dynamics and hysteresis behavior for the model used in this paper. Thus, we hypothesize that the albedo parametrization is key to the model's outcome regarding stability and reversibility of Arctic sea ice, since albedo parameterizations differ across models, including smooth (Müller-Stoffels and Wackerbauer, 2011) and sharp (Thorndike, 1992) step-like albedo behavior around the melting point and wide linear albedo parameterizations (Notz, 2009). In Section 3.3 we briefly describe the regular network model for the ice albedo feedback (Müller-Stoffels and Wackerbauer, 2011), adjusted for ARM's longwave radiative budget data (Barrow, AK) and compared with albedo data from the SHEBA experiment. In Section 3.4 we discuss the relevance of fixed points induced by the annual average surface energy budget and the instantaneous surface energy budget for identifying bistability in parameter space as well as for understanding the system dynamics close to bifurcation points. The effect of albedo parameterization on the robustness of hysteresis is explored in Sect. 3.5.

3.3 Model and Albedo Parameterization

In the following we briefly describe the regular network model by Müller-Stoffels and Wackerbauer, 2011 for an Arctic sea ice-ocean layer under atmospheric and oceanic forcing. Lattice (regular network) models are commonly used to describe nonlinear spatiotemporal dynamics (Cross and Hohenberg, 1993; Stahlke and Wackerbauer, 2009). We review several albedo parameterizations from the literature that are used in conceptual models. The choice of parameterizations for longwave-radiative flux density and for albedo is motivated from observational data.

3.3.1 Model

A thin vertical ice-ocean layer is modeled by a two-dimensional regular network of diffusively interacting ice-ocean cells (Müller-Stoffels and Wackerbauer, 2011). A conceptual picture of the model domain is given in Fig. 3.1. The state of each cell (i,j) is given by its energy content $E_{i,j}$, which also governs the liquid-solid phase transition. The model equation

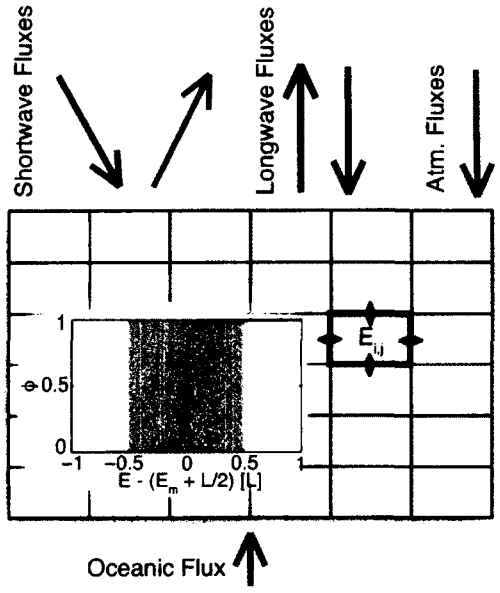

Figure 3.1. The thin vertical ice-ocean layer is modeled by a regular network of diffusively interacting ice-ocean cells. The state of each cell is given by its energy content $E_{i,j}$, which also defines the phase of the cell (ice, water). Each cell can exchange energy with its nearest neighbors via state-dependent nonlinear diffusion. Atmospheric heat fluxes are entering at the upper surface (top row), and oceanic heat fluxes are entering at the bottom row of the ice-ocean layer. The inset shows the steplike phase transition between ice ($\Phi = 0$) and water ($\Phi = 1$) and the gradual release of latent heat L as the energy of a cell increases (shaded area).

for the total energy (sensible and latent heat) $E_{i,j}^{n+1}$ of cell (i,j) at discrete time $n+1$ is

$$\begin{aligned} E_{i,j}^{n+1} &= E_{i,j}^{n} \\ &+ \zeta \sum_{k=-1}^{1} D_{[i,i+k],j}(E_{i+k,j}^{n} - E_{i,j}^{n}) \\ &+ \zeta \sum_{k=-1}^{1} D_{i,[j,j+k]}(E_{i,j+k}^{n} - E_{i,j}^{n}) \\ &+ \delta_{1i}\zeta h^4(R_{SW} + R_{LW}) + \delta_{Ni}\zeta h^4 F_o. \end{aligned} \tag{3.1}$$

$\zeta = \Delta t/h^2$ is a global coupling constant, that determines the relationship between temporal and spatial resolution, constrained by numerical stability. D is a heterogeneous and

nonlinear diffusion constant (local coupling). The model domain is forced by absorbed solar shortwave radiation R_{SW}, longwave radiative exchange R_{LW} between atmosphere and ice/ocean surface, and an oceanic heat flux density F_o that is assumed to be a constant in this study. The factor h^4 ensures correct dimension with h being the cell size. δ_{ij} represents the Kronecker delta. See also Müller-Stoffels and Wackerbauer, 2011 for model details, and Table 3.1 for the physical and numerical parameters used in this study.

The phase of each cell (i,j) determines its physical properties such as surface albedo or thermal diffusivity. The phase transition is modeled by a local energy-dependent *phase factor* (inset Fig. 3.1),

$$\phi(E_{i,j}) = \frac{1}{\pi}\arctan[c(E_{i,j} - E_m - \frac{L}{2})] + \frac{1}{2}, \tag{3.2}$$

with melting energy E_m and volumetric latent heat L. $E_m = C_I h^3 T_0$ represents the energy content of a cell of ice at temperature $T_0 = 273K$ with C_I the volumetric heat capacity of ice. The sharpness of the phase transition is determined by c. The phase factor ϕ controls the phase dependent parameter X via a switch function according to

$$X = X_I + (X_W - X_I)\phi, \tag{3.3}$$

where the subscripts I and W refer to ice and water respectively. The parameter X represents the surface albedo α, the thermal conductivity k, the volumetric heat capacity C, or the release of latent heat L.

The thermal diffusivity $D_{i,j} = k_{i,j}/C_{i,j}$ for a single cell follows Eq. (3.3). We use the molecular thermal diffusivity of ice or water as given in Table 3.1. Thermal exchange between two adjacent cells is calculated from the respective individual thermal diffusivities $D_{i_1,j}$ and $D_{i_2,j}$ as

$$D_{[i_1,i_2],j} = 2\frac{D_{i_1,j}D_{i_2,j}}{D_{i_1,j} + D_{i_2,j}} \tag{3.4}$$

for two vertically adjacent cells (i_1,j) and (i_2,j). In this study we assume spatial homogeneity in the horizontal direction, which leads to $D_{i,[j_1,j_2]} = D_{i,j}$ with $j = j_1 = j_2$.

The *absorbed solar shortwave radiation* R_{SW} depends on the surface albedo α and the actual downwelling shortwave radiation $R_{SW}^{\downarrow}$ (e.g., Campbell and Norman, 1998; Müller-Stoffels and Wackerbauer, 2011),

$$R_{SW} = (1-\alpha)R_{SW}^{\downarrow} = (1-\alpha)S_{p0}[\tau^m + 0.3(1-\tau^m)]. \tag{3.5}$$

S_{p0} is the shortwave flux density received at the top of the atmosphere on a surface perpendicular to the incoming flux, and depends on the zenith angle. The factor in square brackets describes the transmission losses in the atmosphere for direct (first term) and diffuse (second term) radiation, with τ^m the optical thickness. The absorbed shortwave radiation is both a function of time and local surface properties.

Longwave radiative forcing, R_{LW}: One contribution to R_{LW} is due to the longwave radiative budget between the atmosphere and the surface of the ice-ocean layer according to Stefan-Boltzmann's equation, $(\varepsilon_a - \varepsilon_s)\sigma T^4$, with Stefan-Boltzmann constant σ and temperature T in Kelvin. The emissivity ε_s for the upwelling thermal radiation is rather constant, with $\varepsilon_s = 0.96$ being a good approximation for sea ice's and ocean's surface emissivity (Campbell and Norman, 1998). The atmosphere's emissivity ε_a depends on various parameters such as temperature, water vapor pressure, and gas concentration (e.g., Satterlund, 1979; Prata, 1996; Crawford and Duchon, 1999). Not all parameterizations for ε_a given in the literature remain physical (i.e. $\varepsilon_a < 1$) across reasonable model conditions. After exploring several parameterizations (Satterlund, 1979; Prata, 1996; Crawford and Duchon, 1999), we chose the parameterization by (Satterlund, 1979) in this study, since his parameterization is reported to perform well at low temperatures, remains physical for all temperatures, and depends only on one variable (if one concedes that water vapor pressure is a function of temperature itself). We modified this parameterization such that it cannot exceed ε_s, which renders Satterlund's equation to be

$$\varepsilon_a = \varepsilon_s \left[1 - \exp(-e_0^{T/2016})\right]. \tag{3.6}$$

The vapor pressure e_0 is assumed to be 80% of the saturation vapor pressure, since an average relative humidity of 80% in the Arctic is comparable to annually averaged meteorological data for Barrow, AK (*ARM Data Archive* 2010). The saturation vapor pressure is calculated from the temperature (in Kelvin) using the World Meteorological Organization's recommended parameterization by Goff, 1957. With these assumptions the exponent in Eq. (3.6) can be well approximated as $-e_0^{T/2016} \approx -7.7 \times 10^{-5} T^2 + 0.028T - 3.1$.

The other contribution to the longwave radiative forcing R_{LW} is due to the thermal contact of the Arctic with lower latitudes via ocean and atmospheric heat transfer. This plays an important role, especially during times when temperature gradients between lower

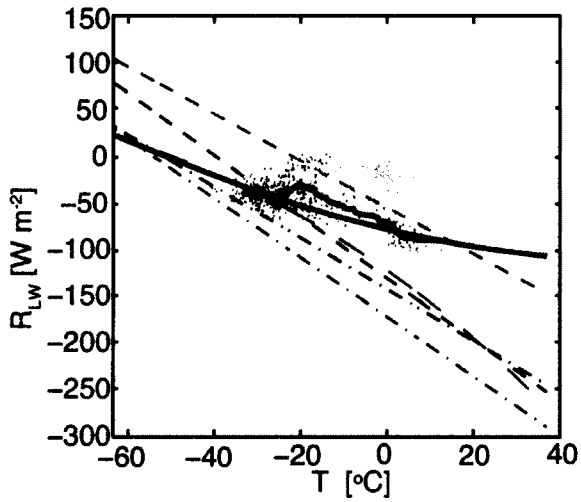

Figure 3.2. Longwave radiative energy budget R_{LW} versus surface temperature T, with negative values signifying a heat loss of the surface to the atmosphere. The light grey dots represent daily averages for the 14 year record of ARM's longwave radiative budget data for Barrow, AK (*ARM Data Archive* 2010) for all sky (cloudy and clear) conditions. The black dots mark the subset of data points for clear sky conditions, assuming that the sky is free of clouds if the skyward pointing IR thermometer reads values below 220K. These scattered clear sky data are filtered with a 50 data point wide moving average (solid blue line). The longwave budget (solid red line) from Eq. (3.7) is fitted to these filtered clear sky data with a higher weight to the regions of higher data density, and yields $a = -1.05$ W m^{-2} K^{-1} and $b = b_0 = 301$ W m^{-2}. Longwave radiative energy budgets used in other conceptual models are plotted for comparison: parameterization by Notz, 2009 (dashed grey line; increased by 100 W m^{-2} to fit the figure); Thorndike, 1992 (dash-dotted lines) differentiates between a summer (red) and winter (blue) parameterization; and Eisenman and Wettlaufer, 2009 (dashed lines) use monthly varying parameterizations that expand between a maximum (August, red) and minimum curve (March, blue). All parameterizations are monotonously decreasing with T, consistent with the clear sky 50 point running average.

latitudes and the Arctic are large. This can cause strong local temperature inversions, especially in the winter, which complicates calculation of a radiation balance via just one (surface) temperature. To account for the actual transfer of sensible heat northward we assume a linear temperature relationship and fit the longwave radiation budget R_{LW} to longwave radiation data provided by ARM for Barrow, AK (*ARM Data Archive* 2010), following

$$R_{LW} = [\varepsilon_a(T) - \varepsilon_s]\sigma T^4 + aT + b, \tag{3.7}$$

with $b = b_0 + \Delta b$. a and b_0 are empirical constants, and Δb is a bifurcation parameter. Figure 3.2 shows the temperature dependence of this longwave radiation budget R_{LW} for $a = -1.05\,\mathrm{W\,m^{-2}\,K^{-1}}$, $b_0 = 301\,\mathrm{W\,m^{-2}}$, and $\Delta b = 0\,\mathrm{W\,m^{-2}}$, and compares it to daily averages for the 14 year record of longwave radiation data for Barrow, AK under all sky and clear sky conditions. For comparison we also show the longwave radiation budgets used by Thorndike, 1992, Eisenman and Wettlaufer, 2009, and Notz, 2009 in their respective conceptual models. Thorndike, 1992 and Eisenman and Wettlaufer, 2009 use an irradiance model for the atmosphere to derive the longwave budget. All parameterizations assume that the LW budget is a monotonously decreasing function of temperature. This is not a trivial assumption and does not simply emerge in Stefan-Boltzmann budgets $(\varepsilon_a - \varepsilon_s)\sigma T^4$ from the parameterizations of ε_a given in the literature (e.g., Satterlund, 1979; Prata, 1996; Crawford and Duchon, 1999), although it is consistent with the data record for Barrow, AK. Both Thorndike, 1992 and Eisenman and Wettlaufer, 2009 include a direct time-dependence into their longwave budget parameterization, based on observations. Interestingly, our parametrization [Eq. (3.7)] and 's August and March parameterization intersect at reasonable seasonal temperatures.

Our system exhibits slightly exaggerated high and low temperature values because several significant dampening factors are not included, as e.g., a connection to a stable temperature reservoir (deep ocean), evaporation effects (cooling due to absorption of latent heat of evaporation), and enhanced heat transfer in the ocean due to eddy thermal diffusivities.

3.3.2 Albedo Parameterization

The (surface) albedo describes the fraction of shortwave radiation reflected by the surface, and refers to a spectrally integrated bulk albedo herein. In the sea ice-ocean system the albedo can range from 0.9 for fresh snow to 0.07 for open ocean (Perovich et al., 2002). Values for ice lie within this interval, with young ice's albedo around 0.7, and melting ice and melt ponds down to 0.4 (Perovich et al., 2002). Albedo measurements at a fixed location do not support a clear temperature dependence, especially as snow or ice albedo display aging effects due to surface freeze-thaw cycles and snow metamorphosis. Daily average albedos along a SHEBA transect, however, do reveal a relatively sharp transition between high values for ice (Perovich, 1998) and low values for open water and leads [Fig. 3.3]. At temperatures below but close to the freezing point the fluctuations in the surface albedo grow as the average albedo decreases. The average albedo for a lead (Paulson, 1998) is much lower than that for ice at the same temperature (Andreas et al., 1998).

In conceptual models different approaches have been taken in parameterizing the albedo (Fig. 3.3). Notz, 2009 follows Sellers, 1969 suggestion of a monotonously decreasing linear function between $-43°C$ and $10°C$, which results in a very gradual transition of the surface albedo over a wide temperature range (ALW, Fig. 3.3). Eisenman and Wettlaufer, 2009 parameterize the albedo as a smooth step-like function with a relatively steep transition around the freezing temperature (AST, Fig. 3.3). Thorndike, 1992 uses a sharp step function with a transition at the freezing point. The albedo parameterization in Eq. (3.3) (Müller-Stoffels and Wackerbauer, 2011) is routinely used in this paper; it follows a smooth step like energy dependence, which appears as a sharp transition in temperature space (ASE, Fig 3.3). Two quadratic parameterizations are introduced as intermediate cases between the step-like and the linear transition. One (AQW) is for the wide temperature band ($-43°C$ to $10°C$) in which Sellers, 1969 varies the albedo linearly, and the other (AQN) describes the same transition on a narrower ($-18°C$ to $0°C$) temperature band (Fig 3.3). All these albedo parameterizations were adjusted to fit the SHEBA data for cold ice ($\alpha_I = 0.85$) and open water ($\alpha_W = 0.07$).

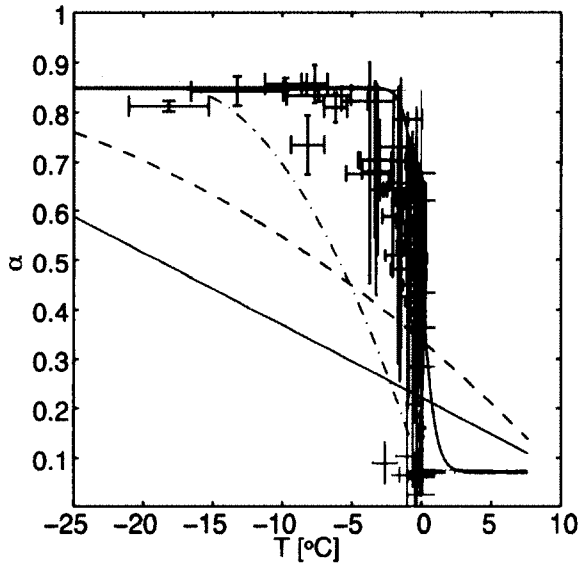

Figure 3.3. Observed and parameterized temperature dependence in surface albedo: The data points correspond to daily average albedo along a transect in the SHEBA experiment versus daily average temperature ['s ice SHEBA data (blue w/ error bars); 's lead SHEBA data (red w/ error bars); and 's temperature SHEBA data]. The albedo parameterizations were adjusted to fit the data for cold ice ($\alpha_I = 0.85$) and open water ($\alpha_W = 0.07$). The parameterizations from conceptual models in the literature include a linear temperature dependence on a wide interval (ALW, grey line) suggested by Sellers, 1969, a smooth step like temperature dependence (AST, purple line) suggested by Eisenman and Wettlaufer, 2009, and a smooth step like energy dependence (Eq. 3.3, ASE, orange line) suggested by Müller-Stoffels and Wackerbauer, 2011. For illustration of intermediate parameterizations a quadratic parameterization over Seller's wide temperature interval ($-43°C \leq T \leq 10°C$, AQW, blue dashed line), and a quadratic parameterization over a narrow temperature interval ($-18°C \leq T \leq 0°C$, AQN, grey dash-dotted line) are introduced.

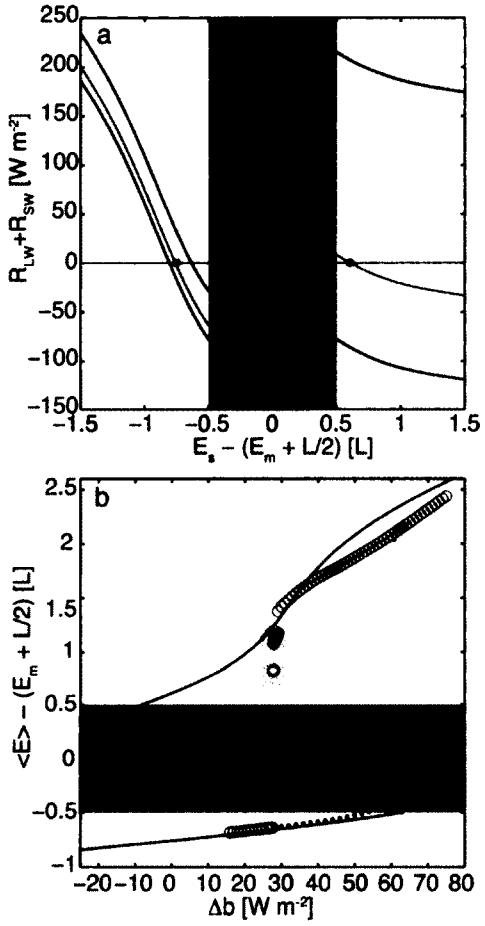

Figure 3.4. a) Surface energy budget $R_{SW} + R_{LW}$ versus surface cell energy for $\Delta b = 0$, $\alpha_I = 0.85$, $\alpha_W = 0.07$, and the albedo parameterization in Eq. (3.3): annual maximum values (upper blue), annual minimum (lower blue), and annual averages (red)]. The zeros of the surface drives are marked by the horizontal line; the symbols indicate the fixed points resulting from the annual average surface drive. b) Hysteresis of the average cell energy $\langle E \rangle$ as a response to varying atmospheric forcing Δb. Simulations with an initially ice covered state (blue dots) started with a uniformly frozen ice-ocean layer [$E - (E_m + L/2) = -0.61L$ for all cells], and simulations with an initially open water state (red circles) started from a uniform water layer [$E - (E_m + L/2) = 0.85L$ for all cells]. The ice cover is seasonal within a narrow range of forcing Δb (shaded blue), if started with an open water initial condition. For comparison, the zeros of the annual average surface energy budget $R_{SW} + R_{LW}$ are plotted as a function of Δb (black graph). In both graphs the energy scale is centered around the phase transition [Eq. (3.2)]. Energies within $-0.5L$ and $0.5L$ (grey area) correspond to the melting point temperature, i.e. they represent the absorption/release of latent heat of that cell.

Table 3.1. Physical constants and system parameters used in all simulations unless stated otherwise.

Symbol	Description	Value
l	Latent heat of fusion	3.35×10^5 J kg^{-1}
ρ_W	Density of water	1000 kg m^{-3}
ρ_I	Density of ice	917 kg m^{-3}
C_W	Heat capacity of water	4.18×10^6 J (m^3 K)$^{-1}$
C_I	Heat capacity of ice	1.93×10^6 J (m^3 K)$^{-1}$
k_W	Thermal conductivity of water	0.6 W (m K)$^{-1}$
k_I	Thermal conductivity of ice	2.2 W (m K)$^{-1}$
α_W	Water albedo (minimum)	0.07
α_I	Ice albedo (maximum)	0.85
τ^m	Optical thickness	0.13
Φ	Latitudinal angle	80° N
F_o	Ocean heat flux	2 W m^{-2}
Δt	Time step	4 h
h	Cell dimension	0.3 m
$\zeta = \frac{\Delta t}{h^2}$	Coupling constant	1.6×10^5 s m^{-2}
N	Number of vertical cells	16
M	Number of horizontal cells	50
c	Sharpness factor	10^{-5}

3.4 System Stability, Dynamics, and Hysteresis

If the ice-ocean system would react to changes in surface forcing instantaneously, the system would precisely follow the instantaneous fixed points resulting from the surface drive. Technically, this would correspond to a (single row) ice ocean layer with atmospheric drive, where the *instantaneous fixed points* are determined from $R_{LW} + R_{SW} = 0$. Since the mass of ice and water can only take on or release a certain amount of heat per time step determined by their thermal diffusivities, the system lags behind these instantaneous fixed points. During Arctic night, i.e. the time in winter when the sun remains below the hori-

zon, the surface energy budget takes its minimum value R_{LW} (Fig. 3.4a), and only one fixed point exists for any Δb. In summer when shortwave radiation dominates the energy budget, one or three instantaneous fixed points exist depending on Δb. For a frozen cell the difference between minimum and maximum surface forcing is given by $(1-\alpha_I)\max(R^{\downarrow}_{SW})$, and for a liquid cell the corresponding difference is $(1-\alpha_W)\max(R^{\downarrow}_{SW})$. The ice albedo feedback is clearly visible as an increase in energy uptake of liquid cells, $E-(E_m+L/2)>0$.

The Arctic Ocean can be assumed to be in a *dynamic equilibrium*. Over the years annual forcing, temperature and ice extent cycles are more or less similar, if we disregard the recently observed trends and the paleoclimate record. Thus, information about system stability and system dynamics can be gleaned from annual averages. Figure 3.4a shows the annual average surface forcing $\langle R_{LW}+R_{SW}\rangle = R_{LW}+[1-\alpha]\langle R^{\downarrow}_{SW}\rangle$ for $\Delta b = 0$ as a function of surface cell energy. If we assume that the ice-ocean layer is driven by this annual average forcing, three fixed points exist: a stable fixed point below the freezing point, an unstable fixed point within the phase transition regime, and a stable fixed point above the freezing point. The bifurcation parameter Δb manipulates the existence and exact location of the fixed points. The height of the step between the average surface forcing on ice and on water (i.e. around $E = E_m + L/2$) is directly related to the albedo difference between ice and water, and can be approximated as $(\alpha_I-\alpha_W)\langle R^{\downarrow}_{SW}\rangle$. In the following we compare the (dynamic) equilibria observed in simulations of Eq. (3.1) with the fixed points resulting from the average surface forcing. By (dynamic) equilibrium we mean that the system's annual cycle reaches its asymptotic value within numerical accuracy.

From the cubic shape of the annual average surface forcing in Fig. 3.4a we expect *hysteresis* of the average cell energy $\langle E\rangle$ as a response to atmospheric forcing Δb. We started simulations in either the open water regime or the ice covered regime and let the system equilibrate under various atmospheric forcings. Figure 3.4b reveals a single stable fixed point corresponding to perennial ice cover for parameters below $\Delta b = 28$ W m $^{-2}$. In a narrow range of forcing between $\Delta b = 28$ and $\Delta b = 30$ W m $^{-2}$, bistability between perennial ice and seasonal ice cover exists. For seasonal ice cover all ice in the system has melted ($E_{ij} > E_m + L/2 \quad \forall \quad i,j$) for at least one day per annual cycle, and the surface row of cells is frozen ($E_{1j} < E_m + L/2 \quad \forall \quad j$) for at least one day. Between $\Delta b = 30$ and $\Delta b = 62$ W m $^{-2}$ bistability between perennial open water and perennial ice exists, while only the perennial

open water state is stable above that forcing regime. Comparing the hysteresis curve with the fixed points from the annual average surface forcing (black line) in Fig. 3.4b reveals that the transition from bistability to a single stable perennial ice state at about $\Delta b = 62$ is well predicted by the annual average surface drive, while the width of the forcing interval for bistability is overestimated.

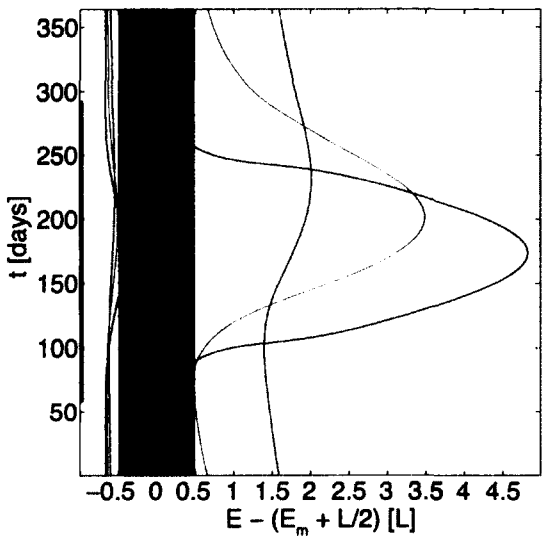

Figure 3.5. Annual cycle of the instantaneous fixed points resulting from the surface energy budget (black curve) together with typical system trajectories for $\Delta b = 40$ Wm^{-2} within the parameter regime of bistability (Fig. 3.4b): Trajectory of average cell energy (dark red) and surface cell energy (light red) for the equilibrated system starting from open water initial conditions; trajectory of average cell energy (dark blue) and surface cell energy (light blue) for the equilibrated system for an initially frozen ice ocean layer. The vertical red line denotes the time of year when the system receives shortwave radiation (Arctic day).

Figure 3.5 shows the existence and location of the instantaneous fixed points (black graph) for a typical atmospheric forcing ($\Delta b = 40$ Wm^{-2}) in the *parameter regime of bistability*. The time of year during which three instantaneous fixed points exist is surprisingly small and confined to spring and fall. For most of the year only a single fixed point exists with a cell energy below the phase transition for the winter months and above the phase transition for the summer months.

The duration of the existence of three instantaneous fixed points is directly tied to the difference in ice albedo α_I and ocean albedo α_W. The larger the ice albedo, the longer into the summer the lower fixed point remains in existence (Fig. 3.4a). Or vice-versa, the larger the ocean albedo the later in the summer the higher fixed point comes to exist. The opposite is the case in the fall. In the extreme case of $\alpha_I = \alpha_W$ the step in the surface forcing around $E = E_m + L/2$ vanishes, and a single fixed point exists that varies with solar radiation. Variation of $\alpha_I - \alpha_W \neq 0$ gives insight into the dependence of bistability on instantaneous fixed points. For various ice albedos $\alpha_I \in \{0.6, 0.7, 0.85, 0.95\}$ and a fixed ocean albedo $\alpha_W = 0.07$ we numerically determine the bifurcation point $\Delta b_\downarrow$ for which simulations starting from open water remain in the high energy state of seasonal ice. The relationship between $\Delta b_\downarrow$ and α_I is linear and follows the numerically determined equation $\Delta b_\downarrow = 34.67\alpha_I - 1.267$, which is consistent with our previous results in Müller-Stoffels and Wackerbauer, 2011. For the respective bifurcation points $\Delta b_\downarrow$ we find that the duration of the existence of the upper stable fixed point is at least 150 days. While this value is likely to be strongly model dependent, the finding points towards a critical minimum existence time of a second stable fixed point for bistability to develop.

Figure 3.5 also shows how typical annual system trajectories are tracking the instantaneous fixed points within the parameter regime of bistability ($\Delta b = 40$ Wm^{-2}). The surface cell energy for the equilibrated system, starting from open water initial conditions (red), decreases during winter but does not reach the stable fixed point for ice cover nor is it sufficiently cooled for the cell to freeze before the onset of Arctic day. During that first part of the year the surface cell is heated from below, indicated by a larger average cell energy than surface cell energy, but the surface energy budget is still sufficiently negative to cool the surface cell. Solar shortwave radiation eventually induces a time interval with three instantaneous fixed points; the surface cell trajectory moves away from the unstable steady state around $E = E_m + L/2$ to approach the instantaneous stable fixed point in the open water energy regime. The surface energy increases rapidly due to the low albedo of open water, but does not truly follow the trajectory of the fixed point due to cooling from below the surface and due to the rapid change of the open water fixed point to higher and higher energy values. The surface cell energy reaches its maximum value slightly after the time of maximum solar radiation since the stable fixed point is still located at higher

energies than the surface cell energy. Cooling from below together with a rapid decline of solar shortwave radiation reduces the surface cell energy to enter the time period of a stable single instantaneous fixed point, located in the frozen regime. The surface cell energy for the equilibrated system for an initially frozen ice ocean layer (blue) is very close to that of the fixed point in the freezing regime. During the part of summer when that fixed point no longer exists, the surface cell energy stays rather unchanged, since R_{SW} is low due to the high ice albedo and since the open water fixed point is far from the melting point and only weakly attractive (low slope of R_{LW} for high energies).

The surface energy dynamics *near the onset and near the ending of the parameter regime of bistability* is considered in more detail, focusing on the seasonal progression of the surface cell energy (Figs. 3.6a-c) and the interaction of surface cell energy with the surface energy budget $R_{LW} + R_{SW}$ (Figs. 3.6d-f). Note that the surface energy budget differs from the rate of change of surface cell energy since energy exchange between surface layer and second layer is not included; Figures 3.6d-f are therefore not phase space representations in the usual sense. We find that the transition from an open ocean to perennial ice is distinctly different than the transition from perennial ice to open ocean.

Figure 3.6a shows consecutive annual cycles of surface cell energy for a simulation with open water initial condition and atmospheric forcing parameter $\Delta b = 27$ W m^{-2} slightly before the onset of bistability (Fig. 3.4b). During the transition from initially open water to perennial ice the surface cell energy and especially its summer maximum diminishes with each new annual cycle. During the winter months when the surface cells enter the freezing regime, a latent heat signal becomes visible in November/December (day 300 to 365) lasting into the early days of the following year. This release of latent heat manifests itself as a local variation (squiggle) of the surface cell energy, where each consecutive squiggle within an annual cycle denotes a further row of cells freezing. The last annual cycle to leave the freezing regime during summer (seasonal ice as a transient state) exhibits fewer squiggles of latent heat release, since the absorbed solar shortwave radiation only resulted in surface melt. The following year even the surface remains frozen throughout the summer; the lack of a sharp increase in surface energy during summer is direct evidence that the albedo remained high. The annual cycle of instantaneous fixed points in Fig. 3.6a (black) consists of a stable fixed point in the frozen water energy regime that exists throughout

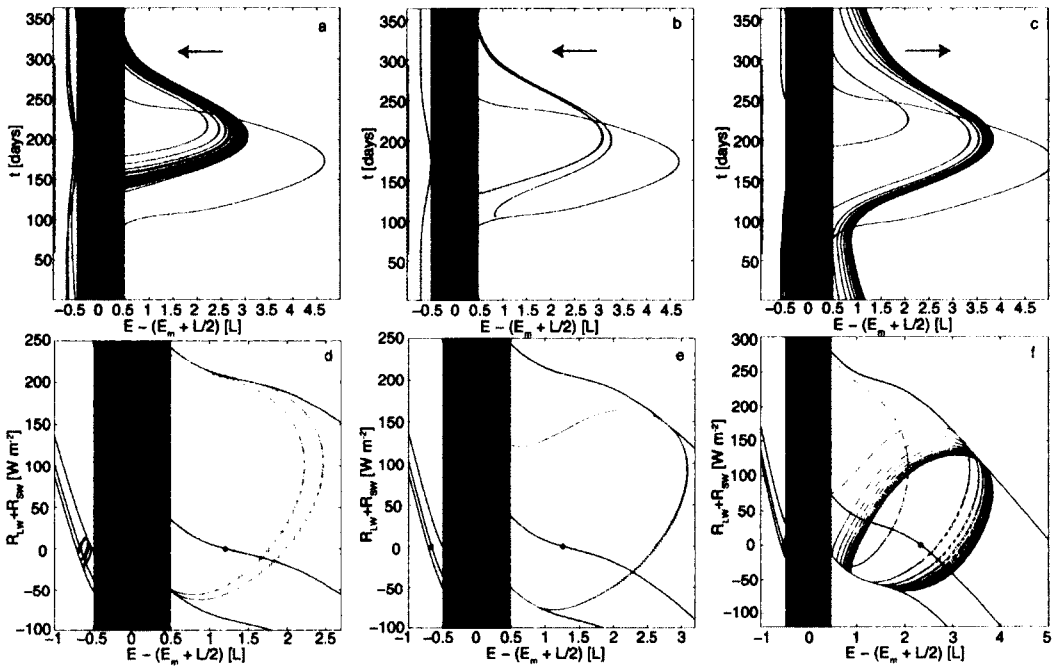

Figure 3.6. Top row: Annual cycle of the instantaneous fixed points (black curve) resulting from the surface energy budget together with typical system trajectories (blue) for various atmospheric forcing Δb near the onset and near the end of the parameter regime of bistability (Fig. 3.4b): a) transition from initially open water to perennial ice ($\Delta b = 27$ W m^{-2}), b) transition from initially open water to stable seasonal ice ($\Delta b = 28.5$ W m^{-2}), and c) transition from an initially frozen ice ocean layer to perennial open water ($\Delta b = 63$ W m^{-2}). The arrow marks the direction of consecutive annual cycles. The vertical red line denotes the time of year when the surface receives solar shortwave radiation (Arctic day). Bottom row: Corresponding panels that show the trajectories of the surface cells (red dots) in the surface cell energy vs surface energy budget space. Consecutive dots cover the same time interval. The black graphs in each panel show the annual maximum, annual average, and annual minimum surface energy budget (from top to bottom) as a function of surface cell energy. The stable (full circle) and unstable fixed points (open circle) resulting from the annual average drive are marked. A video illustrating the motion of the trajectory together with the instantaneous fixed points arising from the time varying surface energy budget is supplied at (Müller-Stoffels and Wackerbauer, 2011b).

the year. An additional stable fixed point in the open water energy regime together with an unstable fixed point within the phase transition regime exists during most part of the Arctic day. For this atmospheric forcing parameter the upper stable fixed point only occurs in conjunction with the lower stable fixed point.

Figure 3.6d shows the typical system trajectories from Fig. 3.6a in the space spanned by the surface cell energy and the surface energy budget. While the system experiences (transient) seasonal ice the trajectory spirals around the stable open water fixed point that results from the average annual surface drive. During the winter months when there is no shortwave radiation, the system trajectory follows the minimum surface budget (R_{LW}) curve along the horizontal straight line towards the lower stable fixed point. In the phase transition regime (shaded gray) the surface temperature is constant at the freezing point, and the system looses heat at a constant rate. With the onset of shortwave radiation in spring, the trajectory departs from the horizontal line upwards and to the right. The surface energy budget is still negative, but the heat loss is sufficiently reduced from the lower cells warming the surface from below. The trajectory then moves close to the unstable fixed point from the annual average surface drive. Now the direction of the trajectory depends on how much energy is entering the surface. If the incoming energy can melt the surface and thus clearly reduce the albedo, the absorbed shortwave radiation is increasing drastically to warm the surface cells; the trajectory moves quickly to the right. If the surface does not melt however, the albedo stays high and the absorption of solar shortwave radiation is small; the trajectory approaches the R_{LW} curve at lower cell energies during fall, and moves towards the stable frozen water fixed point (resulting from the annual average surface drive) to eventually spiral around that state of perennial ice. A video illustrating the motion of the trajectory together with the instantaneous fixed points arising from the time varying surface energy budget is supplied at (Müller-Stoffels and Wackerbauer, 2011b).

Figure 3.6b shows consecutive annual cycles of surface cell energy for a simulation with open water initial condition and forcing parameter $\Delta b = 28.5$ W m^{-2} slightly above the onset of bistability (Fig. 3.4b). The system converges fast to a stable seasonal ice cover state denoted by the drop of the surface cell energy below 0L in the winter months and the sudden increase in energy uptake during surface melt at day 130. The corresponding system trajectory in Fig. 3.6e shows a stable closed path around the open water fixed point

(from the annual average surface budget). During spring as the trajectory departs from the R_{LW} curve, the system is heated from below before the surface melts and takes on large amounts of shortwave energy during the summer months, similar to Fig. 3.6d. During fall the trajectory reaches the R_{LW} curve at high enough surface energies to stay on this side of the instantaneous unstable fixed point (Video, (Müller-Stoffels and Wackerbauer, 2011b)). The coalescence of the lower stable and the unstable instantaneous fixed point (Fig. 3.6b) is not an indicator for the onset of bistability as simulations with various ice albedo values show. The duration of the existence of the upper stable fixed point however is slightly longer than 150 days.

Figure 3.6c shows consecutive annual cycles of surface cell energy during a transition from perennial ice cover to open ocean for a forcing parameter $\Delta b = 63$ W m^{-2} slightly above the parameter regime of bistability. Because of the much larger forcing Δb, this transition occurs much more rapidly than the reverse transition in Fig. 3.6a, which is evident in the wider spacing of the annual cycles, especially during the winter months. Once the ice cover begins to exhibit surface melt it declines rapidly and does not refreeze; a latent heat signal is absent. The annual cycle of instantaneous fixed points still shows a time period when only the stable fixed point in the frozen water energy regime exists, but this period is much shorter than in the two cases described above. As soon as the surface cell energy reaches values above $E_m + L/2$, it increases rapidly and moves fast towards the instantaneous fixed point in the open water regime. Figure 3.6f reveals that the fixed points resulting from the annual average forcing can describe the system dynamics. The low energy stable fixed point and the unstable fixed point are close together. Heating from below (when $R_{LW} + R_{SW} < 0$) followed by surface heating from above (when $R_{LW} + R_{SW} > 0$) moves the trajectory to higher energies past the unstable fixed point. The system heats rapidly due to surface melt and stabilizes on a trajectory outside the freezing regime to circle around the stable open water fixed point.

Figures 3.6d-f reveal that the fixed points resulting from the annual average forcing do approximate the trajectories in the space spanned by the surface cell energy and the surface energy budget. Close to a bifurcation point, however, the annual average information can fail to predict the transition correctly; the onset of bistability in Fig 3.4b is shifted whereas the ending of bistability is well predicted. In such parameter regimes the dynamics is

more sensitive and instantaneous fixed points become more relevant to characterize the system dynamics, together with perturbations initiated by heating/cooling from below the surface. E.g., for the parameter $\Delta b = 27$ W m^{-2} the average surface budget predicts bistability and consequently an open water asymptotic state, in contrast to the simulation results in Figs. 3.6a and d. Surface cells cool enough during winters such that the surface cell energy is below the instantaneous unstable fixed point when it comes back to exist in the spring. As the system looses more and more energy in subsequent winters the heating from below in the spring is no longer sufficient to increase the surface cell energy sufficiently far beyond the unstable fixed point to initiate surface melting. The high surface albedo together with the diminishing solar radiation in fall yield sufficient cooling of the surface cells to reduce the surface cell energy quickly to a value below that of the unstable instantaneous fixed point. At this point the system approaches the lower stable fixed point asymptotically. Empirical data support the asymmetry between the predictability of the onset and the ending of bistability (Fig. 3.4b) by the annual average surface budget. As reported earlier in this section, simulations starting from open water remain in a high energy state of seasonal ice as long as the open water instantaneous fixed point existed for at least 150 days within a year. This criterion is not fulfilled for the parameter range between the predicted onset by the annual average drive ($\Delta b \approx -8$ W m^{-2}) and the actual onset ($\Delta b_{\downarrow} \approx 18.5$ W m^{-2}). Simulations with initially frozen water remain in a low energy state of perennial ice until the end of the predicted parameter regime for bistability ($\Delta b \approx 62$ W m^{-2}). Throughout this parameter regime the instantaneous fixed point in the frozen water energy range existed for at least 150 days within a year (Figs. 3.6a-c).

3.5 Existence of Hysteresis under Albedo Parameterization

Compared to data taken in a spatially confined area of the Arctic, step-like albedo parameterizations with temperature (or energy/enthalpy) are more suitable to describe albedo changes around the melting point (Fig. 3.3). This does not mean that the linear albedo parameterization on a wide temperature interval is unreasonable, especially since this parameterization was initially published for modeling climate data in large regions [latitudinal band model, Sellers, 1969]. In such a case it is conceivable that the average albedo across a latitudinal band changes with the average temperature of such a band in a wider

temperature interval and with a smoother behavior than a step-like function. Satellite imagery for surface albedo and respective surface temperature would reveal more insight into the dependence of albedo on temperature, but is not part of this paper (Agarwal, Moon, and Wettlaufer, 2011). We demonstrate in a simple thought experiment that the smoother approach of parameterizing the albedo is valid in ODE models of the Arctic and that the step-like (local) parameterization is linked to the smoother (nonlocal) parameterization.

We assume the Earth to be a perfect sphere with radius R, the Arctic Ocean to be the surface region between two given latitudes θ_S and θ_N, and the surface temperature $T(\theta,t)$ within this region to be a function of inclination angle θ and time t. For simplicity the time variation of surface temperature is independent on the location, and described as

$$T(\theta,t) = T_1(\theta) + T_2(t). \tag{3.8}$$

ODE models resolve time, and usually include averages of spatially varying physical quantities. A step-like nonlocal albedo parameterization could be obtained from calculating the average temperature of a latitudinal band and using this temperature to determine the corresponding albedo. Averaging the local albedos over the various latitudinal bands between θ_S and θ_N, however, yields a wider albedo parameterization,

$$\langle \alpha(T) \rangle_{[\theta_S,\theta_N]} = \frac{\int_{\theta_S}^{\theta_N} \alpha(T)\sin\theta d\theta}{\int_{\theta_S}^{\theta_N} \sin\theta d\theta}, \tag{3.9}$$

with $\langle \alpha(T) \rangle_{[\theta_S,\theta_N]}$ a function of $T_2(t)$. For simplicity we consider a linear South to North surface temperature gradient between latitude θ_S=60°N and θ_N=90°N in Eq. (3.8),

$$T_1(\theta) = \frac{T_N - T_S}{\theta_N - \theta_S}(\theta - \theta_S) + T_S, \tag{3.10}$$

and an albedo $\alpha(T)$ that can locally be described as a step-function with surface temperature T [°C],

$$\alpha(T) = \alpha_W - \frac{\alpha_W - \alpha_I}{2}\left(1 - \tanh\left(\frac{T}{T_0}\right)\right), \tag{3.11}$$

with T_0 a scaling temperature used to control the sharpness of the step. The spatially averaged surface albedo is obtained from numerical integration of Eq. (3.9) under the assumptions of Eqs. (3.10, 3.11). An analytic solution is accessible in this particular case, but not very illustrative.

Figure 3.7 shows the spatially averaged surface albedo as a function of spatially averaged surface temperature for two linear South to North surface temperature gradients. With increasing surface temperature gradient the spatially averaged surface albedo becomes wider and looses the step-like behavior, even though the local albedos obey a step-like temperature dependence [Eq. (3.11)]. The actual shape of a spatially averaged albedo depends strongly on the spatial temperature distribution in the Arctic; the linear temperature gradient was assumed to illustrate scaling properties and possible difficulties when the extended system is interpreted from an ODE approach.

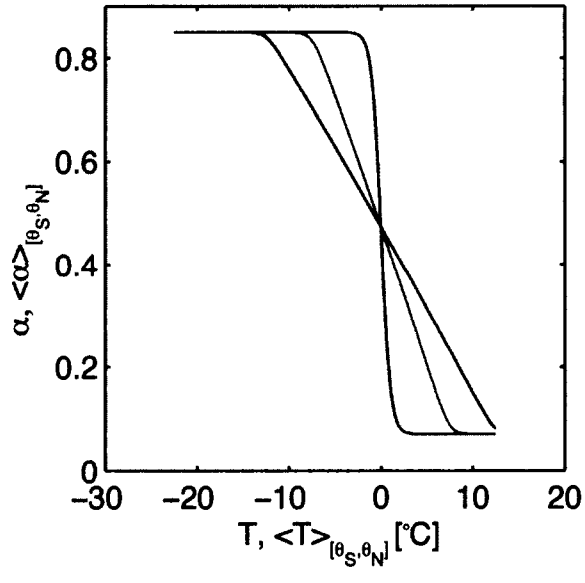

Figure 3.7. Spatially averaged surface albedo $\langle\alpha(T)\rangle_{[\theta_S,\theta_N]}$ [Eq. (3.9)] versus spatially averaged surface temperature $\langle T\rangle_{[\theta_S,\theta_N]} = \langle T_1\rangle_{[\theta_S,\theta_N]} + T_2$ [Eq. (3.8)] for $\theta_S = 60°\text{N}$, $\theta_N = 90°\text{N}$, $T_0 = 1°\text{C}$, and different temperature gradients, $T_S = 0°\text{C}$, $T_N = -15°\text{C}$ (red graph) and $T_S = 5°\text{C}$, $T_N = -20°\text{C}$ (blue graph). The local step-like albedo $\alpha(T)$ [Eq. (3.11)] is plotted for reference (black graph).

In the following we show that albedo parameterization has a significant effect on the properties of stable states and on the existence of bistability and hysteresis. The albedo parameterizations introduced in Fig. 3.3 cover the range from step-like to wide linear temperature dependence around the melting point with a fixed albedo for cold ice α_I =

0.85 and open water $\alpha_W = 0.07$. Figure 3.8 shows the annual average surface energy balance, $\langle R_{LW} + R_{SW} \rangle = R_{LW} + [1 - \alpha(T)]\langle R_{SW}^{\downarrow} \rangle$, for all albedo parameterizations. The parameter regime of bistability in the annual average surface budget is largest for step-like albedo parameterizations [ASE, Eq. (3.3); AST]. The corresponding cubic shape is progressively less pronounced for more gradual transitions (AQN, AQW, ALW) between ice albedo and open ocean albedo. For the linear albedo parameterization on a wide temperature range (ALW) the cubic feature in the surface energy budget is almost lost. For a slightly smaller difference between α_I and α_W this cubic feature would disappear, and the annual average surface budget would lack a parameter regime of bistability for that ALW parameterization.

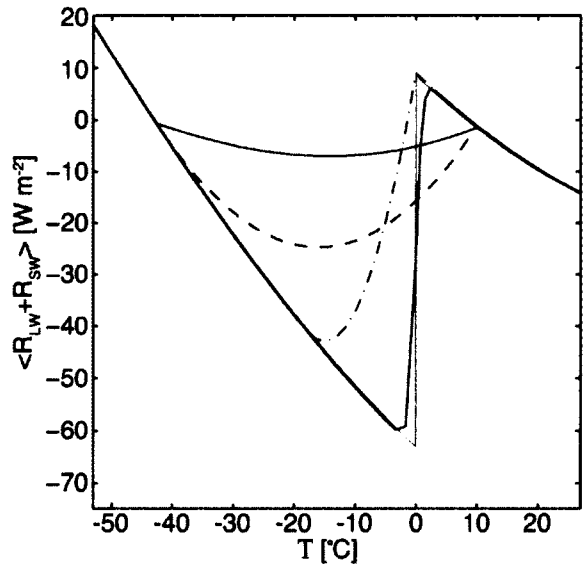

Figure 3.8. Annual average surface energy budget $\langle R_{LW} + R_{SW} \rangle$ for the albedo parameterizations introduced in Fig 3.3 and $\Delta b = 0$: ALW (grey), AQW (dashed blue), AQN (grey dash-dotted), AST (purple), ASE (orange).

Figure 3.9 shows the influence of albedo parameterization on hysteresis properties in the average cell energy $\langle E \rangle$ as a response to atmospheric forcing Δb. We find that hysteresis between perennial ice and seasonal ice (or open water) disappears for sufficiently wide/gradual albedo parameterization around the melting temperature. The step-like

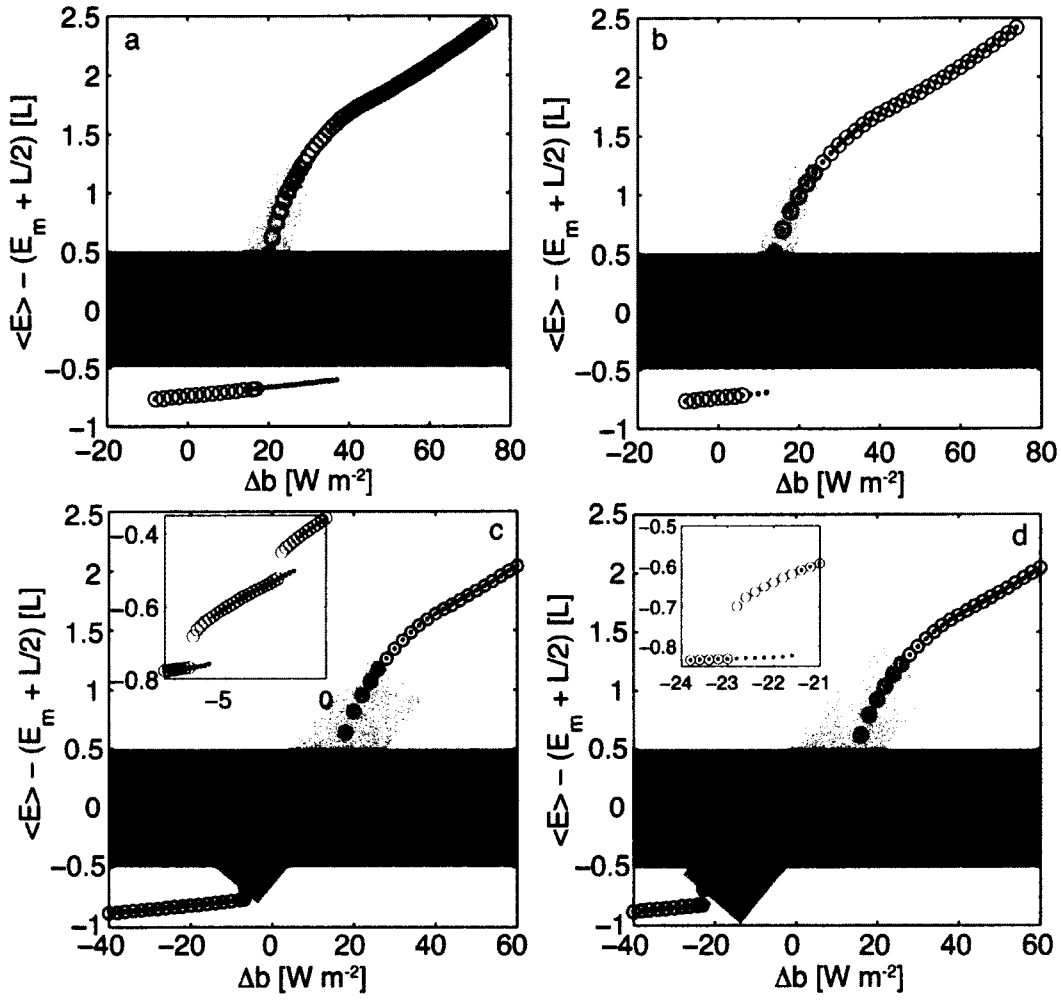

Figure 3.9. Asymptotic states of the average cell energy $\langle E \rangle$ as a response to atmospheric forcing Δb for the albedo parameterizations in Fig. 3.3: a) AST, b) AQN, c) AQW, and d) ALW. Simulations with an initially ice covered state (blue dots) started with a uniformly frozen ice-ocean layer, and simulations with an initially open water state started from a uniform water layer as in Fig. 3.4b. The ice cover is seasonal for the data points within the blue shaded area, and surface melt exists for the data points within the dark grey shaded area. Convergence is reached within numerical accuracy, i.e. doubling the simulation time does not change the values of $\langle E \rangle$.

albedo in temperature space (AST, Fig 3.3) yields bistability on a 20 W m^{-2} wide parameter interval of Δb, starting at Δb = 16 W m^{-2}. In comparison to the step-like albedo parameterization in energy space (ASE, Fig. 3.4b), the onset of bistability is at a lower Δb for AST, and the parameter regime of bistability is shortened by about 40%. Simulations that started with an open ocean initial condition (Fig. 3.9a, red circles) in the bistable region converge to seasonally ice covered solutions for a wider range of parameters than in the ASE case. The quadratic albedo parameterization on the narrow temperature interval (AQN) softens the step-like albedo change around the melting temperature; the albedo starts to deviate from α_I = 0.85 around -15°C (Fig. 3.3). This shifts the local minimum in the annual average surface energy budget from the neighborhood of the melting point (AST, ASE) to the neighborhood of -15°C (AQN, Fig. 3.8) and reduces the height of the cubic part in the annual average surface energy budget to about two thirds of the height for the step-like functions. Bistability exists on a narrow Δb-interval of width 6 W m^{-2}, with the onset of bistability at even smaller atmospheric forcing, Δb = 6 W m^{-2} (Fig. 3.9b). Once the quadratic albedo parameterization is flattened (AQW, Fig. 3.3) by widening the temperature interval according to Sellers, 1969, the local minimum in the annual average surface energy budget moves to lower temperatures, and the cubic structure is further weakened (Fig. 3.8). Hysteresis between perennial ice and seasonal ice (or open water) is lost. With increasing atmospheric forcing the system transitions rather steadily from perennial ice, to perennial ice with surface melt, to seasonal ice, and then to perennial open ocean (Fig. 3.9c). This steady transition is interrupted by two very narrow bistable regimes, in both of which the stable states are close together (insert, Fig. 3.9c). One hysteresis exists between perennial ice and perennial ice with surface melt, the other hysteresis exists between two stable states of perennial ice with surface melt but slightly different energies. For the linear albedo parameterization (ALW, Fig. 3.3) on the wide temperature interval by Sellers, 1969 the cubic structure in the annual average surface energy budget is almost lost (Fig. 3.8). The transition from perennial ice to open water is very similar to the AQW case, with again no hysteresis between perennial ice and seasonal ice or open water (Fig. 3.9d). The insert reveals a very narrow region of bistability between two slightly different energies, i.e. perennial ice and perennial ice with surface melt.

The transition between ice and ocean albedo can also be made more gradual by reduc-

ing the difference between α_I and α_W and considering a fixed temperature interval for the albedo transition around the melting point. Following Sellers, 1969, we keep $\alpha_I = 0.85$ and replace α_W with a 'non-ice' albedo value of 0.37, which is rather high as it incorporates both ocean and land. Under these conditions, the width of the bistability regime is reduced in comparison to the regimes in Figs. 3.9a and b, and the linear albedo parameterization does not yield any bistability. These results are consistent with the studies by Eisenman, 2011 and Abbot, Silver, and Pierrehumbert, 2011 which indicate that bistability disappears or is weakened for smaller differences $\alpha_I - \alpha_W$. They are also consistent with Notz, 2009, who uses these albedo values to define the slope in the albedo transition and to conclude that the ice pack is stable under perturbations.

3.6 Conclusion

The spatially extended conceptual dynamical systems model by Müller-Stoffels and Wackerbauer, 2011 addresses the stability of Arctic sea ice and feedback processes based on the thermodynamic interaction of nonlinearly coupled ice ocean cells with atmospheric and oceanic nonlinear spatiotemporal forcing. We adjust several model components to include observations from the Arctic region. The longwave radiative budget considers clear sky data provided by ARM, and variations in albedo parameterization were inspired by data provided through the SHEBA project and the work by Sellers, 1969, Thorndike, 1992, Eisenman and Wettlaufer, 2009 and Notz, 2009. These adjustments follow our core model development paradigm to base the change in physical variables and parameters on the change in system state and not on explicit time-dependences in physical quantities that are based on todays or past observation. This is particularly relevant when investigating system dynamics and feedback processes under a broader range of climatic conditions than accessible by reliable data.

The complexity of the dynamical system is evident in a seemingly minor change in the shape of a model component that significantly changes the outcome of certain model simulations. Adjusting the longwave radiative budget to observations provided by ARM from its site in Barrow, Alaska, results in seasonal ice being a stable state, where previously only perennial ice cover and perennially open ocean were stable solutions (Müller-Stoffels and Wackerbauer, 2011). This stable annual cycle of seasonal ice is a special case of the

higher energy stable state and becomes the open ocean stable state for larger atmospheric forcing.

The annual average surface forcing provides an approximate tool to locate bistability in parameter space. For bistability to exist in our model, it is necessary that the fixed points induced solely by the annual average surface forcing exhibit a parameter regime of bistability. Further analysis of the (instantaneous) fixed points induced solely by the instantaneous surface drive reveals that in much of the parameter regime of bistability only one of the two stable (instantaneous) fixed points exists for most of the annual cycle. The system can be considered to be of cyclically varying stability, possibly displaying time intervals with the existence of a single stable state in the frozen energy regime, a single stable state in the open water energy regime, or with coexistence of both of these stable states. We find that the instantaneous fixed points are essential for the understanding of the system dynamics, particularly in the neighborhood of a bifurcation point. They provide insight into the interaction of the surface energy with the radiative forcing and the underlying body of ice/water. Surface cell energies are tracking the instantaneous fixed points, but are rarely close due to the inertia of the underlying system, which releases/stores energy at a limited rate.

There is an ongoing discussion in the literature about the reversibility of sea ice loss and the existence of a tipping point (Walker, 2006; Lenton et al., 2008; Eisenman and Wettlaufer, 2009; Notz, 2009). The albedo parameterization (among others) is distinctly different between ODE models exhibiting hysteresis and tipping point behavior and models exhibiting a smooth continuous sea ice decrease under increasing atmospheric forcing (Sellers, 1969; Thorndike, 1992; Eisenman and Wettlaufer, 2009; Notz, 2009; Eisenman, 2011). We choose ice and ocean albedos that are commonly used in GCMs (Liu, Zhang, and Horton, 2007) and manipulate the shape of albedo parametrization around the melting point. We show that albedo parametrization is key to distinct transition behavior. The hysteresis between perennial ice and seasonal ice is less pronounced for albedo parameterizations with a more gradual transition between ice and ocean albedo around the melting temperature. For the linear albedo parameterization on the wide temperature interval by Sellers, 1969 the transition from perennial ice to open water is smooth with increasing atmospheric forcing and stable under perturbations.

An interesting question is of course, which albedo parameterization to pick in a conceptual model. Local measurements (SHEBA) reveal that while the albedo starts to diminish slightly below the freezing point, step-like parameterizations capture the transition better than wide gradual transitions. Spatial averaging, however, reconciles the local step-like albedo behavior with the more gradual albedo transition, indicating that gradual parameterizations can provide a bulk albedo for the model Arctic as a whole. Consequently, the albedo parametrization is model dependent. If only local parameters enter into an ODE model then the outcome is local. For a regional ODE model the (spatially averaged) albedo parameterization depends on e.g., temperature gradients in the region, the actual forms of the local albedo parameterization. Further studies are necessary to better represent albedo parameterization in conceptual models and models per se, particularly, since the existence of hysteresis is crucially dependent on the albedo parameterization (this paper), and since small changes to the ice albedo severely change the outcome of GCM's ice extent predictions (Eisenman, Untersteiner, and Wettlaufer, 2007).

Many GCMs produce a seasonal ice state under increased greenhouse gas emission scenarios (IPCC, 2007). The initial conditions of these GCMs usually allow for some region of open water at lower latitudes. Latitudinal differences in shortwave fluxes generate an inherent spatial inhomogeneity that induce lateral fluxes. This is a significant difference to ODE models and cannot be overlooked when translating ODE model to GCM results. This paper explores a spatially confined model domain at latitude 80°N. Insolation values for other latitudes would shift parameter ranges for bistability and seasonal ice. In ODE models the common definition of seasonal ice is that the whole model domain will be ice covered for some time every year. The definition of seasonal ice in a GCM is that there exists a region within the model domain that will be ice covered for some time every year. Inherent in the difference is the significant limitation of ODE models regarding spatial resolution. Our findings that (1) smoother albedo parametrizations have significant impact on the asymptotic behavior of ODE models, and that (2) spatial scaling gives a smoother albedo parametrization, are significant in understanding and interpreting ODE model results in a GCM context.

The lattice structure of our model enables spatial inhomogeneities in the ice-ocean layer to be implemented rather straightforward. We adjust the lattice to describe a latitudinal

transect between 60° and 90°N (with one-tenth of a degree resolution) and include lateral atmospheric heat transfer via diffusion of surface temperatures and enhanced heat transfer in the ocean mixed layer via vertical and horizontal eddy thermal diffusivities. Preliminary results show that bistability in the annual average ice edge location is strongly influenced by the albedo parametrization, and that a locally step-like albedo parameterization results in a wider spatially averaged albedo along the transect.

Acknowledgements

MMS was supported by a Global Change Student Research Grant sponsored by the Cooperative Institute for Alaska Research (CIFAR) and a UAF Graduate School Thesis Completion Grant; RW was supported by funding from the Department of Energy through grant number DE-SC0001898. This research was supported by the Arctic Region Supercomputing Center at the University of Alaska Fairbanks. The authors would like to thank Hajo Eicken for valuable discussions and the chance to experience sea ice first hand (MMS).

References

Abbot, D, M Silver, and R Pierrehumbert (2011). "Bifurcations leading to summer arctic sea ice loss". In: *Journal of Geophysical Research* 116, p. D19120. DOI: doi:10.1029/2011JD015653.

Agarwal, S, W Moon, and J Wettlaufer (2011). "Decadal to seasonal variability of Arctic sea ice albedo". In: *Geophysical Research Letters (Preprint, arXiv:1109.3058v1)* 38, pp. 1–4.

Andreas, E., C. Fairall, P. Guest, and O. Persson (1998). *SHEBA ASFG PAM surface temperature data*. URL: http://www.eol.ucar.edu/projects/sheba/.

ARM Data Archive (2010). URL: http://www.archive.arm.gov.

Bony, S, R Colman, V Kattsov, R Allan, C Bretherton, J Dufresne, A Hall, S Hallegate, M Holland, W Ingram, D Randall, B Soden, G Tselioudis, and M Webb (Aug. 2006). "How well do we understand and evaluate climate change feedback processes?" In: *Journal of Climate* 19, pp. 3445–3482.

Campbell and J Norman (1998). *Introduction to environmental biophysics*. Second. New York, NY: Springer Science+Business Media.

Crawford, T and C Duchon (Apr. 1999). "An improved parameterization for estimating effective atmospheric emissivity for use in calculating daytime downwelling longwave radiation". In: *Journal of Applied Meteorology* 38.4, pp. 474–480.

Cross, M and P Hohenberg (1993). "Pattern formation outside of equilibrium". In: *Reviews of Modern Physics* 65, pp. 851–1112. DOI: doi:10.1103/RevModPhys.65.851.

DeWeaver, E, E Hunke, and M Holland (May 2008). "Comment on"On the reliability of simulated Arctic sea ice in global climate models"by I. Eisenman, N. Untersteiner, and JS Wettlaufer". In: *Geophysical Research Letters* 35.4, p. 4501.

Eisenman, I (2011). *Factors controlling the stability of the sea ice cover*. Presentation at SIAM Conference on Applications of Dynamical Systems, Snowbird, UT, USA.

Eisenman, I, N Untersteiner, and J Wettlaufer (May 2007). "On the reliability of simulated Arctic sea ice in global climate models". In: *Geophysical Research Letters* 34.10, pp. 1–4.

Eisenman, I and J Wettlaufer (Jan. 2009). "Nonlinear threshold behavior during the loss of Arctic sea ice". In: *PNAS* 106.1, pp. 28–32.

Goff, J (1957). "Saturation pressure of water on the new Kelvin temperature scale". In: *Transactions of the American society of heating and ventilating engineers*, pp. 347–354.

IPCC (2007). *Climate Change 2007: The physical science basis, summary for policymakers*. Tech. rep. Intergovernmental Panel on Climate Change.

Lenton, T, H Held, E Kriegler, J Hall, W Lucht, and H Schellnhuber (2008). "Tipping elements in the Earth's climate system". In: *PNAS* 105, pp. 1786–1793.

Liu, J, Z Zhang, and R M Horton (2007). "Evaluation of snow / ice albedo parameterizations and their impacts on sea ice simulations". In: *International Journal of Climatology* 91, pp. 81–91.

Maykut, G and N Untersteiner (1971). "Some results from a time-dependent thermodynamic model of sea-ice". In: *Journal of Geophysical Research* 76, pp. 1550–1575.

Müller-Stoffels, M and R Wackerbauer (2011). "Regular network model for the sea ice-albedo feedback in the Arctic". In: *Chaos* 21.1.

— (2011b). *Animations supporting Figure 5 d, e and f*. URL: http://www.youtube.com/user/mmuellerstoffels.

North, G (1984). "Small Ice Cap Instability in Diffusive Climate Models". In: *Journal of the Atmospheric Sciences* 41.23, pp. 3390–3395. ISSN: 1520-0469.

Notz, D (Dec. 2009). "The future of ice sheets and sea ice: Between reversible retreat and unstoppable loss". In: *PNAS* 106.49, pp. 20590–20595.

Paulson, C (1998). *SHEBA ice camp summer leads albedo data.* URL: `http://www.eol.ucar.edu/projects/sheba/`.

Perovich, D (1998). *SHEBA spectral light transmittance project data.* URL: `http://www.eol.ucar.edu/projects/sheba/`.

Perovich, D, T Grenfell, B Light, and P Hobbs (Oct. 2002). "Seasonal evolution of the albedo of multiyear Arctic sea ice". In: *Journal of Geophysical Research* 107.C10.

Prata, A (July 1996). "A new long-wave formula for estimating downward clear-sky radiation at the surface". In: *Quarterly Journal of the Royal Meteorological Society* 122.533, pp. 1127–1151.

Satterlund, D (1979). "An improved equation for estimating long-wave radiation from the atmosphere". In: *Water Resources Research* 15.6, pp. 1649–1650.

Sellers, W (1969). "A global climatic model based on the energy balance of the Earth-atmosphere system". In: *Journal of Applied Meteorology* 8, pp. 392–400.

Shine, K and A Henderson-Sellers (1985). "The sensitivity of a thermodynamic sea ice model to changes in surface albedo parameterization". In: *Journal of Geophysical Research* 90.D1, pp. 2243–2250.

Stahlke, D and R Wackerbauer (2009). "Transient spatiotemporal chaos is extensive in three reaction-diffusion networks". In: *Physical Review E* 80, p. 056211. DOI: `doi:10.1103/PhysRevE.80.056211`.

Thorndike, A (June 1992). "A toy model linking atmospheric and thermal radiation and sea ice growth". In: *Journal of Geophysical Research* 97.C6, pp. 9401–9410.

Walker, G (2006). "The tipping point of the iceberg". In: *Nature* 441, p. 802.

Winton, M (2008). "Sea-ice albedo feedback and nonlinear Arctic climate change". In: *Arctic sea ice decline: observations, projections, mechanisms, and implications.* Ed. by C. M. Bitz E. T. DeWeaver and L. B. Tremblay. American Geophysical Union, pp. 111–131.

Chapter 4

Sea ice retreat in a regional scale regular network model

4.1 Introduction

The recent trends of warming and record low sea ice extent and sea ice volume in the Arctic have been linked to increased surface forcing due to elevated levels of greenhouse gases in the atmosphere (IPCC, 2007; Stroeve et al., 2007). Most state-of-the-art general circulation models (GCMs) do not capture the recent sharp decline of sea ice extent. The inter-model divergence of ice extent projections for 2100 is large. Some models predict the loss of all Arctic sea ice by the end of the century; others predict a reduction to levels observed today (Stroeve et al., 2007). The observed and projected warming trends for the planet are amplified in the Arctic via several feedback mechanisms (Bony et al., 2006). Studies isolating the ice albedo feedback suggest that it is a major mechanism in the retreat of the Arctic sea ice (Thorndike, 1992; Eisenman and Wettlaufer, 2009; Müller-Stoffels and Wackerbauer, 2011; Müller-Stoffels and Wackerbauer, 2012; Eisenman, 2012; Abbot, Silver, and Pierrehumbert, 2011), although it is not thought to be the strongest feedback in the climate system (Bony et al., 2006). It has also been shown that slight adjustments in albedo values can significantly change the outcome of GCMs regarding sea ice extent (Eisenman, Untersteiner, and Wettlaufer, 2007).

Much of the discussion on ice albedo feedback is centered around the question of how the sea ice cover will retreat and if this retreat is reversible (Walker, 2006; Lenton et al., 2008). Low order modeling approaches (ordinary differential equations [ODE], Thorndike, 1992; Eisenman and Wettlaufer, 2009; Notz, 2009; Müller-Stoffels and Wackerbauer, 2011) exhibit both reversible and irreversible sea ice loss. The parametrization of the transition of albedo values from ice to water determines wether a low order system exhibits bistability. Sharp transitions result in bistable systems, which exhibit irreversible sea ice loss. With smoother transitions the parameter interval of bistability is reduced or annihilated (Müller-Stoffels and Wackerbauer, 2012; Eisenman, 2012; Abbot, Silver, and Pierrehumbert, 2011). Local observational data of albedo support a relatively sharp decline of albedo with temperature around the freezing point, but spatial averaging of local sharp transitions results in smoother regional albedo parametrizations based on local measurements (Müller-Stoffels and Wackerbauer, 2012). A recent study of one GCM reports no

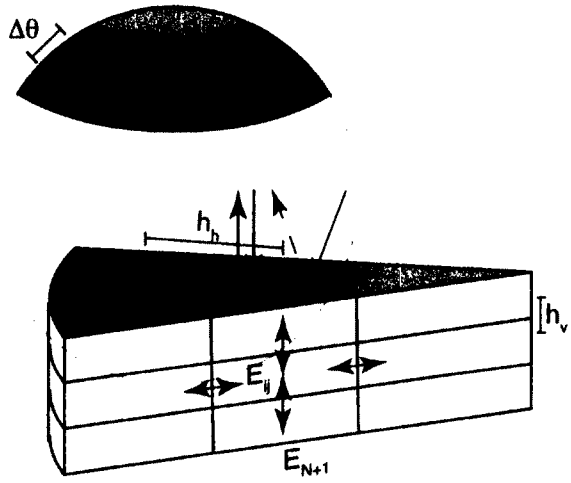

Figure 4.1. The ocean mixed layer from latitude 60° to 90° N is mapped onto a $N \times M$ grid of coupled cells. Latitudinal bands of width $\Delta\theta$ have varying surface areas A and volumes V, which is reflected in the laterally varying size of the grids cells. Cells exchange energy with their direct neighbors (light blue arrows). Cells at the bottom of the grid exchange energy with a constant energy (E_{N+1}) ocean. At the surface the grid is forced via shortwave (R_{SW}, red arrows), longwave (R_{LW}, dark blue arrows) and lateral atmospheric fluxes ($k_{\text{eff}}/h_h(T_{j+1} - T_j)$ and $k_{\text{eff}}/h_h(T_{j-1} - T_j)$, orange arrows).

evidence of irreversibility (Armour et al., 2011). This leads to the question whether bistability with a sharp albedo transitions in ODE-type models is mitigated by spatial effects in full climate models.

This study addresses a link between irreversible spatially confined models with sharp local albedo parametrization and the reversibility of sea ice retreat in a regional scale model (Sec. 4.2) comprised of coupled local cells known to exhibit bistability. Thus, spatial ice albedo feedback effects are studied within the confines of a model in which local effects are well understood (Müller-Stoffels and Wackerbauer, 2011; Müller-Stoffels and Wackerbauer, 2012). Compared to energy balance models (EBM, aka latitudinal band models, e.g., Sellers, 1969; North, 1984; Winton, 2008), the model presented here has high spatial and temporal resolution.

The albedo parametrization influences the mode of ice retreat and the existence of asymptotic states with seasonal ice cover in this regional model (Sec. 4.3). An inverse

ice thickness parameter reveals a regime change in predominant melting mechanisms between simulations with stable perennial ice at high latitudes and unstable perennial ice cover (Sec. 4.4). Comparison with Arctic sea ice extent and sea ice volume data suggests that this record exhibits a similar regime change in the record low sea ice volume years. The ice albedo feedback is assessed (Sec. 4.5) and it is shown that lateral coupling plays an important role in the intensity of the feedback.

4.2 Model

A regular network model that resolves the spatial coordinate in the North-South and the vertical direction and incorporates spatial inhomogeneity of latitudinal bands is presented. The ocean mixed layer is mapped from latitude 60° to 90°N onto a $N \times M$ grid of coupled cells. The horizontal grid resolution is 0.1°, which renders the horizontal (North-to-South) center-to-center cell spacing to be $h_h = 11100$ m. The vertical grid spacing $h_v = 0.3$ m is the same as in Müller-Stoffels and Wackerbauer, 2011 and Müller-Stoffels and Wackerbauer, 2012 and allows for a relatively high resolution of ice thickness. Each cell volume V and surface area A (upward and downward facing surfaces) is adjusted depending on its latitudinal location to account for the spherical geometry of the polar region. The model grid is forced with latitude dependent shortwave fluxes R_{SW}, temperature-dependent longwave fluxes R_{LW}, temperature-dependent lateral atmospheric fluxes ($k_{\text{eff}}/h_h(T_{j+1} - T_j)$ and $k_{\text{eff}}/h_h(T_{j-1} - T_j)$), and each grid column is connected to a constant energy ocean cell E_{N+1}. The energy E_{N+1} is equivalent to an underlying ocean temperature of 274.5 K. Due to the inhomogeneous cell size, all extensive quantities are location dependent and heat transfer equations are performed using energy density, an intensive quantity.

In the following, generic indices, $i \in [1,N]$ for rows and $j \in [1,M]$ for columns are used. The index j indicates a model cell at a specific latitude, where the latitude of that cell is determined by

$$\theta_j = \theta_S + (j-1)\Delta\theta, \text{ for } j = 1,\ldots,M, \tag{4.1}$$

with $\Delta\theta$ the latitudinal resolution (angular distance between horizontally adjacent cell centers) of our model, θ_S the southernmost latitude used, and M the horizontal grid size.

The volume V for each latitudinal band at latitude θ and of width $\Delta\theta$ is

$$\begin{aligned} V(\theta,\Delta\theta) &= \int_0^{2\pi}\int_{\theta+\frac{\Delta\theta}{2}}^{\theta-\frac{\Delta\theta}{2}}\int_{R_e-h_v}^{R_e} r^2\sin\theta' dr d\theta' d\phi, \\ &= \frac{2}{3}\pi\Big(R_e^3-(R_e-h_v)^3\Big)\Big(\cos(\theta-\frac{\Delta\theta}{2})-\cos(\theta+\frac{\Delta\theta}{2})\Big), \end{aligned} \tag{4.2}$$

with $R_e = 6371$ km being the earth radius (we assume a perfect sphere). The surface area A, that is the area of the upward and downward faces of each cell, is

$$\begin{aligned} A(\theta,\Delta\theta) &= R_e^2\int_0^{2\pi}\int_{\theta+\frac{\Delta\theta}{2}}^{\theta-\frac{\Delta\theta}{2}}\sin\theta' d\theta' d\phi, \\ &= 2\pi R_e^2\Big(\cos(\theta-\frac{\Delta\theta}{2})-\cos(\theta+\frac{\Delta\theta}{2})\Big). \end{aligned} \tag{4.3}$$

This renders the *model equation* for a given cell (i,j) at time step $n+1$,

$$\begin{aligned} E_{i,j}^{n+1} &= E_{i,j}^n \\ &+ \zeta_v\sum_{k=-1}^{1} D_{[i,i+k],j}(E_{i+k,j}^n - E_{i,j}^n) \\ &+ \zeta_h\sum_{k=-1}^{1} D_{i,[j,j+k]}V_j(E_{i,j+k}^n V_{j+k}^{-1} - E_{i,j}^n V_j^{-1}) \\ &+ \delta_{1i}\Delta t A_j(R_{SW}+R_{LW}+k_{\text{eff}}/h_h(T_{j+1}+T_{j-1}-2T_j)) \\ &+ \delta_{Ni}\zeta_v D_{[i,N+1],j}(E_{N+1}-E_{i,j}^n), \end{aligned} \tag{4.4}$$

for $i \in [1,N]$ and $j \in [1,M]$, where ζ is the horizontal (h) and vertical (v) global coupling constant, D is the horizontal and vertical local coupling constant (thermal diffusivity), δ_{ij} is the Kronecker delta, k_{eff} describes the effective heat transfer in the near surface atmosphere based on temperature gradients, V is the respective cell volume and A the respective cell horizontal surface area, R_{SW} is the absorbed shortwave flux density, R_{LW} is the longwave flux density budget, T is the surface temperature, and E_{N+1} is the constant cell energy of the ocean reservoir.

A *phase function* ϕ is used to control state specific variables,

$$\phi(E) = \frac{1}{\pi}\arctan\Big(\frac{c}{L}(E-E_m-\frac{L}{2})\Big)+\frac{1}{2}, \tag{4.5}$$

with $L = Vl\frac{\rho_I+\rho_W}{2}$ the local volumetric latent heat of a cell, $E_m = C_I V T_0$ the local energy of ice at the melting point, T_0 the melting temperature of ice (assumed to be 273 K), and c

a sharpness factor. The phase function is used to calculate the phase-dependent values of the thermal diffusivity D and the surface albedo α. Different to Müller-Stoffels and Wackerbauer, 2011; Müller-Stoffels and Wackerbauer, 2012 the factor $1/L$ was introduced and the value of c was changed. This is merely for computational reasons as calculations of the arctan for very large arguments appeared to be sensitive to rounding errors when using MATLAB.

Heat transfer on the molecular scale is characterized via a thermal diffusivity. Such a measure does not incorporate the fact that fluids move and mix due to temperature, solute (salt) and mechanical (wind) gradients. These effects can greatly enhance the transport of a heat signal through the medium. To incorporate such processes not accessible in diffusion models, it is common to employ effective thermal diffusivities that account for bulk motion of the medium. Steward, 2005 gives a range of values for *eddy thermal diffusivities* in the oceans; that vary in the horizontal and vertical direction. Here conservative values for both are used, with a vertical eddy diffusivity of $D = 1.08 \times 10^{-5}$ m^2 s^{-1} and a horizontal eddy diffusivity of $D = 108$ m^2 s^{-1}. In this model D is a calculated value Eq. (4.6); the physical quantity actually modified is the thermal conductivity of water, $k_W^{(v)} = 45$ W (m K)$^{-1}$ and $k_W^{(h)} = 45 \times 10^7$ W (m K)$^{-1}$, with

$$D_{i,j} = \frac{k_I + (k_W^{(x)} - k_I)\phi_{i,j}}{C_I + (C_W - C_I)\phi_{i,j}} \tag{4.6}$$

where x is v or h depending on the direction heat flow is to be calculated for. The thermal conductivity of ice k_I is assumed to be isotropic and the heat capacities C are material constants. The thermal diffusivity D as used in Eq. (4.4) is a local, phase-dependent coupling constant. It depends directly on the phase state of two neighboring cells involved in an energy exchange. For horizontally neighboring cells (i, j_1) and (i, j_2) respectively we calculate

$$D_{i,[j_1,j_2]} = 2\frac{D_{i,j_1} D_{i,j_2}}{D_{i,j_1} + D_{i,j_2}}. \tag{4.7}$$

An analogous argument holds for vertical coupling with $D_{[i_1,i_2],j}$.

The *longwave flux density budget* R_{LW} is modeled after clear sky radiation balance data for Barrow, AK (*ARM Data Archive* 2010; Müller-Stoffels and Wackerbauer, 2012),

$$R_{LW} = [\varepsilon_a(T) - \varepsilon_s]\sigma T^4 + aT + b, \tag{4.8}$$

Table 4.1. Physical constants and system parameters used in all simulations unless stated otherwise.

Symbol	Description	Value
l	Latent heat of fusion	3.35×10^5 J kg^{-1}
ρ_W	Density of water	1000 kg m^{-3}
ρ_I	Density of ice	917 kg m^{-3}
C_W	Heat capacity of water	4.18×10^6 J (m^3 K)$^{-1}$
C_I	Heat capacity of ice	1.93×10^6 J (m^3 K)$^{-1}$
$k_W^{(h)}$	Horizontal eddy thermal conductivity for water	45×10^7 W (m K)$^{-1}$
$k_W^{(v)}$	Vertical eddy thermal conductivity for water	45 W (m K)$^{-1}$
k_I	Thermal conductivity of ice	2.2 W (m K)$^{-1}$
T_0	Melting/Freezing temperature of water	273 K
α_W	Water albedo	0.07
α_I	Ice albedo	0.85
θ	Latitudinal angle	60 to 89.9° N
$\Delta\theta$	Latitudinal resolution	0.1°
τ^m	Optical thickness for zenith angle ψ	0.7^m; $m = \cos^{-1}\psi$
E_{N+1}	Ocean reservoir energy. Equivalent to $T = 274.5$ K	$E_m + 1.02L$
Δt	Time step	0.25 h
h_v	Vertical cell dimension	0.3 m
h_h	Horizontal cell dimension	11.1 km
$\zeta_v = \frac{\Delta t}{h_v^2}$	Vertical coupling constant	1×10^4 s m^{-2}
$\zeta_h = \frac{\Delta t}{h_h^2}$	Horizontal coupling constant	7.3×10^{-6} s m^{-2}
k_{eff}/h_h	Atmospheric heat flux coefficient	2.7 W (m^2 K)$^{-1}$
N	Number of vertical cells	75
M	Number of horizontal cells	300
c	Sharpness factor	10^4

with the surface emissivity ε_S, the atmospheric emissivity $\varepsilon_a(T) = \varepsilon_s \exp(-7.7 \times 10^{-5} T^2 + 0.028T - 3.1)$, $b = b_0 + \Delta b$, $a = -1.05$ W m^{-2} K^{-1} and $b_0 = 301$ W m^{-2} are empirical constants, and Δb is a bifurcation parameter (additional surface forcing). The first part of Eq. (4.8) is the Stefan-Boltzmann law with a temperature dependent atmospheric emissivity. The second part is used to correct for lateral atmospheric fluxes from lower latitudes based on ARM data from Barrow, AK. We would expect that the coefficients a and b_0 are different in other locations of the Arctic. But due to the lack of measurements of similar quality (14 year high-resolution record) to ARM's Barrow data we will use Eq. (4.8) for all latitudes and adjust our forcing term Δb accordingly.

An *effective surface heat flux* term $k_{\text{eff}}/h_h(T_{j+1} + T_{j-1} - 2T_j)$ has been added to model near surface atmospheric fluxes due to temperature gradients similar to the approach to interaction of an ODE model of the Arctic with lower latitudes (Eisenman and Wettlaufer, 2009). The relationship between temperatures T and energies E is $E = C_I V T$ and $T \leq T_0$. In the liquid phase the energy is converted with $E = E_m + L + C_W V(T - T_0)$ for $T > T_0$. For energies during the phase transition $E_m \leq E \leq E_m + L$ the temperature is constant at $T = T_0$.

The *absorbed shortwave radiative flux density* is modeled after Campbell and Norman, 1998,

$$R_{SW}(\theta) = (1 - \alpha) S_0 \cos\psi(\theta)[\tau^m + 0.3(1 - \tau^m)], \tag{4.9}$$

with $S_0 \cos\psi(\theta)$ the incoming perpendicular shortwave flux density at the top of the atmosphere, S_0 the solar constant, ψ the zenith angle, and α the surface albedo; the term in square brackets is the optical thickness for direct (first term) and diffuse (second term) radiation. The exponent $m = (\cos\psi)^{-1}$ adjusts for the optical path length through the atmosphere. The zenith angle ψ is a function of latitude and declination angle and, thus, indirectly a function of time.

The model approach given in Eq. (4.4) is an approximation. Surface areas and volumes are calculated for regions of a sphere. However, small changes to the surface area and volume with changing radius are ignored. This is because the depth of the model is six orders of magnitude smaller than Earth's radius. In the exact solution, R_E would have to be replaced by $R_i = R_E - (i-1)h_v$, but with $N = 75$ and $h_v = 0.3$ m, $R_i \approx R_E \; \forall \, i$. The difference equation (Eq. (4.4) is not used in spherical coordinates, but the geometry is mapped onto a grid and the equation is solved in Euclidean geometry. The approach is valid for the

given type of local calculations and using a relatively high horizontal resolution (1/10th of a latitudinal degree). The energy in the horizontal direction (Eq. 4.4, line 3) is not fully conserved. Horizontally neighboring cells have different volumes; to solve Eq. (4.4) we need to work with energy densities $E_{i,j}/V_j$. For example, if we have three horizontally adjacent cells with energies E^n_{j-1}, E^n_j and E^n_{j+1}, with $E^n_{j-1}/V_{j-1} = E^n_j/V_j = E^n_{j+1}/V_{j+1}$ and no forcing or vertical energy flow, it follows from line 3 of Eq. (4.4) that

$$\sum_{k=j-1}^{j+1} E_k^{n+1} = \sum_{k=j-1}^{j+1} E_k^n + D\left[E^n_{j-1}\left(\frac{V_j}{V_{j-1}} - 1\right) + E^n_j\left(\frac{V_{j-1}+V_{j+1}}{V_j} - 2\right) + E^n_{j+1}\left(\frac{V_j}{V_{j+1}} - 1\right)\right], \tag{4.10}$$

where the term in square brackets should be zero. The error introduced can be neglected for small $\Delta\theta$, with

$$\frac{V_{j-1}+V_{j+1}}{V_j} = 2\cos\Delta\theta \underset{\Delta\theta \ll 1}{\approx} 2, \tag{4.11}$$

which can be seen using Eq. (4.2), and the fact that $\theta_{j\pm1} = \theta_j \pm \Delta\theta$. A similar argument holds for $V_j/V_{j\pm1} \approx 1$. The order of magnitude of the error per time step introduced by the approximation is about 1 $\mathrm{nWm^{-2}}$. Thus, in an open system which exchanges on the order of 10 $\mathrm{Wm^{-2}}$ per time step, the error can be neglected. The above approximation fails in the case of periodic boundary conditions where a very large volume could end up being connected to a very small volume.

4.2.1 Albedo parametrizations

As is evident from Surface Heat and Energy Budget of the Arctic (SHEBA) data (Fig. 4.2a and as presented in Müller-Stoffels and Wackerbauer, 2012) given by Perovich, 1998 [light blue] and Paulson, 1998 [light red] plotted against surface temperature (Andreas et al., 1998), the ice albedo is reduced before the ice reaches the melting temperature (0 °C). To model this, a second step, centered at $E = E_m - 0.015L$ (equivalent to −2.5 °C), was incorporated into the sharp step-like albedo parametrization (SAT) used in in Müller-Stoffels and Wackerbauer, 2011 and Müller-Stoffels and Wackerbauer, 2012. The green graph in Fig. 4.2 shows a sharp double step transition (DST1) from the albedo value for cold ice $\alpha_{I,\max}$ to the value for warm/ponding ice $\alpha_{I,\min}$. The purple graph shows a softened transition between the same values (DST2). This parametrization was developed as it better fits the transition suggested by the data. The DST parametrizations are realized using

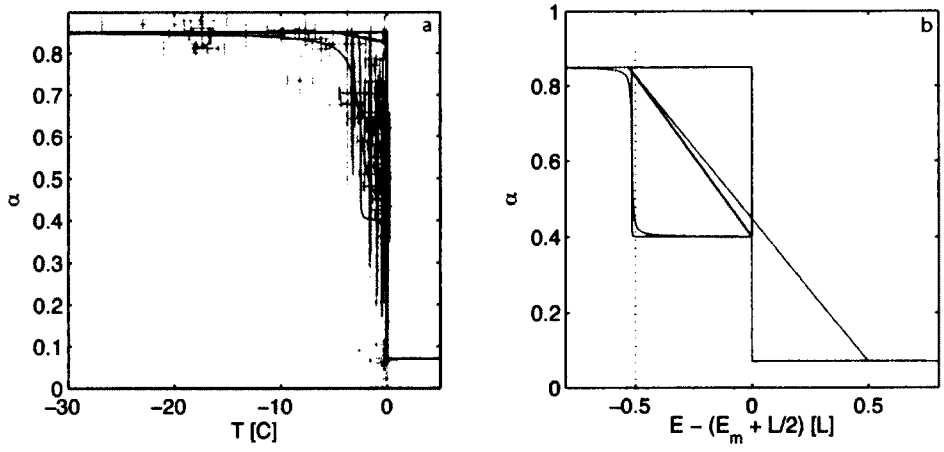

Figure 4.2. a: Surface albedo parametrizations plotted against surface temperature. Blue is a sharp step transition (SAT) albedo; Red is a gradual linear transition (GLT); Black is a linear-step transition (LST); Green is a sharp double step transition (DST1); Magenta is a soft double step transition (DST2). For comparison SHEBA ice albedo data [light blue] Perovich, 1998 and SHEBA lead albedo data [light red] Paulson, 1998 as discussed in (Müller-Stoffels and Wackerbauer, 2012).
b: Surface albedo parametrizations versus surface energy.
The temperature scale in Fig. a does not match the energy scale in Fig. b.

$$\alpha(E) = \alpha_{I,\max} - (\alpha_{I,\min} - \alpha_W)\phi(E,c) - (\alpha_{I,\max} - \alpha_{I,\min})\phi(E + 0.015L, c_d),$$

where DST1 uses the standard sharpness factor $c_d = c$ (Tab. 4.1) to calculate ϕ and for DST2 uses $c_d = 250$.

Two more albedo parametrizations were added for control purposes and as intermediate cases. The red curve in Fig. 4.2 transitions gradually and linearly (GLT) from the maximum ice albedo $\alpha_{I,\max}$ at $E = E_m - 0.03L$ ($T = -5$ °C) to water albedo α_W at $E = E_m + L$. The black graph transitions gradually and linearly from the maximum ice albedo $\alpha_{I,\max}$ at $E = E_m + 0.03L$ to the minimum ice albedo $\alpha_{I,\min}$ at $E = E_m + L/2$, then it steps sharply down to water albedo α_W. This albedo parametrization is referred to as LST.

Fig. 4.2b shows the albedo parametrizations from Fig. 4.2a but in energy space. This illustrates that the albedo parametrizations are not functions in the mathematical sense in temperature space as the whole region of latent heat release from the energy picture is folded into a single value $T = 0$ °C.

4.3 Ice extent under surface forcing

Simulations were performed with the albedo parametrizations introduced in Sec. 4.2.1 under open water initial conditions (OWIC), ice covered initial conditions (ICIC) and varying surface forcing. For all albedo parametrizations three distinct states can be identified: (i) closed ice cover for all latitudes, (ii) partial ice cover with open water at southern latitudes and perennial ice at northern latitudes, and (iii) open water for all latitudes, with (transient) seasonal ice. Figures 4.3 and 4.4 show the asymptotic states of the ice edge latitude versus the bifurcation parameter Δb for the albedo parametrizations (Fig. 4.2). The ice edge is defined to be the southernmost surface cell with $E < E_m + 0.5L$.

The softer albedo reduction below the freezing point used in the DST2 albedo parametrization (Fig. 4.3a) results in convergence on the same asymptotic state of both initial conditions in the partially perennial ice regime. All simulations exhibit a fully ice covered asymptotic stable state for $\Delta b \leq -80$ W m^{-2}. For the OWIC the annual average ice edge latitude recedes gradually northwards for Δb between -80 and -45 W m^{-2}. Initially fully ice covered simulations remain in that state for $\Delta b \leq 57.8$ W m^{-2} and only converge to the same asymptotic state as OWIC simulations for greater Δb values. With rising Δb there is

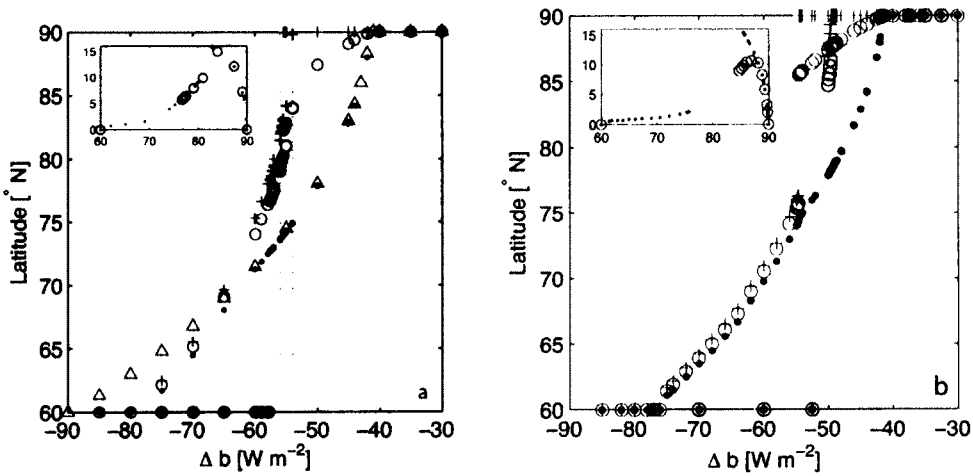

Figure 4.3. a: Ice edge latitude vs Δb for the DST2 albedo parameterization. Red symbols are used for open water initial condition (OWIC). Blue symbols are used for ice covered initial condition (ICIC). Circles are annual mean ice edge latitudes. Dots are annual southernmost ice edge latitudes. Plus signs are annual northernmost ice extents. Grey triangles show the annual average ice edge location for laterally uncoupled simulations with OWIC. Grey dotted lines: simulations used in Sec. 4.4. Inset: Difference of maximum (winter) ice edge latitude and minimum (summer) ice edge latitude $\Delta\theta_s$ vs. annual average ice edge latitude $< \theta_l >$. ICIC simulations between latitude 80 and 85° N are not converged after 170 years of real time at their mean ice edge location. Winter ice edges for those simulations have reached equilibrium.
b: Ice edge latitude vs Δb for the DST1 albedo parameterization. Simulations for the ICIC with average annual ice edge (blue circles) around latitude 85°N have not converged after 170 years of real-time simulation.
The OWIC starts all grid cells at $E = E_m + 1.5L$; The ICIC starts all grid cells at $E = E_m - L$. All simulations shown were run out to 170 years of real time (6×10^6 time steps) or to the point where the changes in all cells from one year to the next were less than a 10^{-15}th of the typical cell energies.

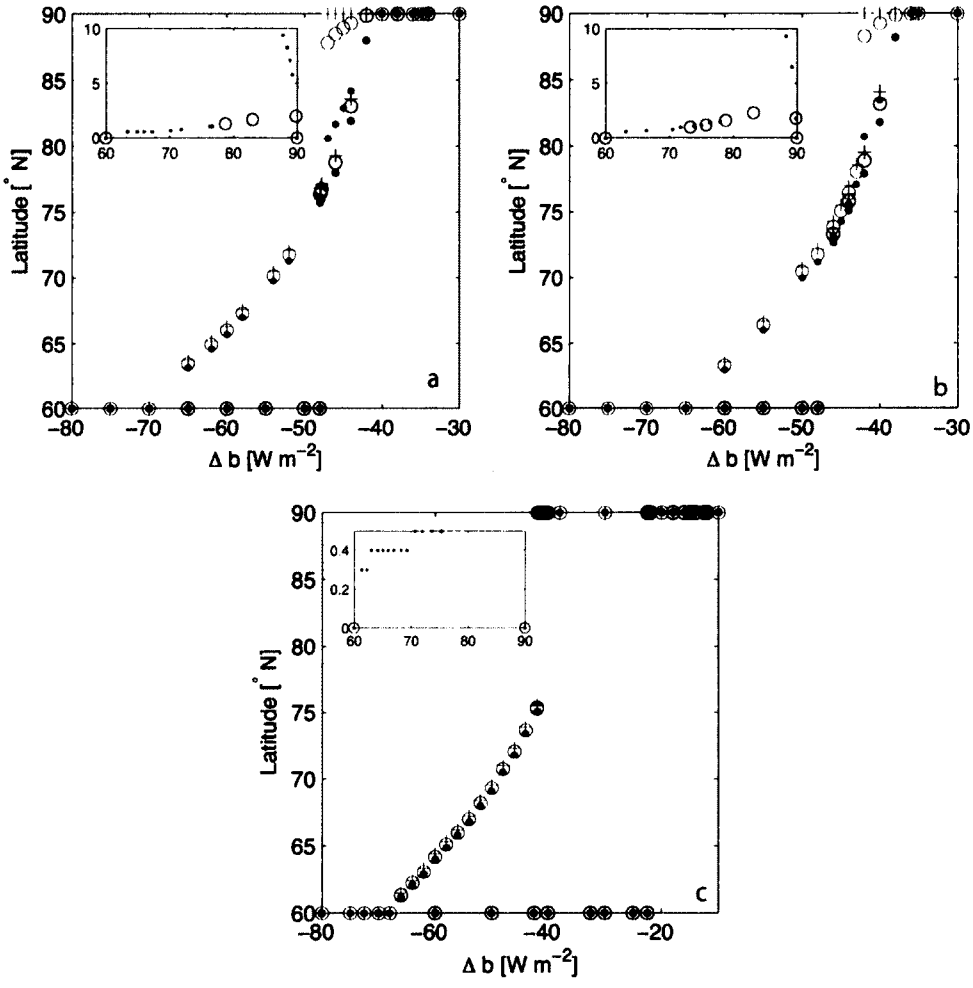

Figure 4.4. a: Ice edge latitude vs Δb for the LST albedo parameterization. Red symbols are used for OWIC. Blue symbols are used for ICIC. Circles are annual mean ice edge latitudes. Dots are annual southernmost ice edge latitudes. Plus signs are annual northernmost ice extents. Inset: Difference of maximum (winter) ice edge latitude and minimum (summer) ice edge latitude $\Delta\theta_s$ vs. annual average ice edge latitude $< \theta_I >$. Ice covered initial condition simulations between latitude 75 and 85° N are not converged after 170 years of real time.

b: Ice edge latitude vs Δb for the GLT albedo parameterization. Ice covered initial condition simulations between latitude 78 and 85° N not converged after 170 years of real time.

c: Ice edge latitude vs Δb for the SAT albedo parameterization.

a strong divergence between the winter maximum and the summer minimum ice extent. This divergence reaches a maximum of 10° (Fig. 4.3, inset) while there still is a perennial ice cover present at high latitudes. A small discontinuity in the average ice edge location is visible at $\Delta b = -55.5\ \mathrm{W\,m^{-2}}$ which marks the transition from perennial to seasonal ice cover. Convergence of simulations started in the ice covered state is very slow around the transition point. The winter ice extent converges much earlier to its asymptotic state than the summer ice extent. Tests with the ICIC, where a few cells (equivalent to less than 1 latitudinal degree) at the southern end of the grid are open water, show convergence to the same stable state as simulations with OWIC at the same forcing. This hints that the ICIC simulations that remain completely ice covered where OWIC simulations under the same forcing do not remain ice covered are a direct product of the closed boundary condition at latitude 60°N.

Simulations for DST2 and a *laterally uncoupled* model domain ($D^{(h)} = 0$ and $k_{\mathrm{eff}}/h_h = 0$) were performed to understand the importance of lateral fluxes for the asymptotic model behavior. The grey triangles in Fig. 4.3a show the annual average ice edge for the OWIC. The winter ice extent of the laterally coupled simulations coincides quite well with the annual average ice extent for the laterally uncoupled case for $\Delta b \geq -65\ \mathrm{W\,m^{-2}}$. Below $\Delta b = -65\ \mathrm{W\,m^{-2}}$ the coupled model predicts a greater ice extent than the uncoupled model. Tests for the fully coupled model with $\alpha_{I,\min} = 0.3$ and 0.5 show that the behavior seen in Fig. 4.3a is robust under a changed albedo step height with only minor shifts in the average ice edge latitude vs Δb. Simulations for a fully couple ice-ocean and $k_{\mathrm{eff}}/h_h \in \{0, 2.7, 27, 270\}\ \mathrm{W\,m^{-2}K^{-1}}$ show no appreciable change in model dynamics.

With the DST1 albedo parametrization (Fig. 4.3b) a perennial ice cover that covers less than the full latitudinal extent is only a stable state for simulations started with the OWIC for Δb between -75 and $-53\ \mathrm{W\,m^{-2}}$. If the forcing for these simulations is further increased, the annual average ice edge suddenly transitions about 9° northward and all ice melts during the summer months. The winter maximum remains at similar latitudes as those for adjacent simulations with a portion of perennial ice cover; the inset in Fig. 4.3b illustrates this regime change further. As the annual average ice edge recedes northward the difference between summer and winter ice extent slowly increases but remains well below 3°. The annual average ice edge moves sharply northwards for $\Delta b = -55\ \mathrm{W\,m^{-2}}$.

The difference between summer and winter extrema spikes to nearly 15° and then slowly reduces again as the winter extremum recedes further north with increased forcing. This spike coincides with the disappearance of all summer ice cover. For simulations initialized with complete ice cover we see the model grid remains perennially ice covered up to $\Delta b = -50$ W m^{-2}. For stronger forcing, the system approaches the same asymptotic state as for the OWIC, but convergence for the summer ice extent (blue plus signs) is extremely slow (> 170 years) for Δb between -50 and -49 W m^{-2}. The winter ice extents (blue dots) converge to their stable value relatively quickly (< 50 years). As for the DST2 albedo parametrization, the ICIC simulations maintain a closed ice cover where the OWIC do not, and are not stable under small perturbations. If perturbed by manually removing the ice cover in less than 1 latitudinal degree at the southern end of the model domain these simulations will converge to the same asymptotic state as the OWIC simulations under the same Δb.

Figures 4.4a and 4.4b show the ice edge latitude vs. Δb for the LST and GLT albedo parametrization, respectively. Their behavior is quite similar to each other with the exception that the GLT parametrization for the ICIC converges to a state exhibiting perennial ice at $\Delta b = -54$ W m^{-2}. At the same Δb, the LST parametrization with ICIC shows convergence to a seasonal ice state and no initially ice covered simulation converges to a state with perennial ice. The asymptotic states for LST albedo are shifted by -5 W m^{-2} in comparison to the GLT albedo. This can be attributed to the lowered albedo for open water at the freezing point for the LST albedo (Fig. 4.2a). As in the DST1 case the transition from perennial ice cover to seasonal ice cover is marked by a significant northward movement of the annual average ice edge location. For both albedo parametrizations, simulations started with ICIC are unstable under removal of a small area of ice at southern latitudes.

Using the SAT parametrization, only a perennial ice cover in parts of the Arctic or no ice cover at all are asymptotic stable states of the system (Fig. 4.4c) is found. When initialized with OWIC the system will remain in the open water state for $\Delta b > -42$ W m^{-2}. For lesser forcing ($\Delta b \leq -42$ W m^{-2}) the annual average ice edge location (Fig. 4.4a, red circles) transitions to latitude 75.4 N ($\Delta b = -42$ W m^{-2}) and then progresses southwards with reduced forcing, until it reaches the southernmost model latitude (60 N) at $\Delta b = -68$ W m^{-2}. Annual maximum (red dots) and minimum (red plus signs) ice edge locations remain within 0.5° of each other (Fig. 4.4c, inset). Thus, the region of seasonal ice is no larger than a band

of 0.5° width for any of these simulations. For simulations initialized with complete ice cover, the model domain remains perennially ice covered for forcing $\Delta b \leq -22.5\ \mathrm{W\ m^{-2}}$ and then moves to perennially ice free for larger forcing.

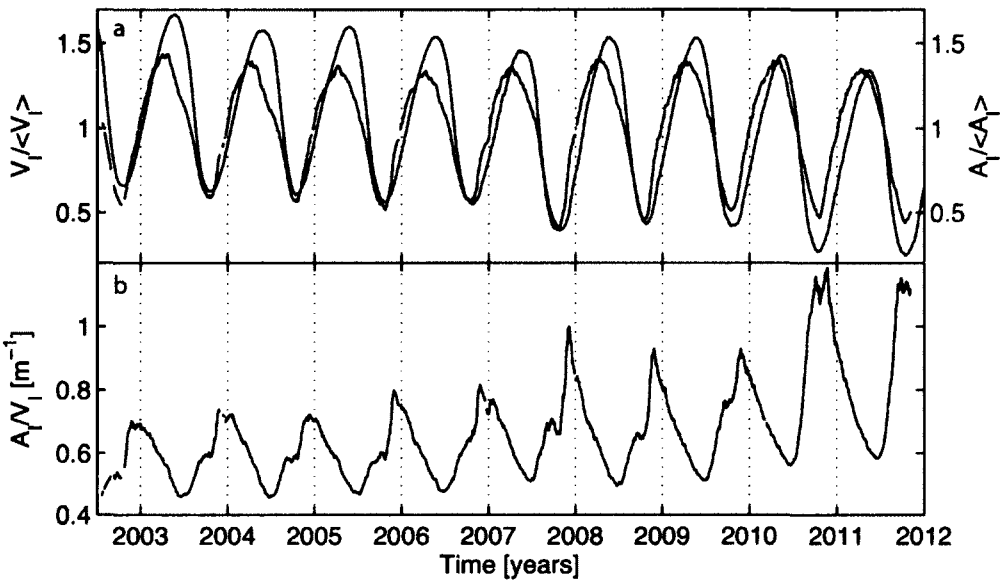

Figure 4.5. Ratio of ice extent over ice volume. a: Normalized ice extent (blue, right y-axis) and ice volume (black) data. b: Ratio of ice extent over ice volume. Extent data from (IARC-JAXA Information System, 2012); volume data from PIOMAS Polar Science Center, 2012 for June 1, 2002 to December 31, 2012. Vertical dotted lines denote year to year transition with the furthest left being the transition from 2002 to 2003. The ice extent data provided by the IARC-JAXA Information System, 2012 is derived from Advanced Microwave Scanning Radiometer for the Earth Observing System (AMSR-E) and the ice volume data provided by the Polar Science Center, 2012 is calculated using the Pan-Arctic Ice Ocean Modeling and Assimilation System (PIOMAS) and validated with observations from US-Navy submarines, oceanographic moorings, and satellites. Missing data points are due to gaps in the sea ice extent data record IARC-JAXA Information System, 2012.

4.4 Indicators of Change

Figure 4.3 illustrates that a receding ice cover coincides with amplified seasonal changes in ice extent. The winter ice extent shows little change in slope under increased forcing

Δb, while the summer ice extent changes sharply under the same change of forcing in the interval of $\Delta b \in [-60, -50]$ W m^{-2}.

Ice extent is an easily accessible measure for the Arctic, e.g., through satellite measurements, but it does not give accurate information about the sea ice volume. To understand how the amount of energy (sensible and latent heat) in the system changes, it is important to know how large the ice volume is and how it changes with forcing. Ice volume is derived from point measurements of the ice thickness via models. Pan-Arctic ice thickness estimates are only accessible via submarine studies or models using freeboard estimates from satellite data compiled into ice thickness distributions.

Under the assumption that the ice volume V_I depends, in the first order, on ice extent A_I as $V_I \propto A_I f(A_I, z, ...)$, with $f(A_I, z, ...)$ some non-trivial function of the ice area, thickness measurements and other factors. To gain better insight into higher order processes, it is beneficial to investigate the dynamics of the ratio of ice extent and volume, A_I/V_I. The advantage of using A_I/V_I, a measure inverse to thickness, is that this measure will enhance features of a thinning ice cover. The graphs in Figs. 4.5, 4.6a and c, and 4.7a and c show A_I/V_I for data based on measurements and for selected simulations. The finite resolution of our model puts a theoretical upper bound of 3.33 m^{-1} (thinnest possible ice resolved) on the ratio. Values smaller than 0.3 m^{-1} are the result of all ice being quite thick.

In Fig. 4.5 the ice extent (IARC-JAXA Information System, 2012), the ice volume (Polar Science Center, 2012) and their ratio A_I/V_I for the time from June 1, 2002 to December 31 2011 are shown. Missing data points are due to missing data in the ice extent record. Vertical dotted lines separate years, with the furthest left vertical separating 2002 from 2003. For reference, the three years of lowest ice extent since satellite measurements are (lowest on record first): 2007 , 2011 , and 2008 (IARC-JAXA Information System, 2012). The three years of lowest ice volume (lowest on record first) are: 2011, 2010 and 2007 (Polar Science Center, 2012).

The record in Fig. 4.5 shows a trend towards thinner ice. This manifests itself as higher peaks and a slight increase in annual average of A_I/V_I. The first three years of record are relatively stable; as the ice retreats in the spring A_I/V_I decreases to about 0.45. This is followed by the predominant loss of ice thickness increasing A_I/V_I to about 0.6. At this point both the ice extent and ice volume have reached their minimum values and the system re-

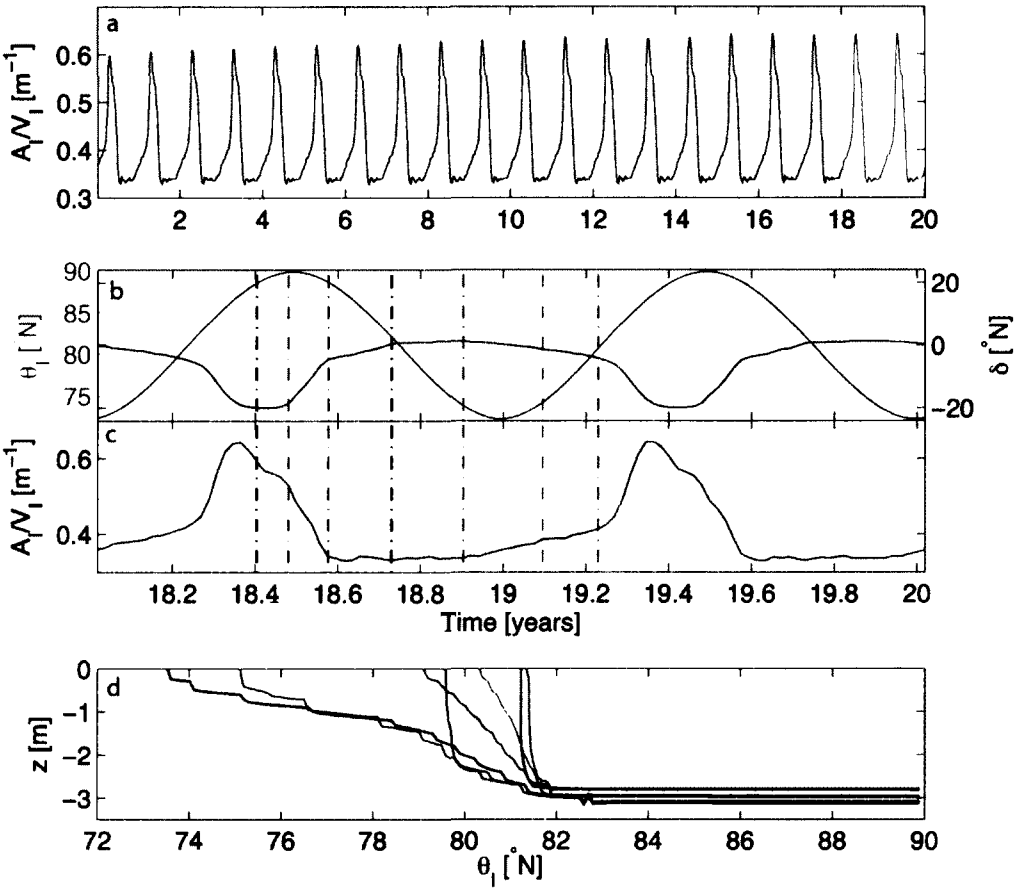

Figure 4.6. Ice thickness evolution for DST2 with $\Delta b = -56$ W m^{-2} and ICIC (see Fig. 4.3). This simulation is near convergence, with a stable perennial ice cover. (a) 20 year record of A_I/V_I over time starting with model year 50. The red part of the record is shown larger in (c). Note that the y-axis of (a) and (c) is of significantly different scale than in Figs. 4.5 and 4.7. (b) Ice edge latitude (red, left y-axis) over time. Vertical lines mark the times the ice thickness was sampled; colors correspond to graphs shown in (d). For reference the solar declination angle is shown (black, right y-axis). Positive values denote angles north of the equator. (c) A_I/V_I over time for model year 68 and 69. (d) Ice thickness over latitude at different times of year. Graph colors correspond to vertical lines in (b) and (c). The finite resolution of our model puts a theoretical upper bound of 3.33 m^{-1} (thinnest possible ice resolved) on A_I/V_I. Values smaller than 0.3 m^{-1} are the result of all ice being quite thick (> 3 m).

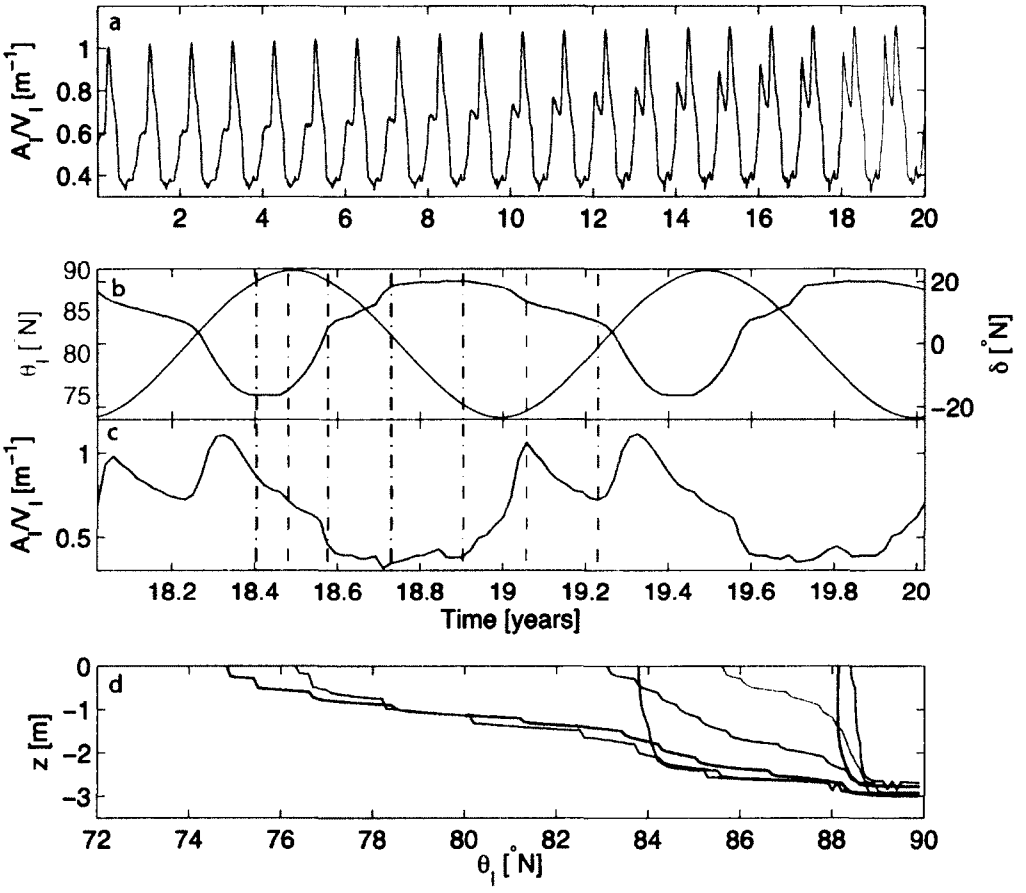

Figure 4.7. Ice thickness evolution for DST2 with $\Delta b = -54$ W m^{-2} and ICIC (see Fig. 4.3). The simulations maximum ice extent has arrived at its asymptotic state, minimum ice extent and ice volume have not converged at the data shown. The simulation will converge to a seasonal ice cover state. (a) 20 year record of A_I/V_I over time starting with model year 50. The red part of the record is shown larger in (c). (b) Ice edge latitude (red, left y-axis) over time. Vertical lines mark the times the ice thickness was sampled; colors correspond to graphs shown in (d). For reference the solar declination angle is shown (black, right y-axis). Positive values denote angles north of the equator. (c) A_I/V_I over time for model year 68 and 69. (d) Ice thickness over latitude at different times of year. Graph colors correspond to vertical lines in (b) and (c).

mains at this value for a few weeks. This is followed by a sharp increase in ice extent with little increase in volume, which causes A_I/V_I to peak at about 0.75 and then to decrease to about 0.6 as the newly grown ice increases in thickness. The slight change in slope during the decrease coincides with the onset of spring melt. The year 2006 shows similar behavior, where the double peak in early 2007 is due to an atypical temporary slowdown in ice extent increase. During the 2007 melt season, the ice extent and volume drop to levels significantly lower than previous years, which is indicated by the A_I/V_I minimum being much higher (0.5) than in previous years. This is again followed by a few weeks of little change when both ice volume and extent are around their minima. When the ice extent rebounds much thin ice is grown resulting in a much higher peak ($A_I/V_I \approx 1$) towards the end of 2007. In the following two years (2008 and 2009) the behavior is similar to 2007, with slightly less prominent peaks hinting at volume recovery. The year 2010 shows rapid decline and thinning of ice during the melt season. This is followed by a double peak. The first peak is generated near the minimum ice extent, which makes it similar in nature to the periods of little change at half peak height seen in earlier years. It is a signal of further thinning ice. The second peak is generated by the rapid growth of thin ice. The AMSR-E record ends on October 4, 2011 due to equipment malfunction (IARC-JAXA Information System, 2012), but not before the ice extent has reached its annual minimum. The last peak in A_I/V_I coincides with that minimum and is of similar nature to the first peak for 2010 and the periods of little change at half peak height in previous years.

The model trajectories shown in Figs. 4.6 and 4.7 consistently exhibit a 10 week delay for maximum and a 4 week delay for the minimum ice extent compared to the real world data. This is not surprising considering that the model is not coupled to lower latitudes which could supply additional lateral fluxes. In addition, in the AMRS-E record, pixels containing 15% ice are considered ice covered (IARC-JAXA Information System, 2012), whereas, this study only considers cells with 100% ice ($E \leq E_m + L/2$) as part of the ice cover. This can lead to further discrepancies between model data and satellite record.

Figure 4.6 shows A_I/V_I for a DST2 albedo parametrization simulation with ICIC and $\Delta b = -56$ W m^{-2}. This simulation will converge to an average ice edge location of 79°N and moderate oscillation of 7.8° between summer and winter (cf. Figs. 4.6b and4.3). For this parameter set, the ocean has a stable perennial ice cover at high latitudes and a significant

band of seasonal ice. The oscillation in A_I/V_I is of similar magnitude as the first three years in Fig. 4.5. As the ice edge recedes northward during summer, the average thickness of the remaining ice increases (Fig. 4.6d, black, red and green) to where $A_I/V_I \approx 0.35$. The melting process for this period is dominated by *retreat through thinning*, i.e., the ice thins first and then recedes. At the same time the ice cover at higher latitudes (78° to 81.5°N) is gaining thickness. Then there is a period of *laterally driven retreat* (Fig. 4.6d, green, blue and gray), i.e., thick ice melting from the side, during which the ice edge recedes by 1.8° and thickness of the remaining ice remains high. In late fall and winter, the ice edge moves southward (Fig. 4.6d, orange and magenta). Area and volume gains are at similar rates, resulting in only a slight increase in A_I/V_I to about 0.41. The feature of consolidation at half peak height seen in most of the record shown Fig. 4.5 is not present. Instead, the period of slow southward ice growth and thickness consolidation is seen as a wide region of near minimum values of $A_I/V_I \approx 0.35$ to 0.41. This is followed by the rapid advance of the ice edge back to winter maximum levels (Fig. 4.6d, black). During this period, the ice area increases faster than the ice volume resulting in the increase of A_I/V_I to its maximum of 0.64 during most rapid ice area increase. As the advance of the ice edge halts the system enters a short period of consolidation indicated by the reduction of peak height from 0.64 to 0.55. Further reduction of peak height is due to the ice edge receding rapidly northward.

To compare the 'fingerprint' of a stable perennial ice cover with that of a receding perennial ice cover, Fig. 4.7 shows data from a DST2 albedo parametrization simulation with ICIC and $\Delta b = -54$ W m^{-2}. This simulation will eventually reach a stable state without perennial ice. The part of the record shown exhibits a perpetually decreasing perennial ice cover around the pole, where the annual northernmost ice edge (summer minimum) recedes by 0.1° every year. The southernmost annual ice edge location (winter maximum) does not change. The ice edge oscillates by 13.6° within an annual cycle, an increase of 5.8° compared to the simulation shown in Fig. 4.6. The period of *retreat through thinning* (Fig. 4.6d, black, red to green) is temporally very similar to that observed in the previous simulation, but spans 9.0° instead of 6.1°. The overall ice thickness is reduced. Thickness gains are still observed at higher latitudes during initial melt, but the ice thickness does not recover to levels seen in Fig. 4.6d. During *laterally driven retreat* (Fig. 4.7d, green, blue, and gray) the ice edge recedes by 4.6°. This is over 2.5 times more than is observed in Fig. 4.6d

for the stable perennial ice cover.

The record shows the development of a shoulder/double peak as time progresses (Fig. 4.7a). Early peaks resemble those of the years 2007 to 2009 in Fig. 4.5; later ones are similar to those seen in 2010 and 2011. The double peak feature (Fig. 4.7c, gray to orange) begins to develop near minimum ice extent and is the result of rapid ice extent gains with negligible thickness gains. As the ice edge moves further south, the thickness of the ice is somewhat consolidated (Fig. 4.7d, magenta) resulting in the local minimum between the peaks. The second peak is the result of further rapid gains of thin ice with the maximum coinciding with maximum rate of advance of the ice edge.

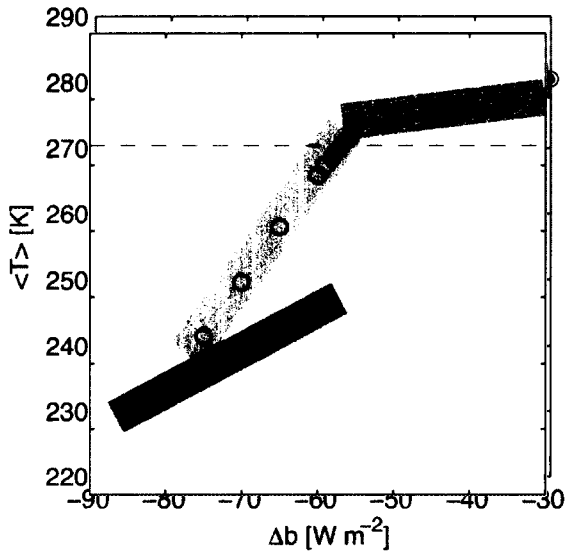

Figure 4.8. Spatiotemporal average surface temperature $< T >$ vs additional surface forcing Δb for the DST2 albedo parameterization. Regime R1 (shaded blue): closed ice cover, no ice albedo feedback; R2 (shaded red): seasonally varying ice cover with perennial ice at high latitudes; and R3 (shaded grey): seasonal ice cover/perennially open water. Red symbols signify open water initial condition. Blue symbols signify ice covered initial condition. The dashed grey line marks the freezing temperature. Values shown are for the last full seasonal cycle in a given simulation.

4.5 Surface Forcing Feedbacks

The presented model contains two directly accessible feedbacks, longwave and albedo feedback. The longwave radiative forcing and the albedo are functions of the surface cell energy. Surface cell temperature, as defined in Sec. 4.2, will be used here to perform a feedback analysis in analogy to the literature (Bony et al., 2006; Flanner et al., 2011). Note that the literature on feedbacks in GCMs usually assesses top of the atmosphere feedbacks. This is not practical in the described model as the atmosphere is a boundary condition, part of R_{LW} and not a fully modeled system.

The surface heating and the forcing feedbacks will be assessed based on spatiotemporal averages $< X >$ of the respective variables, where

$$< X >= \frac{1}{S} \sum_{k=1}^{S} \frac{\sum_{j=1}^{M} A_j X_j(t_k)}{\sum_{j=1}^{M} A_j}, \tag{4.12}$$

and where $X \in \{T, \alpha, \alpha R_{SW}^{\downarrow}, R_{LW.0}\}$ and S is the total number of time-steps for a seasonal cycle.

The spatiotemporal surface temperature average $< T >$ for albedo parametrization DST2 is shown as a function of Δb (Fig. 4.8). The average surface temperature increase with additional surface forcing can be numerically determined to be,

$$\frac{\partial < T >}{\partial \Delta b} = \begin{cases} 0.62 \frac{K}{\mathrm{W\,m^{-2}}} & \text{for R1,} \\ 1.57 \frac{K}{\mathrm{W\,m^{-2}}} & \text{for R2,} \\ 0.19 \frac{K}{\mathrm{W\,m^{-2}}} & \text{for R3.} \end{cases} \tag{4.13}$$

Three distinct regimes, in which $< T >$ changes linearly, can be identified (Fig. 4.8): (R1) heating under closed ice cover (shaded blue, blue dots between $\Delta b = -90$ and -57.8 W m^{-2}), (R2) heating under seasonally varying ice edge with stable perennial ice cover at high latitudes (shaded red, red circles between $\Delta b = -75$ and -55.5 W m^{-2}), (R3) heating under seasonal ice or open water (shaded grey, red circles, $\Delta b \geq -55.4$ W m^{-2}). The surface temperature exhibits a sudden increase of 0.8 K at the transition from R2 to R3. For the other albedo parametrizations (Sec. 4.2.1), the temperature increase in R2 is smaller, ranging from 1.14 $K(\mathrm{W\,m^{-2}})^{-1}$ (SAT) to 1.41 $K(\mathrm{W\,m^{-2}})^{-1}$ (DST1). The sudden temperature increase at the transition from R2 to R3 is significantly larger for all other albedo parametrizations, ranging from 2.8 K (GLT) to 5.3 K (DST1).

Spatiotemporal average surface forcing $< R_{net} >$ is [Eq. (4.8) and Eq. (4.9)],

$$< R_{net} >=< R^{\downarrow}_{SW} > - < \alpha R^{\downarrow}_{SW} > + < R_{LW,0} > + \Delta b, \tag{4.14}$$

with $R^{\downarrow}_{SW} = S_0 \cos\psi(\theta)[\tau^m + 0.3(1-\tau^m)]$ (cf. Eq. 4.9) the down-welling shortwave radiation, and $< R_{LW} >=< R_{LW,0} > + \Delta b$ for clarity.

The spatiotemporal average surface forcing changes with $< T >$ and $< \Delta b >$ according to,

$$d < R_{net} >= \frac{\partial < R_{net} >}{\partial < T >} d < T > + \frac{\partial < R_{net} >}{\partial \Delta b} d\Delta b. \tag{4.15}$$

This defines the individual feedback parameters to be,

$$d < R_{net} >= (\lambda_\alpha + \lambda_{LW}) d < T > + \frac{\partial < R_{net} >}{\partial \Delta b} d\Delta b, \tag{4.16}$$

with,

$$\lambda_\alpha = -\frac{\partial < \alpha R^{\downarrow}_{SW} >}{\partial < T >}, \tag{4.17}$$

$$\lambda_{LW} = \frac{\partial < R_{LW,0} >}{\partial < T >}, \tag{4.18}$$

with λ_α and λ_{LW} the individual feedback parameters for albedo and longwave radiative feedback respectively (cf. Bony et al., 2006). For the temperature range experienced by the model simulations λ_{LW} is nearly constant, with -1.33 W m^{-2}K^{-1} (Fig. 4.9a).

The albedo feedback parameter changes significantly through the three regimes (Fig. 4.8). In R1, λ_α is virtually zero and in R3 λ_α transitions back to virtually zero with the diminishing seasonal ice cover. In R2, the albedo feedback can be approximated to be linear, with $\lambda_\alpha = 2.35$ W m^{-2}K^{-1} (Fig. 4.9b). Comparison between the behavior of $< \alpha R^{\downarrow}_{SW} >$ and $< \alpha >$ as functions of $< T >$ (Fig. 4.9b and c) shows that the change in λ_α is mainly due to changes in the albedo. For the other albedo parametrizations the albedo feedback parameter lies between 2.22 W m^{-2}K^{-1} (GLT) and 2.59 W m^{-2}K^{-1} (LST).

The albedo feedback in R2 for the laterally uncoupled model with DST2 albedo parametrization (see Fig. 4.3a, grey triangles) is significantly lower with $\lambda_\alpha = 2.00$ W m^{-2}K^{-1}. For these simulations with no lateral coupling the warming with increased forcing in R2 is reduced to 1.00 K(W m^{-2})$^{-1}$ as well.

The albedo feedback plays a significant role in the enhanced warming in R2. Following Myhre et al., 1998, CO_2-doubling causes a forcing increase of $5.35 \cdot \ln 2 = 3.71$ W m^{-2}, which

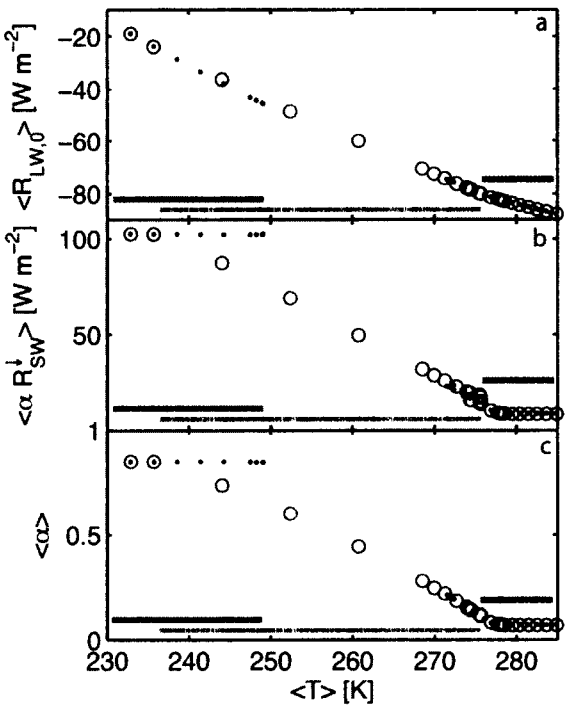

Figure 4.9. Feedbacks. a: Spatiotemporal average of the longwave radiation $< R_{LW,0} >$ versus $< T >$ for simulations with DST2 albedo parametrizations. Red circles signify simulations with OWIC; blue dots signify simulations with ICIC. Colored bars correspond to the temperature intervals of the regimes introduced in Fig. 4.8. Values shown are for the last full seasonal cycle in a given simulation. b: Spatiotemporal average of reflected shortwave radiation $< \alpha R^{\downarrow}_{SW} >$ versus $< T >$. c: Spatiotemporal average albedo $< \alpha >$ vs $< T >$.

would result in a temperature increase of 5.82 K for this model in the R2 regime (Eq. 4.13). The same forcing increase without ice albedo feedback (R1) would result in a temperature increase of 2.30 K. Thus, the ice albedo feedback amplifies the temperature increase in the Arctic by 3.52 K. Vice versa, if CO_2 is reduced to half in R3 (ice-free ocean), the surface would cool by 0.70 K and would continue to do so into R2 if no ice albedo feedback were present. With ice albedo feedback, under this scenario, cooling is enhanced by 5.12 K. The difference between enhancement of temperature changes in R1 (fully ice covered) and R3 (ice-free) is a direct result of difference in albedo and the difference in specific heat capacity of ice and water. R1 is a model specific state and only exists due to the closed southern boundary in the model. It would only be realized for a fully ice covered globe, since the albedo feedback in R2 is not dependent on the location of the ice edge. The value of λ_α refers to the spatial extent of the model only, latitude 60 to 90 °N. Feedbacks reported in the literature are usually reported for the entire Earth or the Northern Hemisphere, even if their direct effect is localized. A first estimate the albedo feedback parameter for the entire Northern hemisphere, with an ice edge within the modeled latitudes, can be gained by $\lambda_{\alpha.NH} = \lambda_\alpha A_A / A_{NH} = 0.32$ W m^{-2}K^{-1}, with A_A the total area of the model domain and A_{NH} the total area of the Northern hemisphere.

4.6 Conclusion

A regular network model for energy flow and phase transition in an ocean mixed layer is presented. It incorporates two spatial dimensions that resolve the latitudinal extent of the Arctic region horizontally and the ocean mixed layer vertically. The ocean mixed layer is coupled to a constant temperature ocean below and forced by radiative fluxes at the interface with the atmosphere. An additional atmospheric forcing term acts as a bifurcation parameter to simulate warming and cooling. Albedo parametrizations range from a double step parametrization fitting measurements quite well to a sharp single step parametrization giving a low order fit to measurements and routinely used in Thorndike, 1992; Eisenman and Wettlaufer, 2009; Müller-Stoffels and Wackerbauer, 2011; Müller-Stoffels and Wackerbauer, 2012. The model is a significant extension of work presented in Müller-Stoffels and Wackerbauer, 2011 and Müller-Stoffels and Wackerbauer, 2012.

Asymptotic states of the ice ocean layer include a stable perennial ice cover at northern

latitudes, a region of seasonal ice at mid-latitudes and open water at southern latitudes. The model converges to a perennially stable ice cover under very low forcing and to open water at all latitudes at very high forcing regardless of albedo parametrization. The albedo parametrizations that fit measurements better produce a stable state of seasonal ice cover at high latitudes. The model exhibits a state of perennial/seasonal ice cover, with perennial open water at southern latitudes for a wide range of the bifurcation parameter. A state of perennial ice cover at all latitudes within that bifurcation parameter range is sensitive to perturbations, which suggests that it is a model artifact resulting from a closed boundary condition at the southern model boundary. It is speculated that a model with latitudinal extent from 90 °S to 90 °N could exhibit bistability, where one of the stable states is perennial ice cover at all latitudes under very low forcing (snowball earth scenario, Budyko, 1969). Further studies, with full latitudinal model extent, would be needed to address the sensitivity of such a state to perturbations, e.g., in form of small regions of open water.

An abrupt transition in summer ice extent from stable perennial ice to open water is a direct effect of enhanced lateral heat fluxes due to ice-albedo feedback resulting in laterally driven retreat of thick ice. The winter ice extent transition towards perennially open water is smooth for double step albedo parametrizations, but is discontinuous for sharp step-like and intermediate albedo parametrizations. The results for a laterally uncoupled model grid coincide (summer and winter ice extent) with the winter ice extent of the fully laterally coupled model for moderate to high additional surface forcing demonstrating the importance of lateral fluxes for summer ice melt. Ice albedo feedback together with lateral heat fluxes works in reverse below a given forcing threshold. For this low additional surface forcing the uncoupled model exhibits less ice than the coupled model.

The dynamics of an inverse ice thickness measure show a regime change between simulations with perennially stable ice cover and simulations with retreat ing perennial ice cover and corroborate the importance of lateral heat fluxes in the melting of thick ice at high latitudes. In simulations exhibiting a thick perennial ice cover at high latitudes the main mechanism of ice melt is *retreat through thinning*, i.e., the summer northward movement of the ice edge is preceded by a thinning of the ice cover. Simulations with seasonal ice cover as their asymptotic stable state exhibit the same *retreat through thinning* process

for much of their seasonal ice, but towards the end of the melt season large areas of ice retreat through a *laterally driven retreat* process in which thick ice melts from the side without thinning appreciably prior to that. Comparison with an inverse thickness measure derived from satellite (ice area, IARC-JAXA Information System, 2012) and model (ice volume, Polar Science Center, 2012) data suggests that a similar mechanism is responsible for the recent record low September ice volumes in the Arctic.

The ice albedo feedback consists of two mechanisms: (i) locally, when the ice cover disappears, the ocean is heated and increased cooling is needed to again form ice, and (ii) laterally, when an area of open water is adjacent to ice the larger rate of shortwave energy absorption of open water establishes an energy gradient, which leads to laterally driven retreat of more ice. The ice albedo feedback amplifies warming in all simulations and the magnitude of the feedback extrapolated for the Northern Hemisphere is within the range of measurements (Flanner et al., 2011) and GCM results (Bony et al., 2006). Control simulations with a laterally uncoupled model show that the impact of the ice albedo feedback is directly dependent on the existence of lateral heat fluxes. The first mechanism is solely a function of the local albedo difference between ice and open water. The second mechanism is a function of the ability of the ocean mixed layer to transport heat laterally. It is known from spatially confined studies (Müller-Stoffels and Wackerbauer, 2011; Müller-Stoffels and Wackerbauer, 2012) that the ice-ocean system in this model is locally bistable, i.e., a locally perennially ice covered ocean can be perturbed to transition to seasonal ice or open water. Lateral heat fluxes due to ice albedo feedback can supply the required perturbation. It can be expected that ice albedo feedback is more effective in regions where prevalent surface currents in the ocean move water towards the ice edge. Further studies on anisotropic lateral heat fluxes are needed to fully understand the influence of near surface ocean currents in this model. If the surface forcing in a laterally coupled model is reduced the ice albedo feedback is negative. Open water has a much higher (eddy) thermal diffusivity than ice which enhances cooling during the times of year when the surface forcing over open water is negative. This leads to the advance of a thin layer of ice, which now acts as the perturbation locally inducing the transition from an open water stable state to an ice covered/seasonal ice stable state. The next time the surface forcing is positive this layer of ice needs to be melted before the ocean can take up large amounts of heat again.

Enhanced vertical oceanic heat fluxes (increased E_{N+1}) have been observed to cause a thinning of average ice thickness in this model, but since the vertical eddy thermal diffusivity is seven orders of magnitude smaller than the horizontal eddy thermal diffusivity, they are suspected to play small roles in the observed lateral dynamics of the ice edge.

The albedo parametrizations with a transition interval of similar width to those used in this study have been shown to produce bistability in a spatially confined model (Müller-Stoffels and Wackerbauer, 2012). A spatial scaling argument was given showing that softer albedo transitions are suitable if large spatial extents are considered in low order models. The theoretical argument given in Müller-Stoffels and Wackerbauer, 2012 is corroborated by model results shown here. Furthermore, it has been shown that the spatial average of the albedo as a function of the spatial average of the surface temperature is not unique. This suggests that albedo parametrizations may have to fulfill further requirements if the model results are to be interpreted in a large spatial extent context.

The asymptotic model behavior is sensitive to changes in the albedo parametrization. This implies that further efforts are necessary to improve albedo parametrizations based on measurements for all modeling approaches to study the Arctic climate under forcing. Here it has been shown, that the ice albedo feedbacks intensity is directly linked to the amount of lateral heat flux allowed in the model. Interaction between ice albedo feedback and other system components, e.g., clouds and water vapor, is likely. Further study of such phenomena is necessary to understand higher order influences on the stability of the Arctic sea ice cover. The small number of components included in the model presented here makes it an ideal testbed to study isolated feedbacks and allows to easily keep track of cause and effect of parameter changes.

Acknowledgements

MMS has been supported by a UAF Graduate School thesis completion grant.

References

Abbot, D, M Silver, and R Pierrehumbert (2011). "Bifurcations leading to summer arctic sea ice loss". In: *Journal of Geophysical Research* 116, p. D19120. DOI: doi:10.1029/2011JD015653.

Andreas, E., C. Fairall, P. Guest, and O. Persson (1998). *SHEBA ASFG PAM surface temperature data*. URL: http://www.eol.ucar.edu/projects/sheba/.

ARM Data Archive (2010). URL: http://www.archive.arm.gov.

Armour, K, I Eisenman, E Blanchard-Wrigglesworth, K McCusker, and C Bitz (2011). "The reversibility of sea ice loss in a state-of-the-art climate model". In: *Geophysical Research Letters* 38.16.

Bony, S, R Colman, V Kattsov, R Allan, C Bretherton, J Dufresne, A Hall, S Hallegate, M Holland, W Ingram, D Randall, B Soden, G Tselioudis, and M Webb (Aug. 2006). "How well do we understand and evaluate climate change feedback processes?" In: *Journal of Climate* 19, pp. 3445–3482.

Budyko, M (1969). "The effect of solar radiation variations on the cliate of the Earth". In: *Tellus* 21.5, pp. 611–619.

Campbell and J Norman (1998). *Introduction to environmental biophysics*. Second. New York, NY: Springer Science+Business Media.

Eisenman, I (2012). "Factors controlling the bifurcation structure of sea ice retreat". In: *Journal of Geophysical Research* 117.D1.

Eisenman, I, N Untersteiner, and J Wettlaufer (May 2007). "On the reliability of simulated Arctic sea ice in global climate models". In: *Geophysical Research Letters* 34.10, pp. 1–4.

Eisenman, I and J Wettlaufer (Jan. 2009). "Nonlinear threshold behavior during the loss of Arctic sea ice". In: *PNAS* 106.1, pp. 28–32.

Flanner, M, K Shell, M Barlage, D Perovich, and M Tschudi (2011). "Radiative forcing and albedo feedback from the Northern Hemisphere cryosphere between 1979 and 2008". In: *Nature Geoscience* 4, pp. 151–155.

IARC-JAXA Information System (2012). *Data of Sea Ice Extent*. URL: http://www.ijis.iarc.uaf.edu/en/home/seaice_extent.htm (visited on 2012).

IPCC (2007). *Climate Change 2007: The physical science basis, summary for policymakers*. Tech. rep. Intergovernmental Panel on Climate Change.

Lenton, T, H Held, E Kriegler, J Hall, W Lucht, and H Schellnhuber (2008). "Tipping elements in the Earth's climate system". In: *PNAS* 105, pp. 1786–1793.

Müller-Stoffels, M and R Wackerbauer (2011). "Regular network model for the sea ice-albedo feedback in the Arctic". In: *Chaos* 21.1.

Müller-Stoffels, M and R Wackerbauer (2012). "Albedo parametrization and reversibility of sea ice decay". In: *Nonlinear Processes in Geophysics*.

Myhre, G, E Highwood, K Shine, and F Stordal (1998). "New estimates of radiative forcing due to well mixed greenhouse gases". In: *Geophysical Research Letters* 25.14, pp. 2712–2718.

North, G (1984). "Small Ice Cap Instability in Diffusive Climate Models". In: *Journal of the Atmospheric Sciences* 41.23, pp. 3390–3395. ISSN: 1520-0469.

Notz, D (Dec. 2009). "The future of ice sheets and sea ice: Between reversible retreat and unstoppable loss". In: *PNAS* 106.49, pp. 20590–20595.

Paulson, C (1998). *SHEBA ice camp summer leads albedo data*. URL: http://www.eol.ucar.edu/projects/sheba/.

Perovich, D (1998). *SHEBA spectral light transmittance project data*. URL: http://www.eol.ucar.edu/projects/sheba/.

Polar Science Center (2012). *Arctic sea ice volume anomaly, version 2*. URL: http://psc.apl.washington.edu/wordpress/research/projects/arctic-sea-ice-volume-anomaly/ (visited on 2012).

Sellers, W (1969). "A global climatic model based on the energy balance of the Earth-atmosphere system". In: *Journal of Applied Meteorology* 8, pp. 392–400.

Steward, R (2005). *Introduction to physical oceanography*. URL: http://oceanworld.tamu.edu/resources/ocng_textbook/contents.html.

Stroeve, J, M Holland, W Meier, T Scambos, and M Serreze (2007). "Arctic sea ice decline: Faster than forecast". In: *Geophysical Research Letters* 34, p. L09501. DOI: doi:10.1029/2007GL029703,2007.

Thorndike, A (June 1992). "A toy model linking atmospheric and thermal radiation and sea ice growth". In: *Journal of Geophysical Research* 97.C6, pp. 9401–9410.

Walker, G (2006). "The tipping point of the iceberg". In: *Nature* 441, p. 802.

Winton, M (2008). "Sea-ice albedo feedback and nonlinear Arctic climate change". In: *Arctic sea ice decline: observations, projections, mechanisms, and implications*. Ed. by C. M. Bitz E. T. DeWeaver and L. B. Tremblay. American Geophysical Union, pp. 111–131.

Chapter 5
Discussion and Conclusion

A new regular network model was developed to study ice albedo feedback, and reversibility of sea ice retreat. Results presented in Chapters 2 to 4 show that reversibility of sea ice retreat is sensitive to albedo parametrization and model extent (local vs regional). Explanations for these sensitivities are offered through surface energy balance fixed point studies, mapping of parameter space, and assessment of ice albedo feedback under varying lateral heat flux conditions.

General remarks: A new model approach to study a forced binary phase system has been presented. The regular network model describes an ocean mixed layer as a local (laterally homogeneous) and regional (laterally heterogeneous) grid. The surface energy drive has been developed based on underlying physics and local measurements where available. Care has been taken to develop time-independent parametrizations wherever possible, to ensure model performance would not be compromised when the model was run at parameter settings outside the currently known envelope for seasonal oscillations.

The model is energy based although temperature is the most readily available measurement for the real-world system. Energy is an extensive property, while temperature is an intensive property. Temperature is a very good proxy for the state of a climate system as long as this system does not undergo a phase transition. At the phase transition, large amounts of heat are converted from sensible to latent and vice versa at constant temperature. Thus, the temperature does not resolve the phase transition and by itself cannot give information about the phase state of the system at the freezing point. This problem is not so much a mathematical one, since sets of equations describing phase transitions are readily available; it is more a problem of interpretation of surface properties of sea ice, e.g., snow or melt pond covered sea ice can be at the same temperature, but they would have a very different albedo. Thus, the albedo of an ice cover cannot be uniquely resolved as a function of temperature. In contrast, the albedo as a function of energy allows to resolve physics at the melting point. Temperature is used throughout this study to put results into context with measurements and the literature. The model itself does not rely on temperature for internal calculations.

The model is scalable in spatial and temporal resolution as long as their interaction is

taken into account, i.e., coarser spatial resolution requires higher temporal resolution. The model resolution can be adjusted for many research questions, and a high vertical resolution (sub-meter scale) to resolve a growing ice cover can be set, while horizontal resolution (kilometer scale) is set to have the grid span the entire Arctic region. The horizontal resolution for the regional scale model, latitude 60°N to 90°N, might seem coarse, but it is much finer (by a factor of 4 to 6) than the resolution of state-of-the-art GCMs. With the resolution used in Chapter 4, 170 years of real-time can be modeled in 24 h on a single standard CPU core. With sufficient computational power it is possible to further increase the resolution and spatial scale.

The appeal of high horizontal resolution is that one can be sufficiently confident that parametrizations derived from local measurements can be ported to the model without spatial scaling and statistical models. This model feature allows a more intuitive approach to parametrization, reduces uncertainty regarding correct spatial scaling, and the effects of local physics are easily accessible in a regionally coupled model. This approach does not solve the problems due to lack of local measurements, e.g., high resolution, long term radiative forcing data is only available from the Atmospheric Radiation Measurement (*ARM Data Archive* 2010) site in Barrow, AK and extrapolation of single site local measurements to different locations introduces its own uncertainty.

The value of the scalable model approach becomes clear when one considers that low order models (Thorndike, 1992; Eisenman and Wettlaufer, 2009; Notz, 2009; Eisenman, 2012) consistently produce a region of bistability and generally predict that sea ice loss is irreversible, while results from state-of-the-art GCMs do not exhibit irreversible sea ice loss (Armour et al., 2011). Intermediate energy balance models (EBMs) have been employed to study ice albedo effects as well (Sellers, 1969; North, 1984; Shine and Henderson-Sellers, 1985; Winton, 2008), but most of these lack temporal resolution. Comparison of model results is complicated because of inter-model differences. With the model presented here it is possible to first understand local effects and then to scale-up the model to study how coupled local models interact. The power of the approach lies in the fact that the inter-model differences are negligible in this case and arbitrarily many intermediate scaling steps can be taken.

The definition of seasonal ice differs significantly between models with (GCMs and

EBMs) and without (ODE models) explicit horizontal spatial dimension. In ODE models seasonal ice is a state where *all* ice melts for at least one day of the year. In GCMs and EBMs, seasonal ice is ice that melts at some point during the seasonal cycle; this seasonal ice can coexist with perennial ice and open water at other latitudes, or it can be the only ice present in the model. Awareness of this difference is important when interpreting model results.

The popular literature likes to refer to a *tipping point* for the Arctic sea ice cover (e.g., Walker, 2006). Scientifically, the term tipping point is rather ill-defined and can mean either any transition from one stable state to another, or an *irreversible* transition from one stable state to another. In addition, it is a rather loaded term, associated with some sort of catastrophic failure. For these reasons this work describes model behavior in well defined terms such as bistability, hysteresis and bifurcation (Strogatz, 1994).

Local ice albedo feedback effects: In Chapters 2 and 3 a spatially confined (local) version of the regular network model is employed to study the effects of ice albedo feedback on the asymptotic behavior of the upper ice ocean layer. Only radiative surface and oceanic forcing was included; all other boundaries were closed. Longwave and shortwave radiative surface forcing are the strongest drivers of the surface energy balance, each being of the same order of magnitude and an order of magnitude larger than any other surface forcing effect (Thomas and Dieckmann, 2003). Only the shortwave forcing is directly linked to the albedo feedback, but both surface albedo and longwave forcing are functions of temperature; since the longwave forcing is of the same order of magnitude as the shortwave forcing it has to be included.

Investigation of the literature on low order models regarding the existence of a region of bistability identified a single significant difference between models producing a bistable regime (Thorndike, 1992; Eisenman and Wettlaufer, 2009) and those producing only a single stable state (Notz, 2009). This difference was found to be the sharpness at which the albedo value changes at the transition from ice to water. Models exhibiting bistability employed a sharp step-like albedo transition centered around the freezing point. Models exhibiting only one stable state over the entire additional surface forcing regime employed a much softer albedo transition with the decay in albedo beginning well in the freezing regime and reaching open water albedo values at temperatures well above freezing. To

conclusively clarify wether the shape of the albedo parametrization was the deciding factor in the existence of bistability the regular network model was run using several albedo parametrizations between a sharp step-like transition and a very wide linear transition (Ch. 3). Thus, inter-model differences were ruled out as contributing factors to the existence of bistability; it was shown that a softening of the step-like feature in the albedo parametrization towards a wide linear albedo transition indeed reduced and, with the widening of the transition, eliminated the existence of bistability. This finding, recently supported by Abbot, Silver, and Pierrehumbert, 2011; Eisenman, 2012, begs the question as to which form of albedo parametrization to use. The albedo measurements from SHEBA (Perovich, 1998; Paulson, 1998; Andreas et al., 1998) used in this study to motivate albedo parametrizations require differing interpretations depending on the model they are used for. For low order models and the spatially confined model presented (Ch. 2 and 3) the data may be interpreted as many single measurements of albedo correlated to near surface air temperature. Multiple different measurements at the same temperature generate a scatter of data a that temperature. The scatter is due to the fact that the near surface air temperature is not a direct measure of the local surface temperature where the measurement occurred. Through a spatial scaling argument it was shown that the step-like albedo parametrization motivated by local measurements can be directly connected to a smooth albedo transition for large regions. This leads to the conclusion that in models studying local effects or having high spatial resolution, sharp step-like albedo parametrizations are a suitable choice. In models studying regional effects without explicit or very coarse spatial resolution, spatially scaled albedo parametrizations are better suited. For models with explicit regional spatial extent the interpretation of the SHEBA albedo data in context of it being taken along a transect becomes more important. For regional scale models (Ch. 4) and GCMs, sub-grid size processes are parametrized in two ways: (i) a parametrization has to yield a relationship of a dependent variable (albedo) to the state variable (energy, enthalpy, temperature) of a model, and (ii) needs to describe the effect that sub-grid size heterogeneities of the dependent variable have on the value used at the grid size level. The standard deviation of mean albedo values measured along a transect increases with temperature, particularly between -5 °C and 0 °C. This increase of standard deviation is a direct result of surface heterogeneities due to surface melt (puddles and melt ponds).

If these surface melt heterogeneities are of sub-grid size for a particular model they have to be incorporated into the parametrization via a spatial argument. For the regional scale model this was done by introducing a second step in the albedo parametrization describing the drop of the albedo in the -5 °C to 0 °C temperature band. Through this second step it is acknowledged that the albedo data shown already represents a spatial average (average of measurements along a transect), although it would be desirable to have data from a transect of similar order of magnitude as the model resolution.

The spatially confined model with sharp albedo transition exhibits a region of bistability under additional surface forcing. The stable states are a perennial ice cover, and a seasonal ice or perennial open water state. The seasonal ice stable state is a special case of the open water stable state. The existence of seasonal ice depends directly on the shape of the longwave radiative forcing. The parametrization of longwave forcing used in Ch. 2 does not produce a stable seasonal ice state. Adjustments made to the longwave forcing parametrization based on measurements in Barrow, AK (*ARM Data Archive* 2010) allow for seasonal ice stable states (Ch. 3).

The surface forcing exhibits either one or two stable instantaneous fixed points depending on the magnitude of additional atmospheric forcing. Fixed points are called instantaneous as their existence and location varies throughout the seasonal cycle. For very low and very high additional surface forcing only a single fixed point exists throughout the seasonal cycle. For low additional surface forcing this fixed point is located in the ice covered energy regime. For high additional surface forcing the fixed point is located in the open water energy regime. Cell energies track these instantaneous fixed points but, due to thermal mass, do not reach them; rather, they circle the annual average location of the instantaneous fixed points. For a seasonal ice or open water stable state to exist, the open water instantaneous fixed point must exist for a minimum critical time during the seasonal cycle.

Regional scale ice albedo effects: The regional scale regular network model spans from latitude 60° N to 90° N (Ch. 4). The vertical resolution and the depth of the ocean mixed layer warrant to account for mechanical heat transfer mechanisms in the ocean via horizontal and vertical eddy diffusivities. The shortwave radiative forcing is spatially heterogeneous. Relatively sharp step-like albedo parametrizations were used with this model.

To match observed albedo data more closely, a second step just below the freezing point was introduced in several albedo parametrizations to model the decline of the ice albedo at near-freezing temperatures.

The regional model exhibits a parameter interval of bistability with perennial ice cover at all latitudes and seasonal ice or open water. However, the perennial ice at all latitudes stable state is a model artifact linked to closed boundary conditions at the southern end of the model grid; this state is very sensitive to perturbations. Thus, the regional model is not bistable in the sense that the local model is.

The model exhibits the same general behavior under all albedo parametrizations used: a receding ice cover under increased forcing and eventual transition to perennially open water. The mode of ice retreat, the amount of seasonal ice, and the existence of a seasonal ice cover at the pole are sensitive to the particular albedo parametrization. Under all albedo parametrizations, a sudden transition of the summer ice cover from perennial ice to open water is observed. The behavior of the winter ice extent under increased additional forcing depends strongly on the albedo parametrization with both continuous and discontinuous behavior at the point where the summer ice extent transitions to open water. These findings, in conjunction with the findings on sensitivity to albedo parametrization in the local scale model (Ch. 3), suggests that it is of great importance to develop very accurate albedo parametrizations for models meant for climate forecasting (GCMs). This evidence is corroborated by findings in Eisenman, Untersteiner, and Wettlaufer, 2007 that ice extent predictions in GCMs are sensitive to small changes in ice albedo values.

The regional model can be understood as coupled local models. Each of the local models would exhibit a parameter region of bistability if isolated. This region of bistability would be different for each local model depending on its latitudinal location. When these local models are laterally coupled their interaction can be interpreted as perturbation of their respective stable states. If an ice covered latitudinal location has an open water neighbor, lateral heat fluxes during summer months will be large due to ice albedo feedback. This large perturbation can push the ice covered latitudinal location into a seasonal ice state or an open water state. If this is the case, the perturbation is now largest between the newly ice free latitudinal cell and its northern neighbor and the same process can repeat. By this cascading mechanism, the summer ice edge can move significantly further North

than local surface energy budgets would allow. Thus, the lateral heat transfer increases the ice albedo feedback and is an important part of the feedback mechanism. This finding is congruent with the finding that a laterally uncoupled regional model produces stable states consistent with the winter ice extents of the coupled model and the distinctly different melt regimes found in this study. The two melt regimes identified are *melt trough thinning* and *lateral melt*. It is speculated that the model latitudes that predominantly experience melt through thinning are located in a region where the surface forcing is strong enough to directly melt much of the ice cover in the summer; the model latitudes with predominant lateral melt are located in a region where the surface forcing alone is insufficient to melt significant amounts of ice. The two melt regimes overlap which makes an in-depth study of heat fluxes and local forcing within the laterally coupled regional model necessary to gain full understanding of the mechanisms observed.

Much of the analysis of the regional model was done using spatial and spatiotemporal averages. This revealed that variables such as spatially averaged temperature and albedo are not unique functions of spatially averaged energy. It can be concluded that this non-unique behavior would complicate any spatial averaging scheme employed in low order models (without horizontal spatial dimension) that are meant to study the behavior of a large region under forcing.

Outlook The behavior of the regular network model presented in this study is well understood, both for spatially confined and regional scale modeling. The model was designed to study isolated feedbacks in a controlled and systematic way. The shortwave and longwave forcing components follow physical principles and local measurements, and with the coupling of the ocean mixed layer to a constant temperature ocean, model outputs such as temperature and ice thickness, fall within geophysically observed ranges. Thus, the present model can act as a testbed to incorporate other feedbacks, and to test new parametrizations at low computational cost.

Albedo parametrization: The albedo of an ice covered ocean was strongly conceptualized in this work. In nature the albedo depends on snow depth, ice thickness, ice type and the history of the ice (freeze-thaw cycles). More of these dependencies can be incorporated into the albedo parametrizations presently used. The performance of more involved albedo

parametrizations used in GCMs (see Liu, Zhang, and Horton, 2007) can be tested.

Other feedbacks: The ice albedo feedback is only one of many feedbacks in the climate system (Bony et al., 2006). Additional feedbacks can be incorporated into the present model through adjustments of the forcing equations (cloud and water vapor feedbacks) and through addition of surface properties and precipitation events (snow feedback).

Cascading perturbations: The lateral coupling has been shown to amplify albedo feedback through perturbation of local stable states. An in-depth study of the connection between lateral coupling strength (horizontal eddy diffusivity) and albedo feedback would further the understanding of the different behavior of summer and winter ice edge under additional surface forcing.

Introduction of noise: The work presented here was performed with constant additional forcing in order to investigate the systems underlying dynamics and asymptotic behavior. A natural next step would be to introduce controlled noise into the additional forcing in order to understand the effect of forcing variations as would be observed due to cyclical multi-year timescale climate forcing, e.g., Pacific decadal oscillation and El Niño.

Currents and ice export: Mechanical heat transport has been implemented in the regional scale model via eddy thermal diffusivities. Currently these diffusivities are laterally and vertically isotropic. A prevalent lateral current can be implemented by using an anisotropic horizontal eddy thermal diffusivity. In conjunction with an extension to a transpolar model grid the transpolar transport of heat due to currents could be studied. Ice export, as experienced through Fram Strait could be modeled via removal of a given portion of ice at one side of such a transpolar model.

References

Abbot, D, M Silver, and R Pierrehumbert (2011). "Bifurcations leading to summer arctic sea ice loss". In: *Journal of Geophysical Research* 116, p. D19120. DOI: doi:10.1029/2011JD015653.

Andreas, E., C. Fairall, P. Guest, and O. Persson (1998). *SHEBA ASFG PAM surface temperature data*. URL: http://www.eol.ucar.edu/projects/sheba/.

ARM Data Archive (2010). URL: http://www.archive.arm.gov.

Armour, K, I Eisenman, E Blanchard-Wrigglesworth, K McCusker, and C Bitz (2011). "The reversibility of sea ice loss in a state-of-the-art climate model". In: *Geophysical Research Letters* 38.16.

Bony, S, R Colman, V Kattsov, R Allan, C Bretherton, J Dufresne, A Hall, S Hallegate, M Holland, W Ingram, D Randall, B Soden, G Tselioudis, and M Webb (Aug. 2006). "How well do we understand and evaluate climate change feedback processes?" In: *Journal of Climate* 19, pp. 3445–3482.

Eisenman, I (2012). "Factors controlling the bifurcation structure of sea ice retreat". In: *Journal of Geophysical Research* 117.D1.

Eisenman, I, N Untersteiner, and J Wettlaufer (May 2007). "On the reliability of simulated Arctic sea ice in global climate models". In: *Geophysical Research Letters* 34.10, pp. 1–4.

Eisenman, I and J Wettlaufer (Jan. 2009). "Nonlinear threshold behavior during the loss of Arctic sea ice". In: *PNAS* 106.1, pp. 28–32.

Liu, J, Z Zhang, and R M Horton (2007). "Evaluation of snow / ice albedo parameterizations and their impacts on sea ice simulations". In: *International Journal of Climatology* 91, pp. 81–91.

North, G (1984). "Small Ice Cap Instability in Diffusive Climate Models". In: *Journal of the Atmospheric Sciences* 41.23, pp. 3390–3395. ISSN: 1520-0469.

Notz, D (Dec. 2009). "The future of ice sheets and sea ice: Between reversible retreat and unstoppable loss". In: *PNAS* 106.49, pp. 20590–20595.

Paulson, C (1998). *SHEBA ice camp summer leads albedo data.* URL: `http://www.eol.ucar.edu/projects/sheba/`.

Perovich, D (1998). *SHEBA spectral light transmittance project data.* URL: `http://www.eol.ucar.edu/projects/sheba/`.

Sellers, W (1969). "A global climatic model based on the energy balance of the Earth-atmosphere system". In: *Journal of Applied Meteorology* 8, pp. 392–400.

Shine, K and A Henderson-Sellers (1985). "The sensitivity of a thermodynamic sea ice model to changes in surface albedo parameterization". In: *Journal of Geophysical Research* 90.D1, pp. 2243–2250.

Strogatz, S (1994). *Nonlinear Dynamics and Chaos.* Cambridge, MA: Westview Press.

Thomas, D and G Dieckmann (2003). *Sea Ice: An Introduction to physics, chemistry, biology and geology*. Malden, MA 02148-5020, USA: Blackwell Science Ltd.

Thorndike, A (June 1992). "A toy model linking atmospheric and thermal radiation and sea ice growth". In: *Journal of Geophysical Research* 97.C6, pp. 9401–9410.

Walker, G (2006). "The tipping point of the iceberg". In: *Nature* 441, p. 802.

Winton, M (2008). "Sea-ice albedo feedback and nonlinear Arctic climate change". In: *Arctic sea ice decline: observations, projections, mechanisms, and implications*. Ed. by C. M. Bitz E. T. DeWeaver and L. B. Tremblay. American Geophysical Union, pp. 111–131.